Final Report (March 15, 2006)

Lightweight, deployable, dual frequency/polarization microstrip antenna array for remote sensing of precipitation

John Papapolymerou, Georgia Institute of Technology

Introduction

During this 3-year project funded by NASA's Earth and Science Technology Office (ESTO), efforts focused on the development and experimental characterization of a 2x2 dual polarization/frequency antenna sub-array with an RF MEMS phase shifter on a multilayer, lightweight and flexible organic substrate. Selection of polarization is achieved with integrated low loss RF MEMS switches, while beam scanning is achieved with a 4-bit MEMS phase shifter. The sub-array operates at two frequencies of interest for remote sensing of precipitation: 14 GHz and 35 GHz. A simplified schematic of the envisioned sub-array is shown in Fig. 1, where the 14 GHz patches are on the top layer and the 35 GHz patches are on the middle layer (or vice-versa) of the organic layer stack up (Fig. 1). The sub-array was developed on Liquid Crystal Polymer (LCP) material that was characterized for the first time up to 110 GHz. This report consists of the following sections: a) characterization (electrical and mechanical) of LCP, b) dual polarization/frequency arrays on LCP, c) RF MEMS switches and phase shifters on LCP, d) compact Soft-Hard-Surfaces (SHS) for improvement of antenna performance, e) analysis of phased array including phase error impact on array performance, f) updated TRL assessment and g) final accomplishment Quad chart. The appendix also provides information on journal/conference publications, invention disclosures and students involved with this project.

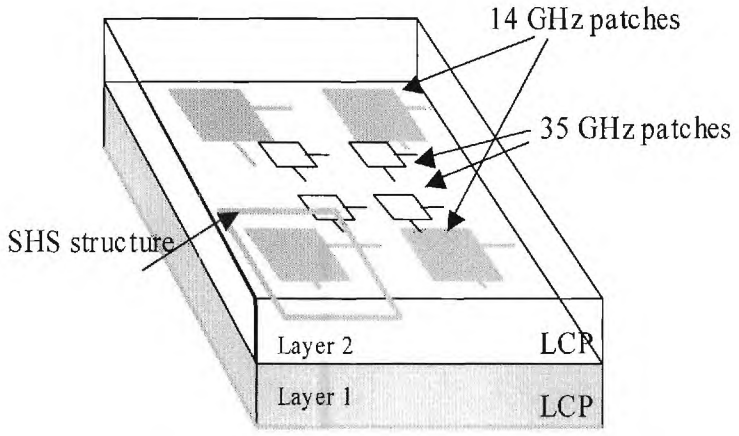

Fig. 1 3D-view of the dual polarization/frequency 2x2 arrays on LCP substrate with SHS ring.

A.1. LCP Material Characterization

A thorough investigation of LCP's dielectric properties from 2-110 GHz was performed. Microstrip ring resonators of varying diameters and substrate thicknesses have been used in conjunction with cavity resonators to extract LCP's dielectric constant and loss tangent, and the methods cross-referenced in order to provide certainty of the results. In addition, coplanar waveguides (CPWs) and microstrip lines, each on varying substrate thicknesses, have been characterized and the losses have been quantified in decibels per centimeter (dB/cm). The results of this investigation are summarized in the following figures and tables.

Figure 2 shows the resonators and resonant peaks used to extract the dielectric constant and loss tangent of LCP.

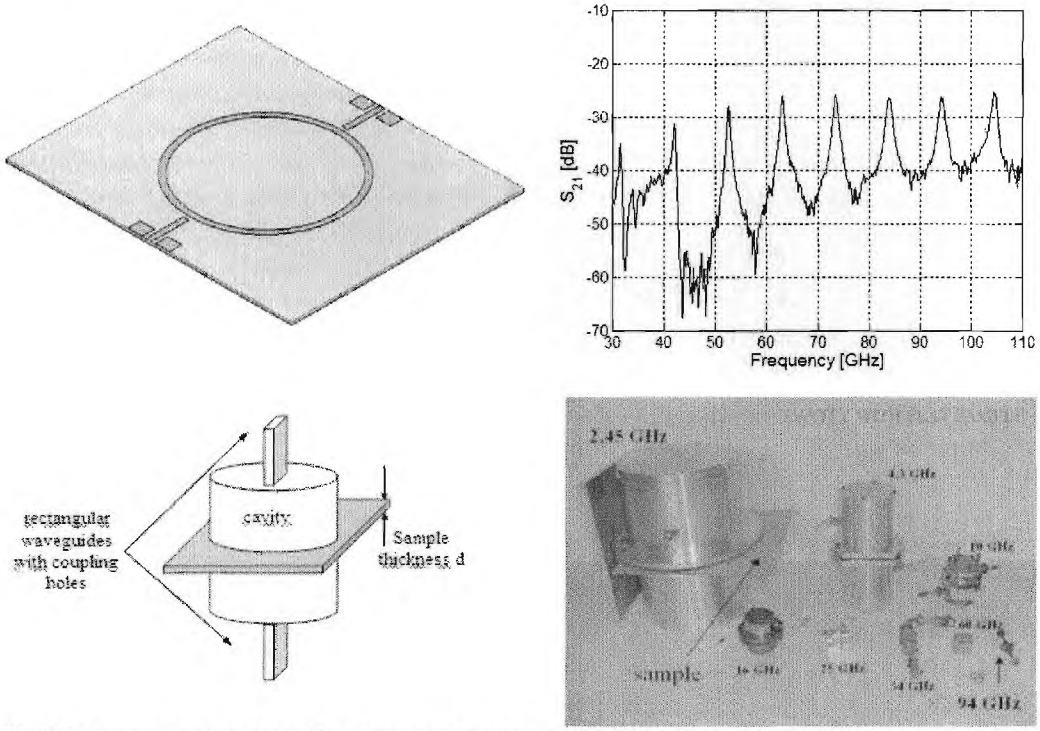

Fig. 2 Resonators and the associated resonant peaks which are used to extract the dielectric constant and loss tangent.

Figure 3 shows the dielectric constant results extracted from the ring resonator designs and the cavity resonators. The results between the two methods have very good agreement and show that LCP has a nearly static dielectric constant from 30-110 GHz. The value of ε_r slightly increases with frequency, but a value of $\varepsilon_r \sim 3.16 +/- 0.05$ is accurate over this entire frequency range. These stable dielectric constant results are important for establishing LCP as a material that can be used across the mm-wave frequency spectrum.

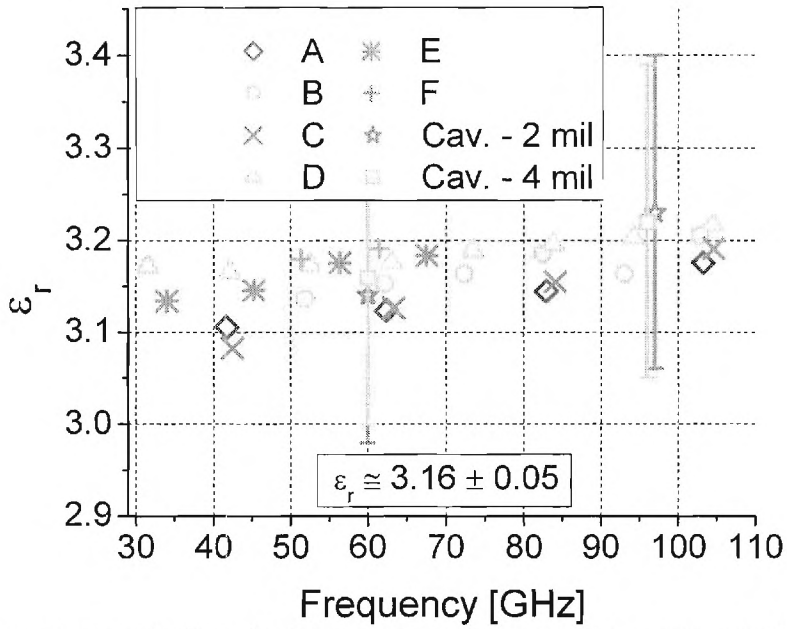

Fig. 3 Dielectric constant results from six ring resonator designs and cavity resonators at 60 and 97 GHz. The result is approximately constant at 3.16 with a slight increase vs. frequency.

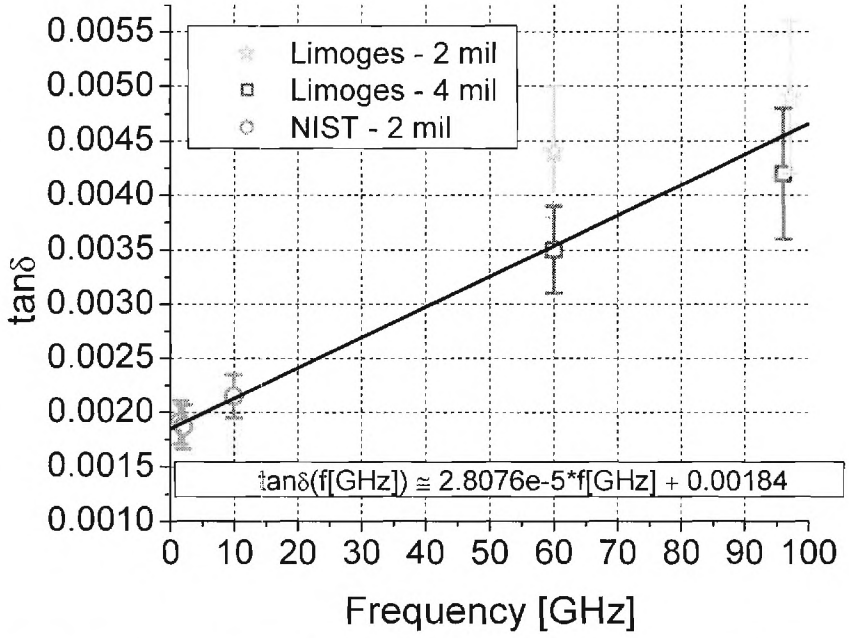

Fig. 4 Loss tangent results and a linear fit equation for the frequency dependent loss tangent from data extracted by cavity resonators at 2, 10, 60, and 97 GHz.

Figure 4 shows the results for LCP's loss tangent, including a linear fit that describes the loss vs. frequency. The loss tangent results show that LCP becomes more lossy with increasing frequency.

Apart from extracting the dielectric properties of LCP, the losses of common transmission lines printed on LCP substrates of different thickness have also been quantified. These are summarized in figures 5, 6 and 7. Attenuation values decrease with increasing substrate thickness. The peak attenuation values at 110 GHz varied between 0.88 and 2.55 dB/cm depending on the substrate thickness and line configuration. The substrate thicknesses varied between 2 and 8 mils while the line impedances were approximately between 50 and 85 ohms.

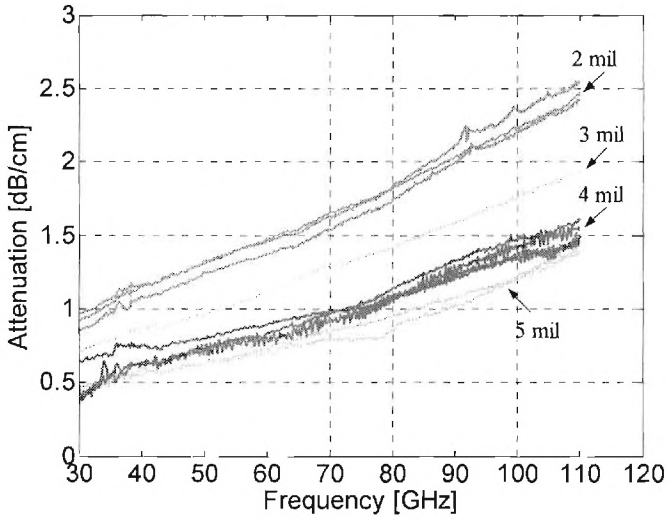

Fig. 5 Microstrip transmission line losses on different LCP thicknesses.

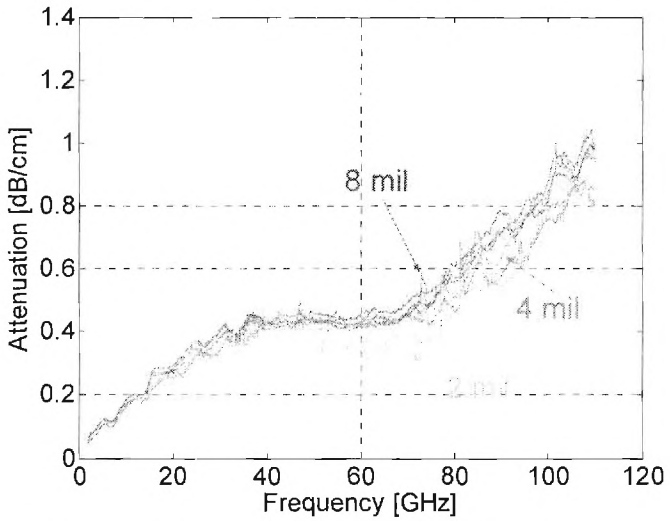

Fig. 6 Coplanar waveguide transmission line losses on different LCP thicknesses.

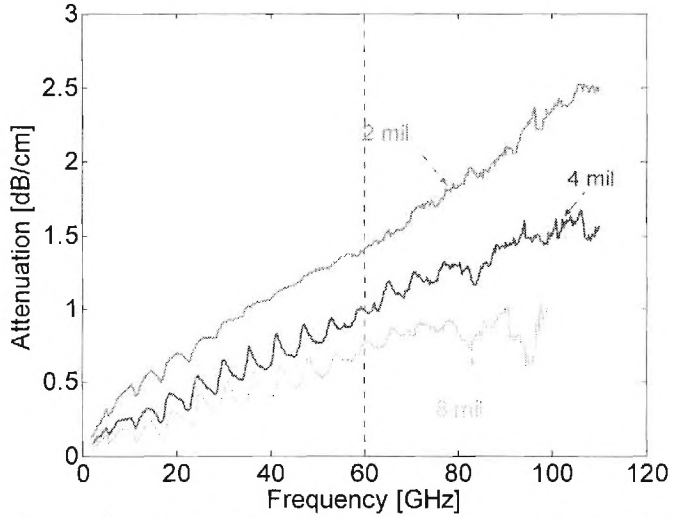

Fig. 7 Conductor-backed coplanar waveguide transmission line losses on different LCP thicknesses.

The temperature dependent dielectric stability and transmission line losses of liquid crystal polymer (LCP) are determined from 11–105 GHz. Across this frequency range, LCP's temperature coefficient of dielectric constant, $\tau_{\varepsilon r}$, has an average value of -42 ppm/°C. At 11 GHz the $\tau_{\varepsilon r}$ is the best (-3 ppm/°C), but this value degrades slightly with increasing frequency. This $\tau_{\varepsilon r}$ average value compares well with the better commercially available microwave substrates. In addition, it includes information for mm-wave frequencies whereas standard values for $\tau_{\varepsilon r}$ are usually only given at 10 GHz or below. Transmission line losses on 3- and 5-mil LCP substrates increase by approximately 20% at 75 °C and 50% or more at 125 °C. These insertion loss increases can be used as a design guide for LCP circuits expected to be exposed to elevated operating temperatures. The results of this investigation and comparison of LCP's dielectric stability with other popular microwave substrates are shown in figures 8 – 11.

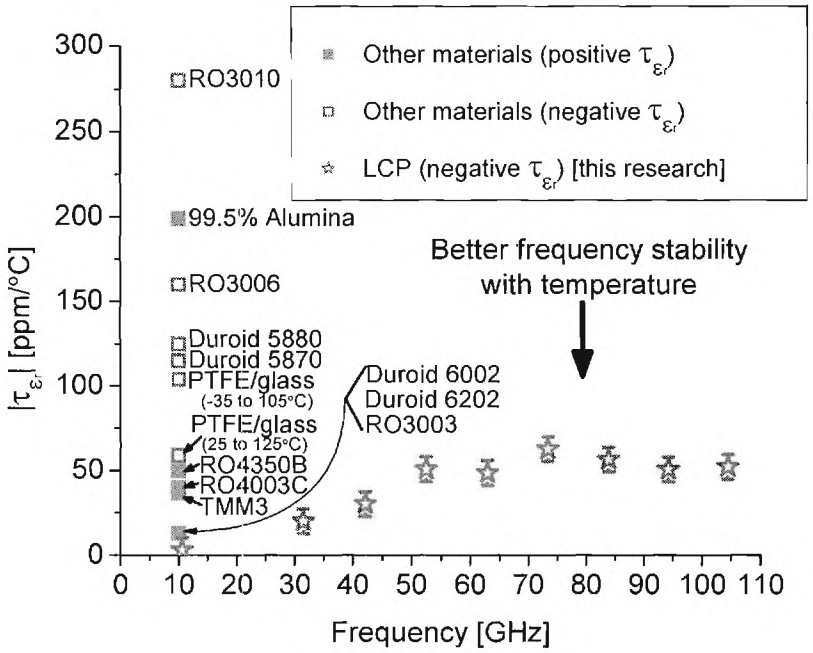

Fig. 8 Absolute value of the thermal coefficient of dielectric constant, $\tau_{\varepsilon r}$, vs. frequency of several standard materials and of the broadband $\tau_{\varepsilon r}$ for LCP. The closer $|\ \tau_{\varepsilon r}\ |$ is to zero, the more stable the dielectric constant is with respect to temperature.

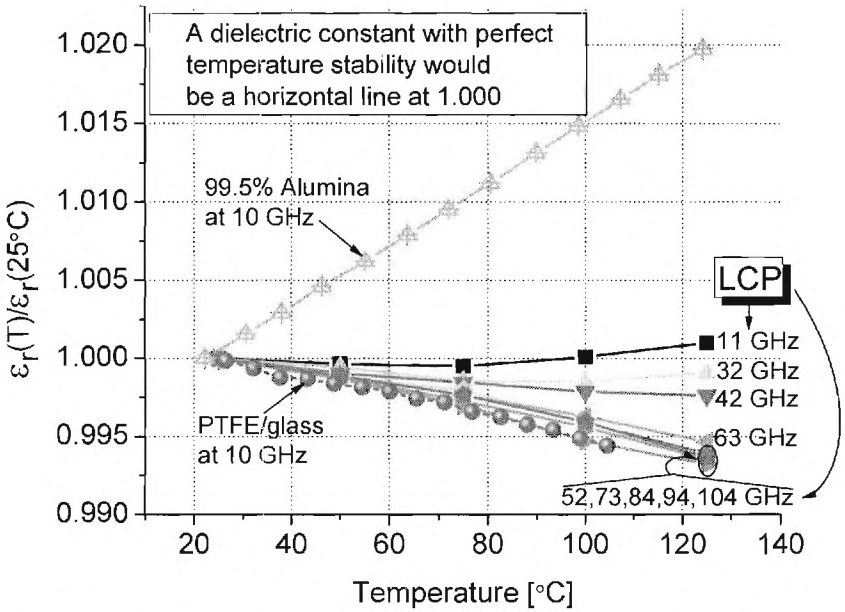

Fig. 9 The ratio of LCP's heated dielectric constant and the dielectric constant at 25 °C vs. temperature. The values for LCP are for measurements from 11–105 GHz from this paper. As a comparison, 99.5% alumina and PTFE/glass have been included. Notice that the values for 99.5% alumina and for PTFE/glass are for measurements at 10 GHz [3].

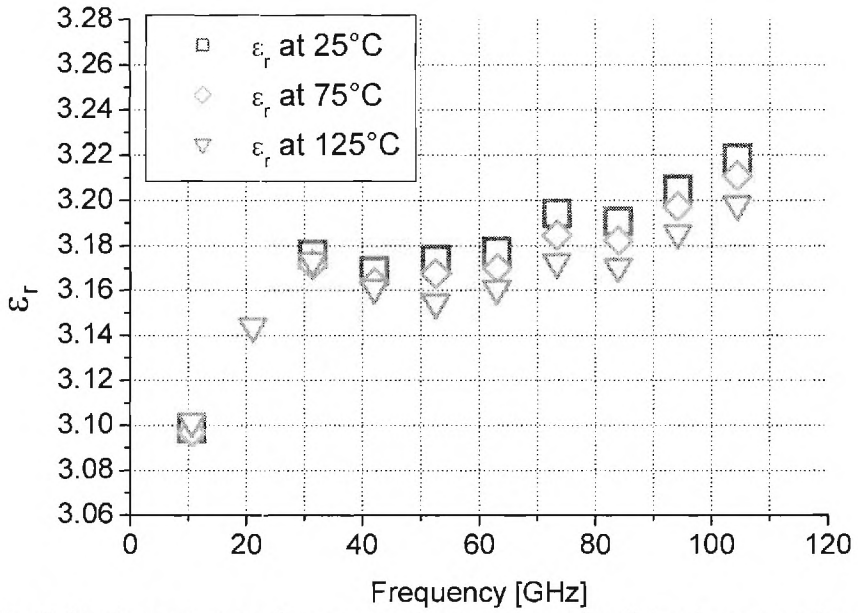

Fig. 10 LCP's dielectric constant vs. frequency and temperature. The dielectric constant increases with increasing frequency and decreases with increasing temperature. Note that the peak at 21 GHz did not have a well shaped Gaussian distribution and thus the resonant frequency could not be accurately calculated. However, the 21 GHz measurement at 125 °C was the best fit at that frequency and so only it is included for an estimate of the dielectric constant.

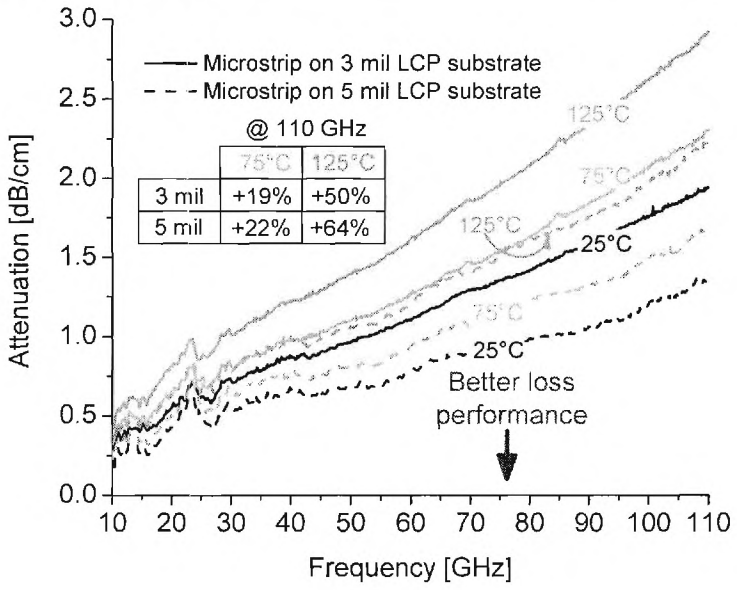

Fig. 11 Attenuation of 3- and 5-mil LCP substrate microstrip transmission lines as a function of temperature. Line width, W, was 104μm for both lines which gave Z_0 = 68 Ω and 88 Ω for the 3- and 5-mil thicknesses, respectively.

A. 2 Antenna Flex Testing

One of the key capabilities of antennas on LCP is the assumed ability to be rolled and then deployed once in space. To verify these capabilities, tests were performed on the mechanical rollability and the effects of rolling on the antenna performance. A 14 GHz 1x2 design was used as a test case. This antenna array is on a 17 mil substrate which is close to the 18 mil substrate thickness used for the final 2x2 antenna design.

The procedure for performing this antenna testing included:

1. Ensuring measurement repeatability when connecting/disconnecting an antenna in the default "flat" state
2. Performing flexure testing on the antenna, rolling it into tubes with various diameters
3. Re-measuring and observing potential differences in measurement or visual structural changes

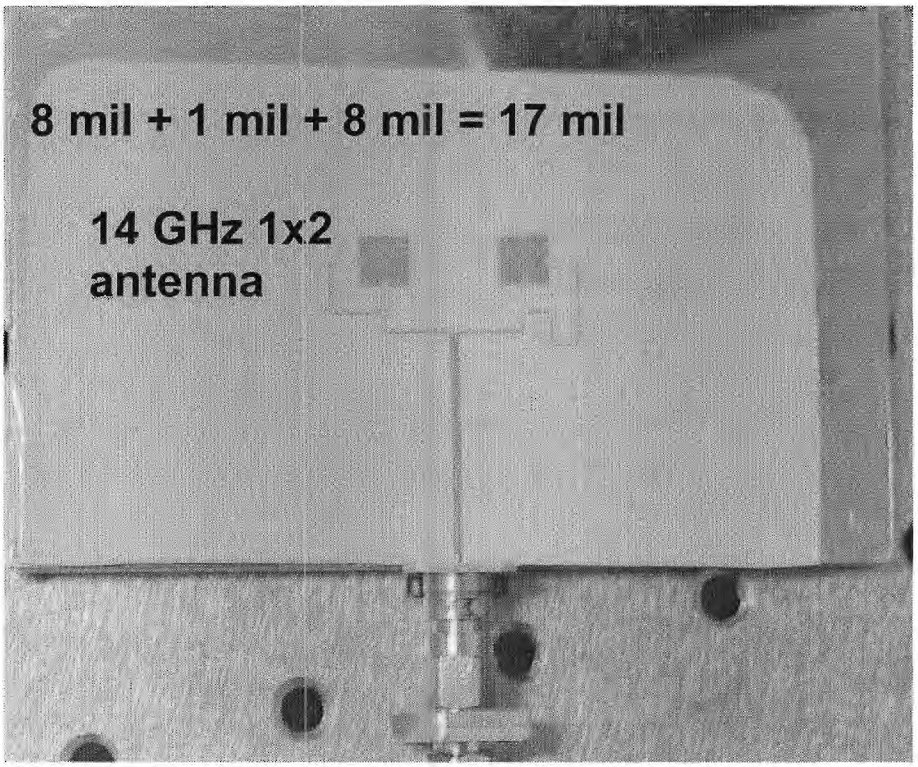

Fig. 12 The 14 GHz 1x2 antenna array on a 17 mil bonded LCP substrate.

To ensure measurement repeatability the antenna was connected and disconnected five times by:

1) Sliding the antenna feed between the coaxial signal pin and the metal ground plane

2) Forcing the signal pin into hard mechanical contact with the feed line and screwing it into position (no solder used)

Each time the antenna was connected, it was re-measured with a network analyzer to determine if any shifts in resonant frequency were occurring. 201 data points were used in an SOLT calibrated measurement from 12-16 GHz. The resulting frequency step was 20 MHz which is a 0.14% frequency resolution at the resonant frequency of 13.80 GHz. This resolution was deemed sufficient to determine any significant frequency shifts. Figure 13 shows the measurement results from measurements taken during the five connect/disconnect cycles. The S_{11} plots are nearly identical.

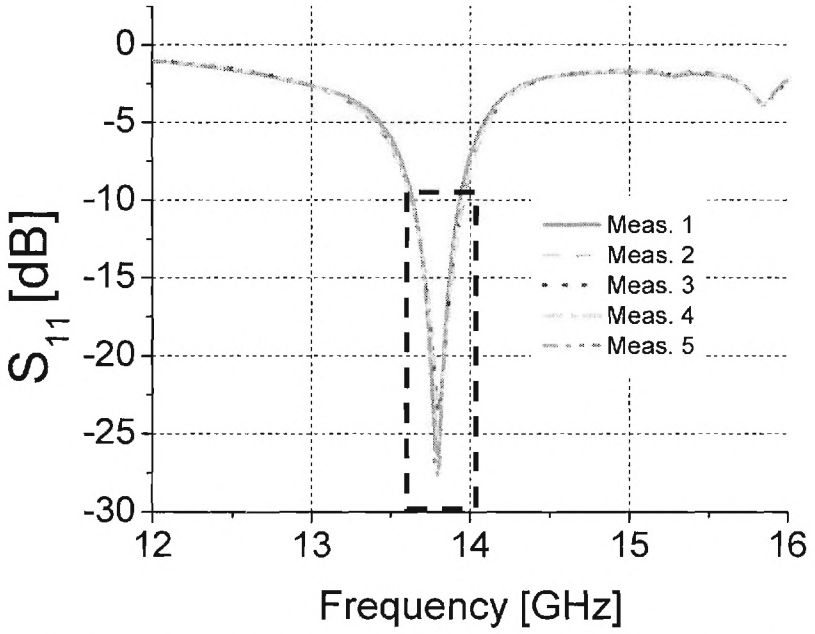

Fig. 13 Measurement repeatability testing by connecting the antenna five times and re-measuring it. The dotted rectangle area is magnified and re-plotted in Fig. 14.

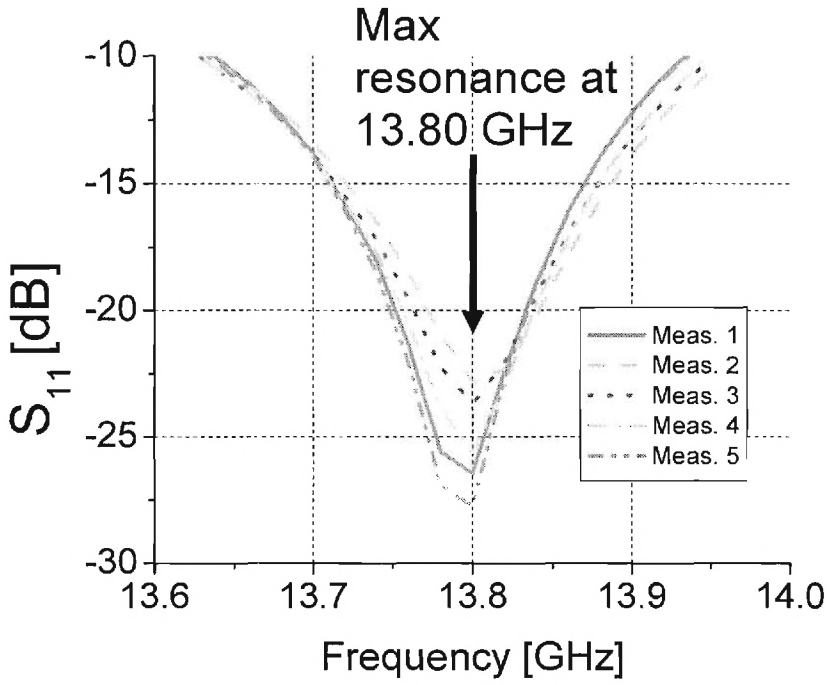

Fig. 14 Zoomed in plot of Fig. 13. The resonance minimum occurs at the exact same frequency point every time showing that the measurement is repeatable when the antenna is in its default (flat) state.

Figures 13 and 14 show no shift in resonant frequency. The level of S_{11} at resonance varies from -22.5 dB to -27.5 dB which is a negligible 0.4% difference in radiated power.

To test the potential antenna rolling capability, several plastic pipes of varying diameter were used as the conformal surfaces. The inner diameters of the pipes used were 6-5/8", 4-1/2", 3-1/2", and 2-5/8". Fig. 15 shows a size comparison of the various pipe diameters next to the antenna and a penny.

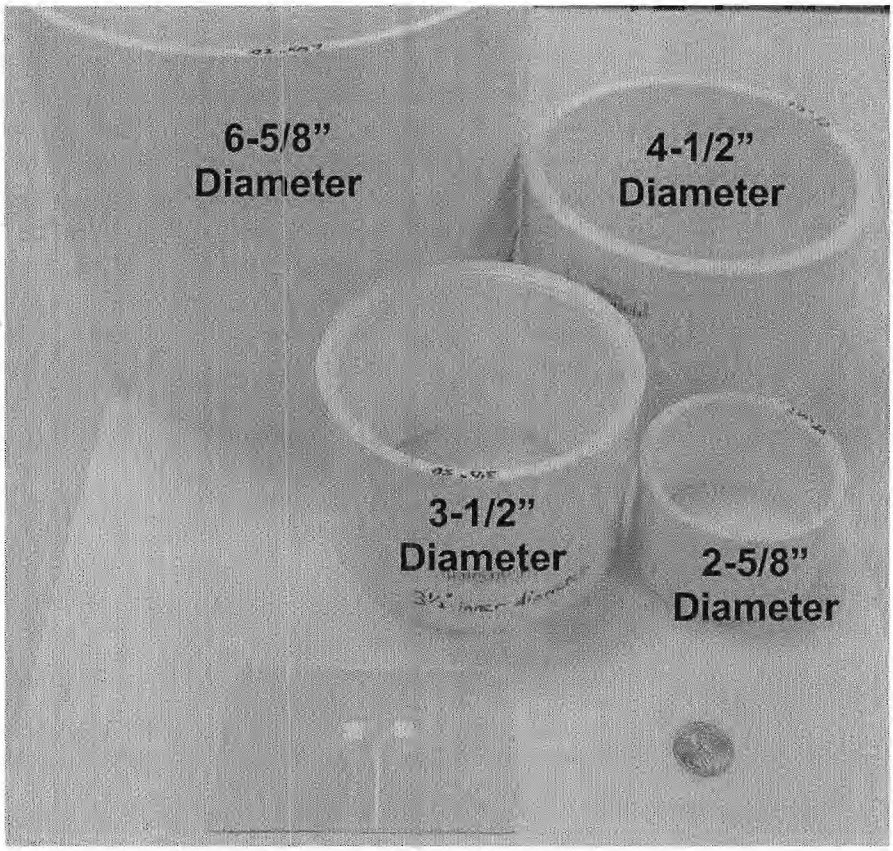

Fig. 15 Various pipe diameters in which to roll the 14 GHz antenna

Figure 16 shows the antenna array conformed inside of the 2-5/8" pipe.

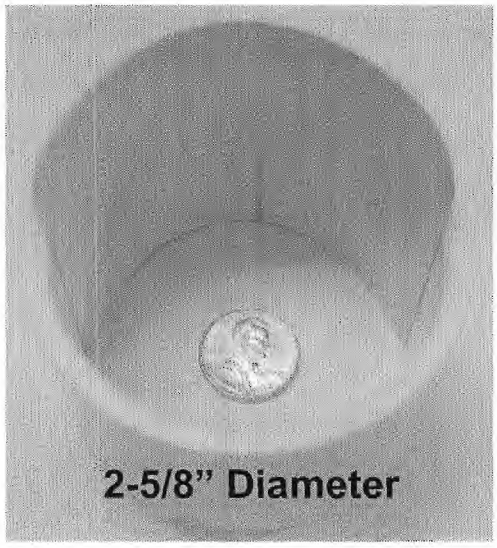

Fig. 16 The antenna conformed inside the 2-5/8" inner pipe diameter

An extreme case where the antenna was wrapped around a magic marker is shown in figure 17.

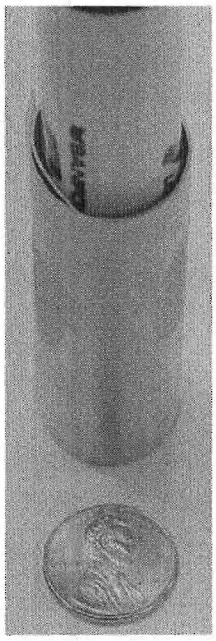

Fig. 17. The antenna rolled around a magic marker and taped in place

Figure 18 shows the same roll diameter from the magic marker from the top view. In this state the antenna has a roll diameter similar to that of a penny.

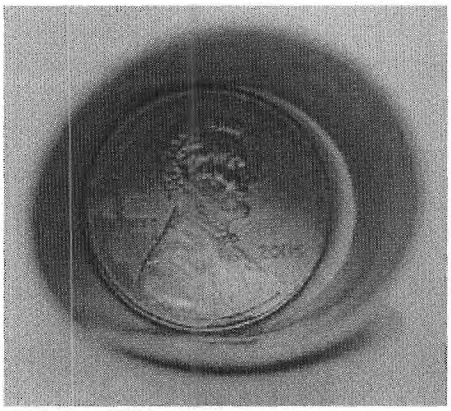

Fig. 18 The antenna roll diameter from the magic marker shown in comparison to the diameter of a penny

For each of these antenna roll diameters the following procedure was carried out:

1. The antenna was conformed to the inner diameter of each pipe (to the outer diameter of the magic marker) and held for 1 minute
2. The antenna was removed, flattened, and re-measured

For most of the roll diameters the antenna was easy to force flat to re-measure in the same flat position as the base case. However for the two tightest roll diameters of the 2-5/8" pipe and the magic marker, a more significant residual curvature remained. This curvature was also able to be flattened with mechanical force, but before doing this we decided to measure the antenna in each of these curved states to see how the curvature affected the radiation frequency. Figures 19 and 20 show the residual antenna curvature from these two rolled states.

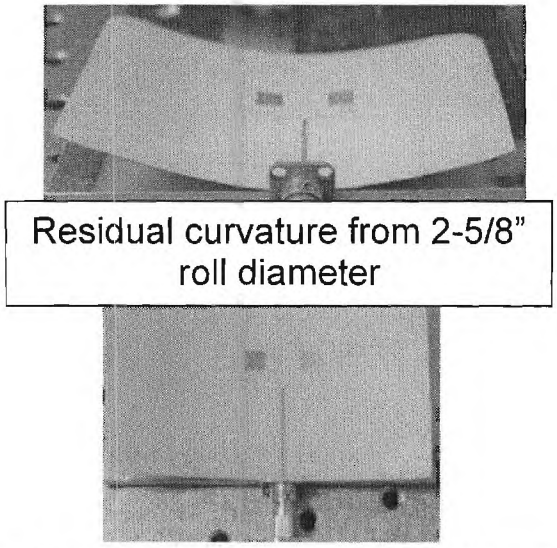

Fig. 19 Side and top views of the residual curvature of the antenna after taking it out of the 2-5/8" diameter pipe

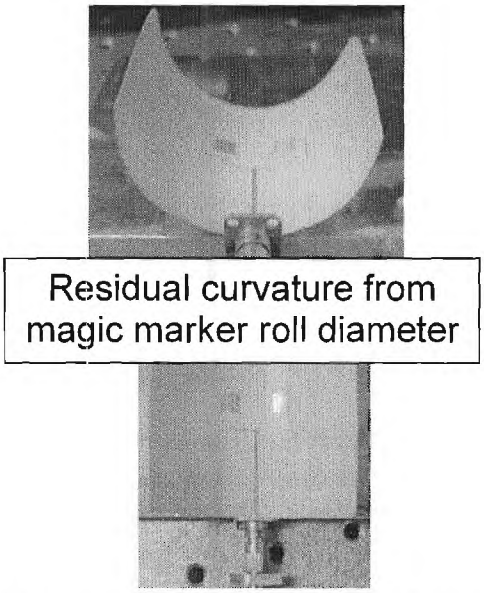

Fig. 20 Side and top views of the residual curvature of the antenna after taking it off of the magic marker

The measurement results from all of the aforementioned cases are shown in figures 21 and 22. These include:

1. Measuring the antenna flattened after flexing to different diameters
2. Measuring the two cases of the antenna with the residual curvature
3. Measuring the antenna after flexing it in opposite directions in the 2-5/8" diameter 10 times then flattening it

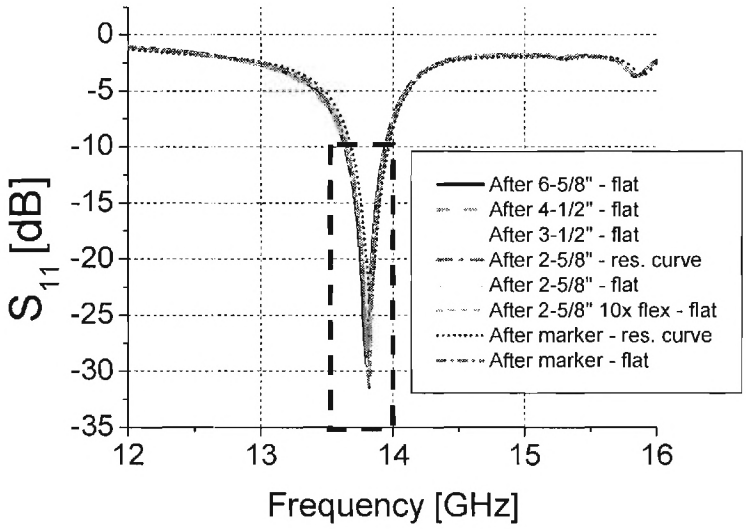

Fig. 21 Measurement results of all of the cases of flexing the antenna. Two of the measurements include the antenna in a curved state while the rest are of the flattened antenna after conforming it to different roll diameters

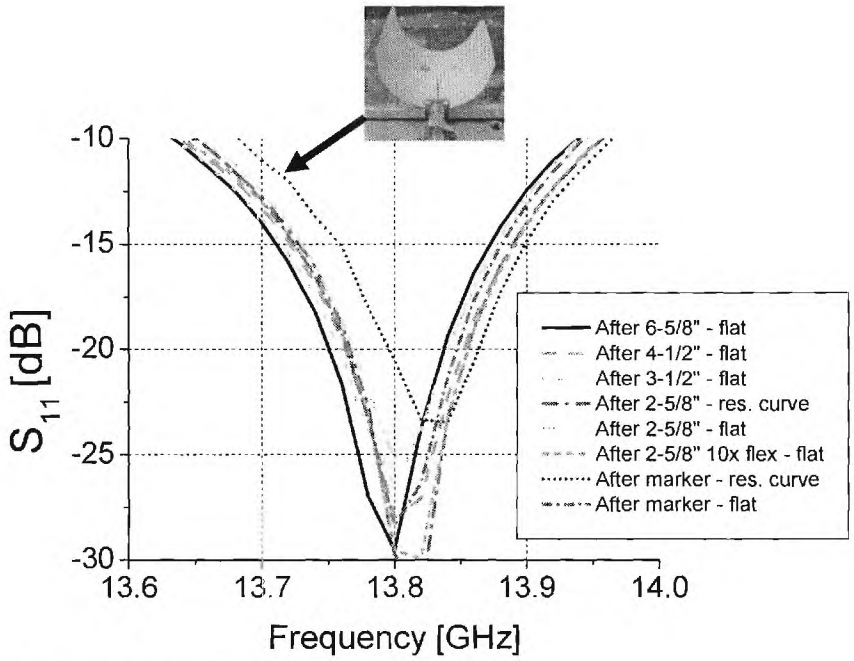

Fig. 22 A zoomed in representation of Fig.

The measurement case that differed significantly was the one measured in the curved state with extreme residual curvature from the diameter of the magic marker. Still, even with this curvature the S_{11} shift was only 0.29%! After flattening the antenna, it again performed the same as before. The conclusion from these flex measurements is that the antenna flexure does not affect the antenna performance.

In regards to the mechanical robustness of the antennas, no metal or substrate delamination was observed. The amount of force required to re-flatten the substrate was not measured, but it was done without much difficulty using hand manipulation.

A.3 Antenna Sensitivity to Fabrication Tolerances, Dielectric Constant, and Humidity

A.3.1 Overview

To determine the potential reasons for shifts in resonant frequency for the various generations of NASA antennas, several single patch antennas were designed and fabricated on 4 mil LCP substrates. Single patches were used because they give clean, well-defined resonances with minimal parasitics that could confuse the response. The 4 mil substrate was selected so that all designs could be fabricated on a single board. The 4 mil substrate is thickest commercially available LCP substrate that does not require extra bonding steps.

The design frequencies were at 6, 14, 28, and 35 GHz. Since the substrate thickness was held at 4 mils (which is thin for lower frequency antenna designs), the best bandwidth and return loss characteristics were achieved for the 35 GHz antennas. Also,

the 35 GHz stackup is closest to the final 2x2 configuration, so these were used for the duration of the following tests.

The designed antennas were done with an assumed dielectric constant of 3.16. To test the repeatability of more than one antenna, six of the 35 GHz antennas were fabricated. The designed and measured responses for the 35 GHz antenna(s) are shown below.

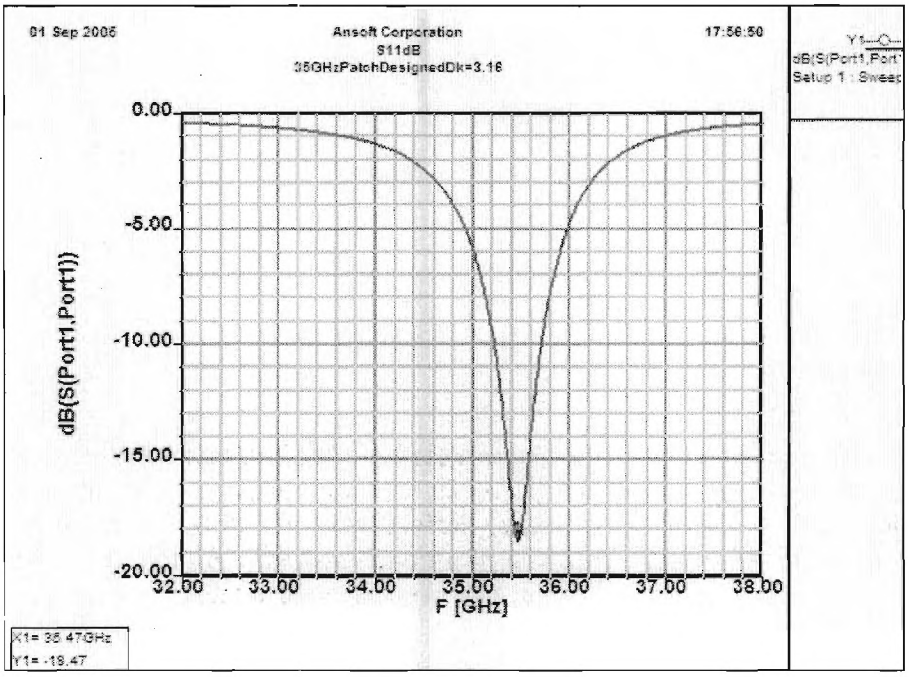

Fig. 23 Simulated response of the 35 GHz antenna

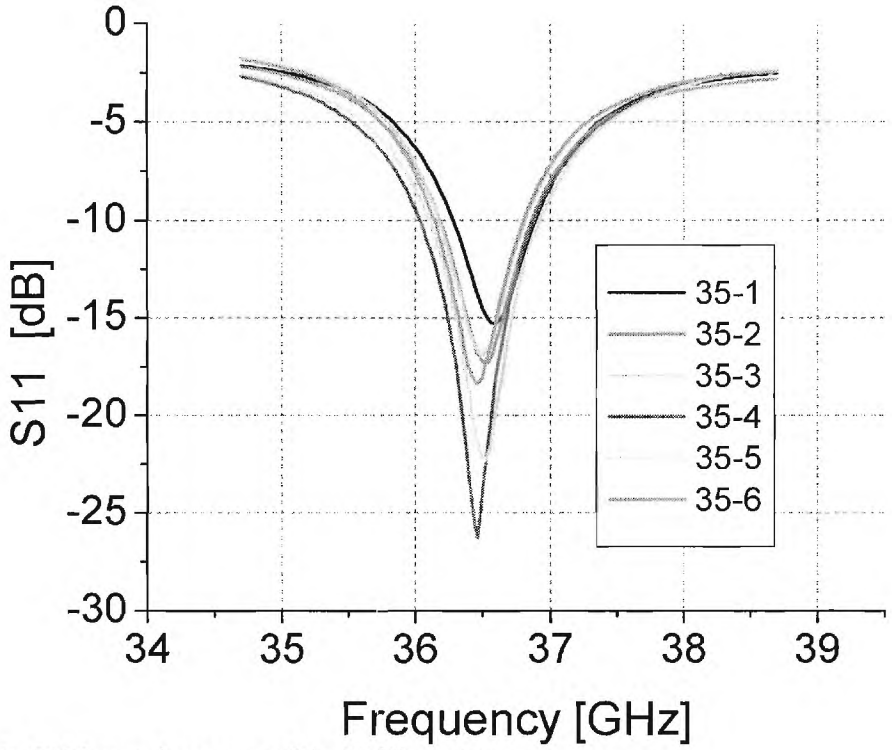

Fig. 24 Measured responses of the 35 GHz Antenna

The measured antennas all have resonances around 36.5 GHz which is about a 1 GHz shift from the design.

A.3.2 Sensitivity to Fabrication

The antenna designs were all fabricated with standard double copper clad LCP sheets from Rogers Corporation. The 18um thick double copper cladding was patterned using ferric chloride chemical etching in 6"x6" polypropylene containers with hand agitation. This is the standard process we use in the lab environment. It works well, but the etch uniformity is significantly less than it would be from a large scale fabrication company. One downside to such a small etch container is that the fluid flow around the periphery of the container is much faster than in the center and this results in the edges of the board etching before the center. This means that designs near the edges of the board will have greater undercut than those near its center. Six of these 35 GHz antennas were laid out on the board in different locations.

After fabrication the designs were imaged with the Wyko Optical Profilometer, which is capable of stitching together a complete profile of the actual antenna size with data point sampling of 1.65um in the plane of the patch (this sampling can be made finer at the expense of longer scan times). This gives a very accurate method of measuring the fabricated antenna dimensions. Of course, this method would run into time constraints for large antennas, but for the 35 GHz patches, with dimensions of about 2.3 mm x 3.3 mm, each full scan took between 5 and 10 minutes.

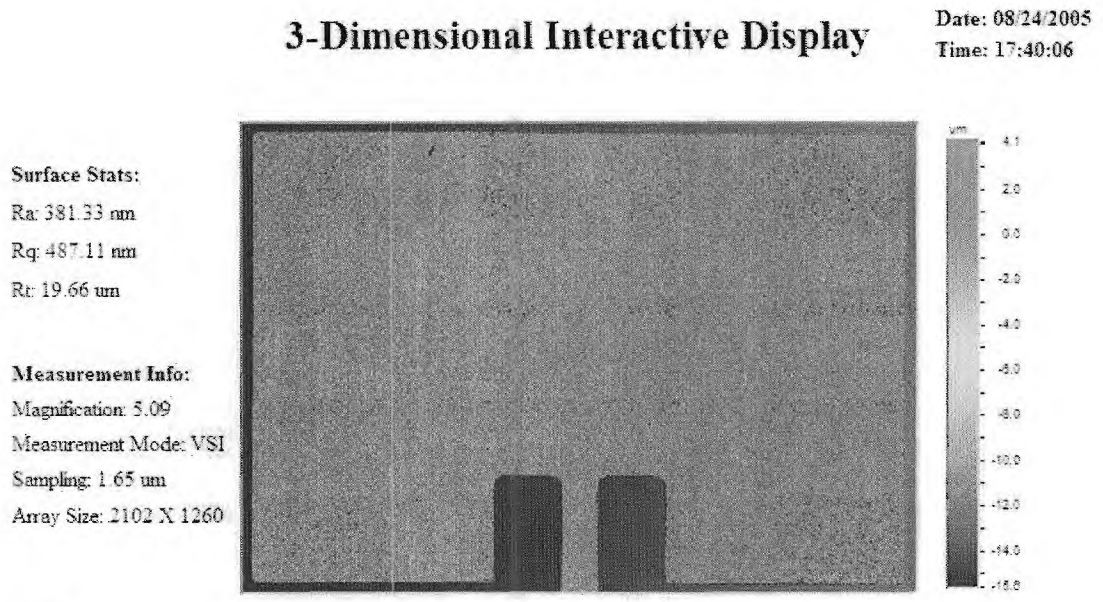

Fig. 25 Profilometer scan showing the rounding of the slots and the surface roughness of the antenna.

We determined that the fabricated antennas differed somewhat significantly from the designs due to large etching undercut. In several measurements the fabricated antennas were off by 40 to 50 um from the design. The table below shows this discrepancy for one of the antennas.

Antenna 35-3	Designed Dimensions [um]	Fabricated Dimensions [um]	Difference [um]
PatchLengh	2350	2310	-40
PatchWidth	3368	3332	-36
SlotLength	555	555	0
SlotWidth	830	880	50
MstripWidth	230	180	-50

One might be concerned with such seemingly large change in the design. We tested this by simulating the antenna (still with a dielectric constant of 3.16) with the measured dimensions. The effects on the simulated response, however, were not significant in terms of a frequency shift. The frequency only shifted down by 30 MHz (to 35.44 GHz from 35.47 GHz). The depth of the resonance was reduced by about 4 dB.

We concluded that the antenna sensitivity to fabrication tolerance could not explain the large frequency shift that we saw in the measured response.

A.3.3 Sensitivity to Dielectric Constant

One candidate for shifting an antennas center frequency is the dielectric constant. To test the effect of this on our single 35 GHz patch antenna, the same initial design was simulated with dielectric constants of 3.16 (nominal design), 3.0, 2.95, and 2.9. The results of these simulations are shown below.

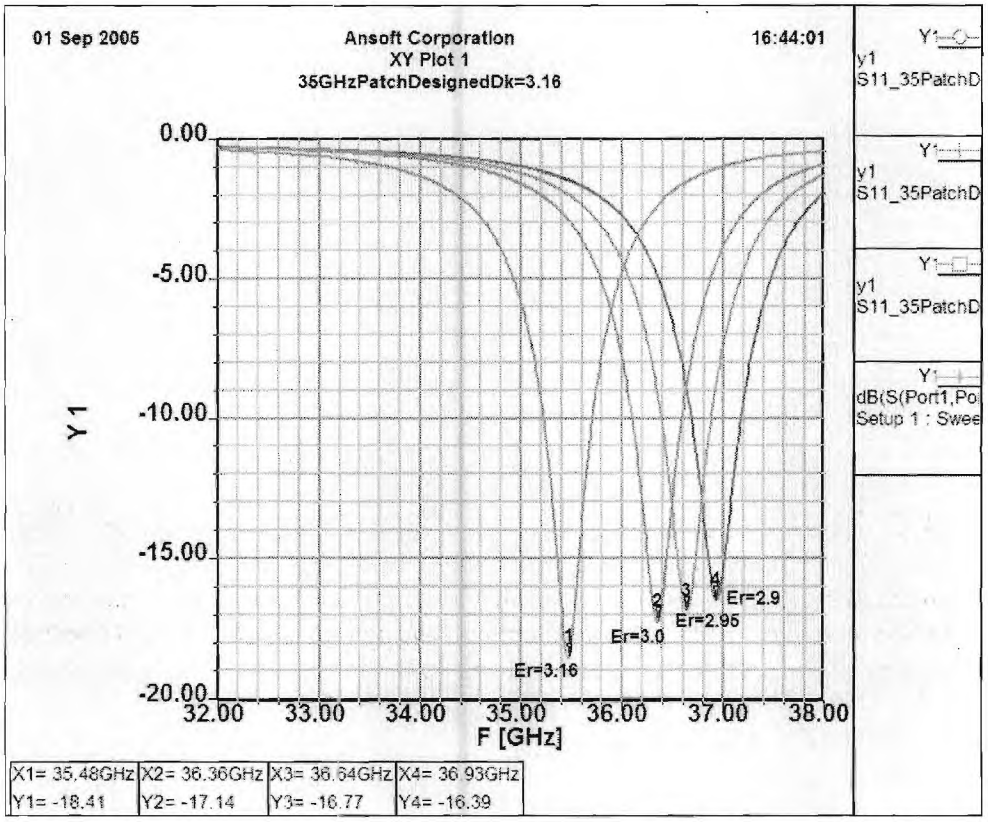

Fig. 26 Simulation results showing the effect of dielectric constant on resonant frequency

Testing the sensitivity of the patch design to variations in the dielectric constant reveals that large frequency shifts (almost 1.5 GHz [4.1%]) can occur with small changes in the absolute value of the dielectric constant. Here the dielectric constant range is from 3.16 down to the manufacturer's specification of 2.9. Although this is only a difference in dielectric constant of 0.26 from maximum to minimum, it is an 8.2% change in dielectric constant. This is something that must be considered for low dielectric constant materials since they are more sensitive to variations. What must be determined is how consistent the dielectric constant of LCP is across a single board and also from batch to batch.

Using the information from the plot above about the effects of dielectric constant on the resonance frequency of our 35 GHz patch, an estimated dielectric constant of 2.975 was used to try to match the simulation to the measurements. A simulation of antenna

35-3 with the fabricated dimensions and ε_r=2.975 was performed and the resulting S11 is shown.

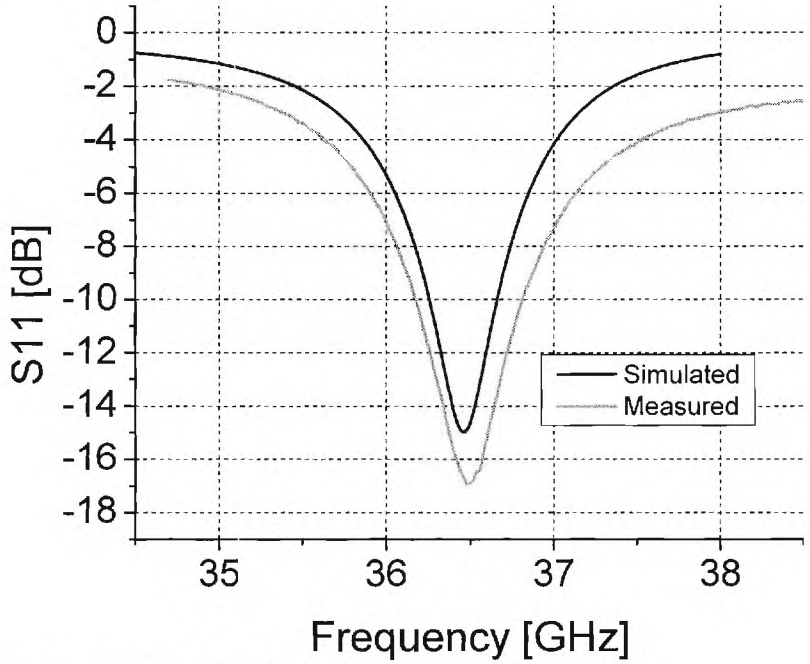

Fig. 27 Comparison between simulated and measured response with ε_r = 2.975

With the fabricated dimensions and simulating with ε_r = 2.975, a result very close to the measurement is achieved. The resonance frequency is within 40 MHz and the depth of the resonance is within 2 dB. A conclusion of this investigation is that the antenna is much more sensitive to dielectric constant changes than to fabrication errors.

A.3.4 Sensitivity to Humidity

In addition to the above analyses, the real world sensitivity of LCP antennas to humidity is of great interest. To test this, we first must be sure that we can connect and disconnect an antenna repeatedly and have it give the same result. In addition, slight misalignments of the connector might contribute to skewed data. Both of these were tested and found to have a minimal effect on the measured results.

A thorough investigation of the effects of water absorption on LCP antennas was carried out during this project. Figs. 28-29 summarize the humidity test results for these antennas on LCP and other organic substrates (3003, 6202). As it is shown in Fig. 28, LCP has the smallest gain increase (~0.038%) compared to the other substrates for the IPC-TM-650 humidity test. In terms of resonant frequency shift, there is none observed for the LCP antennas even after the sample has been immersed for 16 days in water.

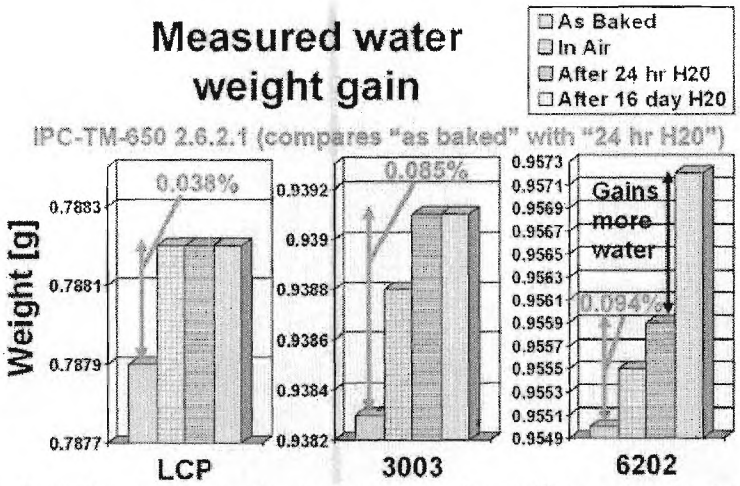

Fig. 28. Measured sample weights to the nearest tenth of a milligram for the following cases: 1) Immediately after baking in an oven at 110°C for 1 hour; 2) Dry, at room temperature and ambient humidity; 3) After 24 hours submersed on edge in distilled water, the surface water dried thoroughly upon removal, and the sample measured immediately; 4) With the same method as 3) except after the samples were submerged for 16 days.

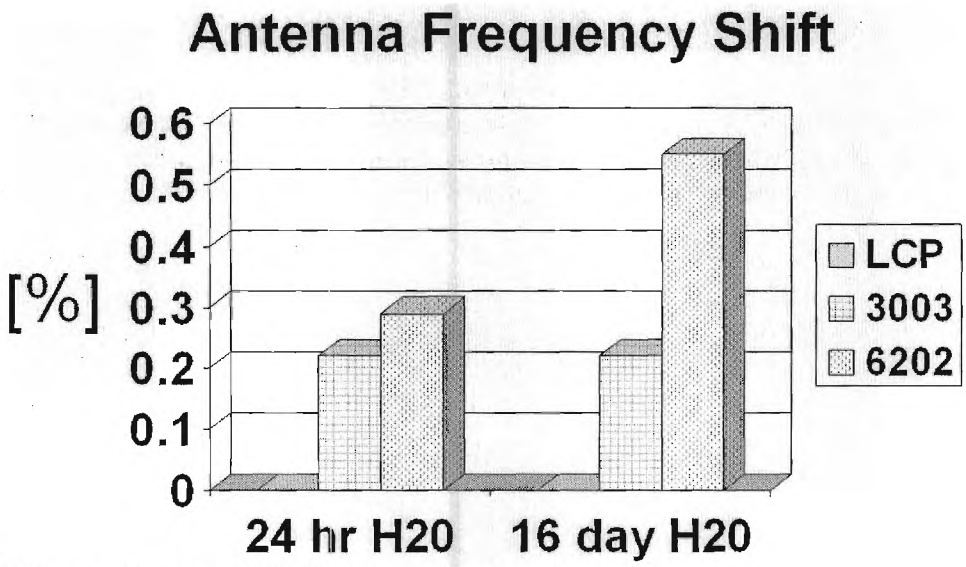

Fig. 29. Measured frequency shift of 14 GHz microstrip patch antennas.

B. Dual Frequency/ Dual Polarization Antenna arrays

We have developed dual frequency and dual polarization microstrip antenna arrays on multilayer liquid crystal polymer (LCP) technology. Microstrip patch antennas are desirable antenna elements due to its low cost, low profile, lightweight, and ease of fabrication characteristics. Furthermore, the flexible nature of LCP and its multilayer lamination capabilities make it a suitable platform for space deployment and for integrating diverse components required in a radar system. There are many different ways of arranging the patch elements and the feed network. Two different configurations, one in which the patch elements are fed by a microstrip feed and the other in which the patch elements are fed through slots on the ground plane, have been explored.

B.1 Microstrip Fed Patch Antenna Arrays

B.1.1 Design

The generic multilayer architecture of the dual-polarization, dual-frequency patch antenna array with microstrip feed is shown in figure 30. The metal, used in simulation and fabrication, for the ground plane and the antenna elements is copper (Cu) and had a thickness of 18 μm. The total substrate thickness (h) for the design is 17 mils, consisting of two LCP layers (each 8 mils thick) and a 1 mil bonding layer. The 35 GHz antenna array is placed on the top surface of the LCP substrate (at the interface of LCP and air), while the 14 GHz antenna array that is physically larger is embedded on an 8 mil layer (h1). The two arrays were designed independently and then fine-tuned before integration in order to optimize the impedance matching and radiation characteristics across both bands. The particular choice of substrate thicknesses stemmed from extensive analysis of their influence on cross-polarization levels, bandwidth and efficiency at each frequency. The feed network for each array is placed in the same layer as the radiating elements to minimize computational and fabrication complexity and to reduce cross-talk between the arrays.

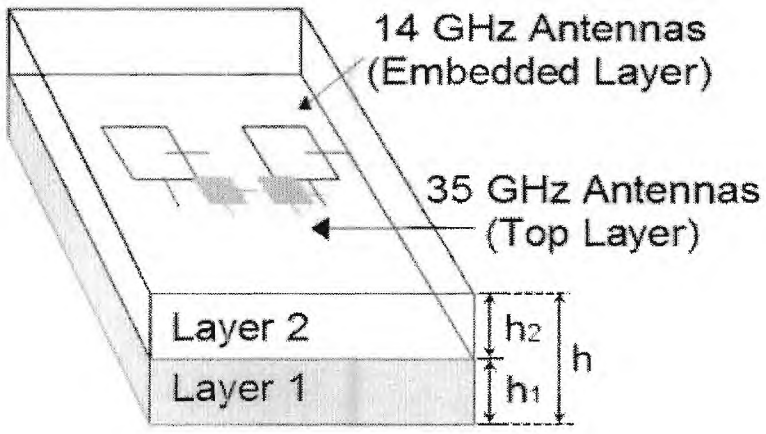

Fig. 30 Generic Multilayer architecture of the microstrip fed antenna array

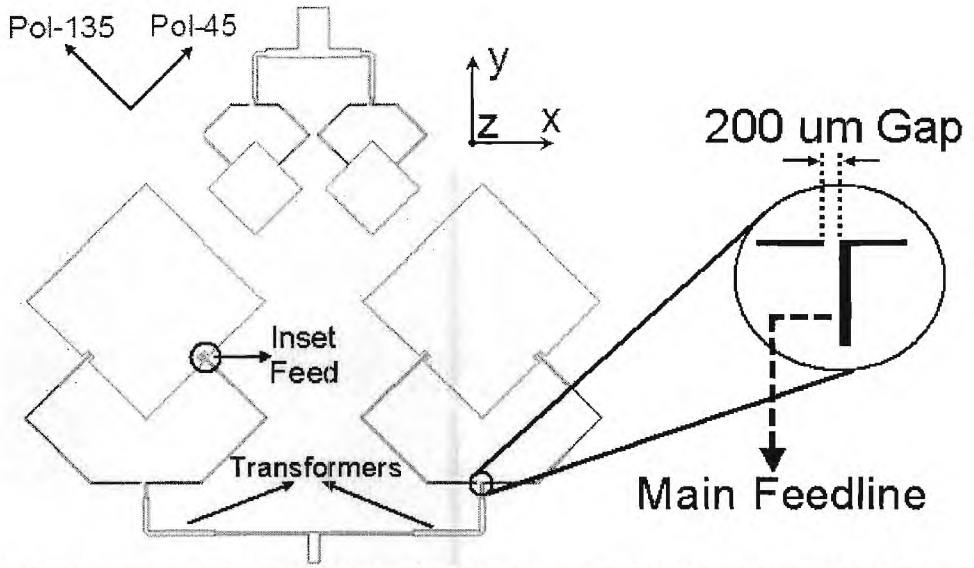

Fig. 31 Top View (with all layers interlaced) of the microstrip fed antenna array. The inset shows an enlarged portion of the feedline containing the 200 μm gap (on the left side branch of the main feedline). By moving the gap to the right ride branch, the polarization can be switched. The configuration shown here will result in radiation patterns with E-field polarized along the 135^0 axis.

The top view of the designed dual - frequency antenna array with diagonal patch elements is shown in figure 31. The patches are rotated by 45^0 and the polarization directions are at $45^0$and 135^0 as opposed to the traditional x-y directions. This kind of arrangement helps in realizing a symmetrical feed network for both polarizations. Currents are always fed in phase to all antenna elements in both polarization directions. This is essential in order to have the main beam pointing as close as possible in the bore-sight direction. The impedance characteristics such as the -10dB bandwidth and the radiation pattern characteristics, such as the directivity, the half power beam-width, the cross-polarization level, and the side-lobe level are very similar for both polarizations. This is one of the critical requirements of the antenna arrays used in satellite imaging systems. The feeding structure for each array contains 200 μm gaps (see inset in figure 29) to enable excitation of the dominant TM mode (TM_{10}) corresponding to one linear polarization and prevent excitation of the other mode (TM_{01}) that corresponds to the orthogonal linear polarization. In this case, the switching of polarizations is controlled by the presence of "hard-wired" perfect "short" (simulated by a continuous feedline) and "open" (simulated by a 200 μm gap) conditions. In a practical implementation, RF MEMS switches will be used to switch polarizations and steer the main beam. In order to minimize the radiation effects of the feed lines, the lines that directly connect to the radiating element are made as thin as possible. The position of the gaps was carefully chosen to minimize the cross-polarization levels. Specifically the length of the feed network between the patch edges and the gap position was made an integer multiple of $\lambda_g/2$ to transfer perfect open conditions to the edge of the patch. The dimensions of the patch were first optimized to make it resonant at the desired frequency. A recessed patch feed and a combination of T-junctions and quarter wave transformers were then employed to achieve better matching and a symmetric feed structure is used to expand

into a 2x1 array. EMPicasso, a MOM (method of moments) based frequency domain 2.5D solver, was used for design and simulations.

B.1.2 Fabrication

Copper-clad (18 μm) LCP dielectric sheets available from Rogers Corporation were used for fabrication. Although these sheets are available only in discrete thickness (1, 2, 4 and 8 mil), it is possible to realize many different substrate configurations due to the availability of two different types of LCP materials – type I LCP (core) and type II LCP (bond). The core layer melts at 315 ^{0}C while the bond layer melts at 290 ^{0}C. This difference in melting points allows formation of multilayer LCP substrates by sandwiching bond layers between core layers. Although a thick copper layer may restrict the minimum feature size due to undercut problems, it is difficult to sputter/ electroplate thin layers of copper on LCP reliably because it has a low stiction coefficient to copper. Therefore thick copper cladding is used and the etch process was characterized and the patterns are modified beforehand to compensate for the undercut. The undercut, if not compensated, can cause undesirable shifts in the resonant frequency of the array especially at 35 GHz. An alternative to using thick copper would be to introduce a thin seed layer such as titanium between copper and LCP to improve stiction. A thin seed layer (0.3 μm) will have no effect on the array performance because the copper layer (3 μm) will be much thicker in comparison. Such layers are often used in semiconductor circuits with no effect on performance. Shipley 1827 photoresist was used for pattern definition and the arrays were exposed under 16,000 dpi mask transparencies pressed into sample contact with 5" glass mask plates. Photoresist development and a wet chemical etch with ferric chloride were then performed to complete the antenna patterning.

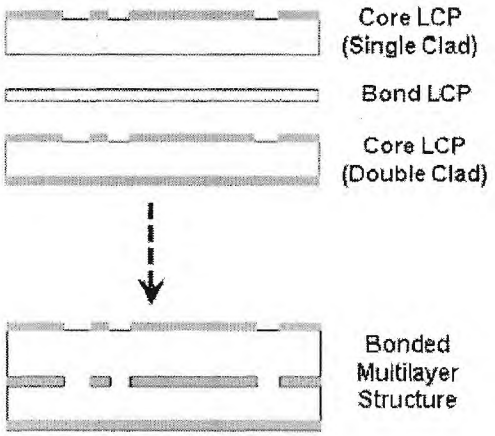

Fig. 32 Typical LCP Bond Process

Once the individual layers were patterned, the multilayer architecture was realized using bonding. The bond layer melts at a lower temperature than the core layers and its flow coupled with the tool pressure applied between the core layers results in the realization of multilayer LCP structures. This is the most critical step in the fabrication process and has to be understood thoroughly to create multilayer LCP structures reliably. Several experiments were carried out to optimize the temperature, the tool pressure and the process times to achieve good bonding while preventing shrinkage, formation of

bubbles and melting of core layers. The bubbles can result in air gaps that can affect the array performance at mm-wave frequencies. A typical LCP bonding process is illustrated in figure 32.

For the multilayer antenna array structure, accurate alignment between different layers is necessary. This is facilitated by drilling precision alignment holes using a laser system. Three different laser systems, the CO_2 laser, the excimer laser and the infrared laser, were used depending on the desired alignment accuracy levels. The holes were drilled before the individual layers were patterned. The alignment marks in the masks, which contain the patterns, were aligned to the laser holes drilled on the substrates during photolithography. After the individual substrates were patterned, alignment was maintained during bonding using alignment pins in the bonding press plates. This specific alignment procedure is unique and essential in creating multilayer antenna structures operating at mm-wave frequencies that require very precise alignment. The fabricated microstrip-fed array is shown in figure 33.

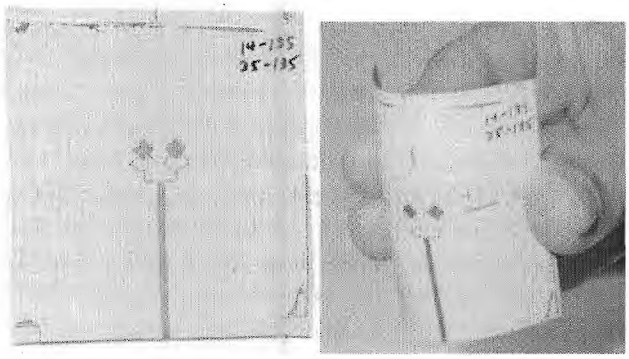

Fig. 33 Left: Photo of fabricated 2x1 Microstrip Fed array. The 14 GHz array is not visible as it is embedded. **Right:** Photo demonstrating flexibility.

B.1.3 Measurement

Return loss measurements were carried out by mounting the array on an aluminum fixture that included a 2.4 mm coaxial-to-microstrip connector. A short, open, load, and thru (SOLT) calibration was performed on a vector network analyzer with the reference planes at the end of the coaxial cables. When required, the microstrip launcher was adjusted to improve the Antenna under Test (AUT) to coaxial launcher impedance match. The antenna pattern measurements were carried out by Dr. George Ponchak at the NASA Glenn Research Center. An anechoic chamber with the AUT as the receive element and a 15 dB gain horn antenna as the transmitting antenna was used for radiation pattern measurements. The AUT was rotated through the measurement plane, and the entire system, including the data recording, was automated. Because the microstrip launcher and the absorbing material placed around it covered a portion of the plane during the scan, there was a slight asymmetry in the radiation patterns due to the characterization system. In addition, the absorber affected the radiation pattern at scan angles greater than 70^0 off boresight.

B.1.4 Results

The simulated and measured return loss plots versus frequency are shown in figures 34 (14 GHz) and 35 (35 GHz). The results are for the 135^0 polarization though they are the same for the 45^0 polarization also owing to the symmetric arrangement. The dual-frequency array was excited at one frequency, while the other array was treated as a parasitic element. The results are summarized in tables 1 and 2. The shift in the resonant frequency can be attributed to fabrication tolerances. The discrepancy in return loss at 14 GHz is due to the extension of the feedline of the embedded (14 GHz) antenna to a point where the top laminated layer of the substrate no longer covers the feedline, thus, modifying its characteristic impedance. The measured impedance bandwidths at both frequencies are in good agreement with those of the simulated designs.

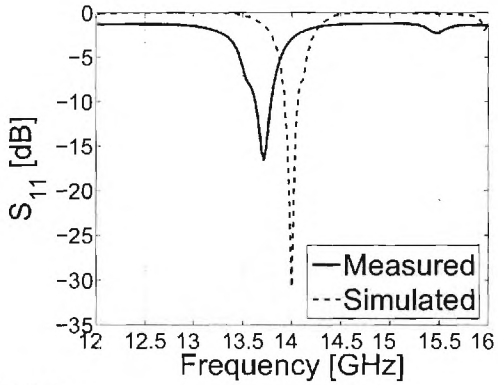

Fig. 34 Return Loss – 14 GHz Array

Table 1 – Impedance Characteristics of the 14 GHz Array

Attribute	Simulated	Measured
Resonant Frequency	**14 GHz**	**13.72 GHz**
Return Loss	**-30 dB**	**-17 dB**
Bandwidth	**140 MHz**	**160 MHz**
% Bandwidth	**1%**	**1.17%**

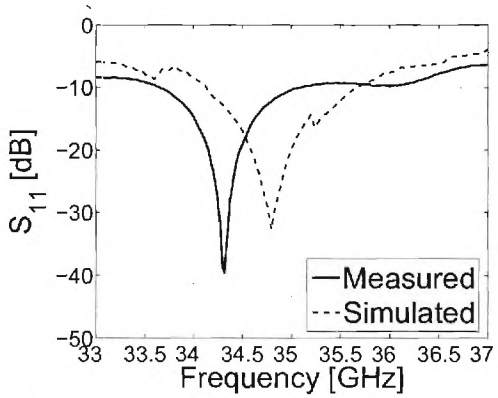

Fig. 35 Return Loss – 35 GHz Array

Table 2 – Impedance Characteristics of the 35 GHz Array

Attribute	Simulated	Measured
Resonant Frequency	**34.87 GHz**	**34.32 GHz**
Return Loss	**-32.5 dB**	**-39.6 dB**
Bandwidth	**1260 MHz**	**1210 MHz**
% Bandwidth	**3.62%**	**3.53%**

Additionally, the simulated and measured 2-D radiation patterns are shown in figures 36(a) and (b) for the E- and H-plane at 14 GHz respectively and figures 37(a) and (b) for the E- and H-plane at 35 GHz respectively. The results are summarized in tables 3 and 4.

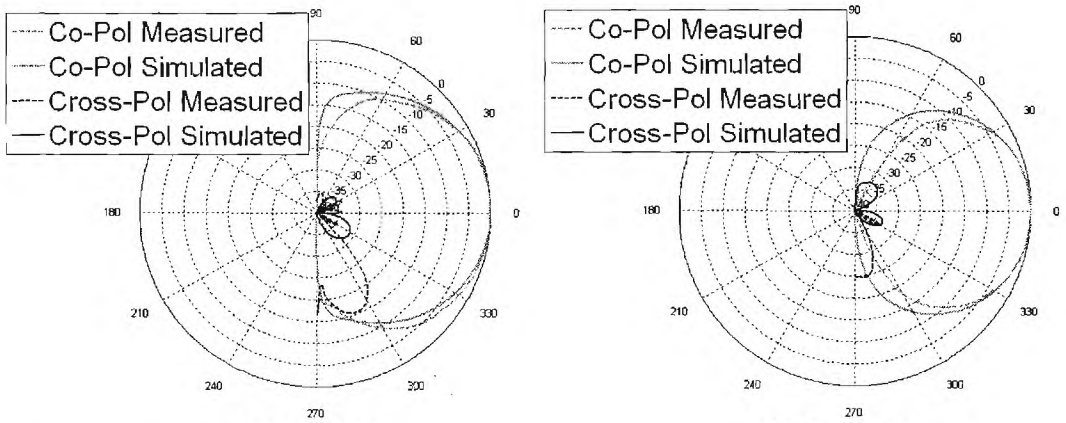

(a) E- Plane (b) H- Plane

Fig. 36 2-D radiation patterns of the 14 GHz array

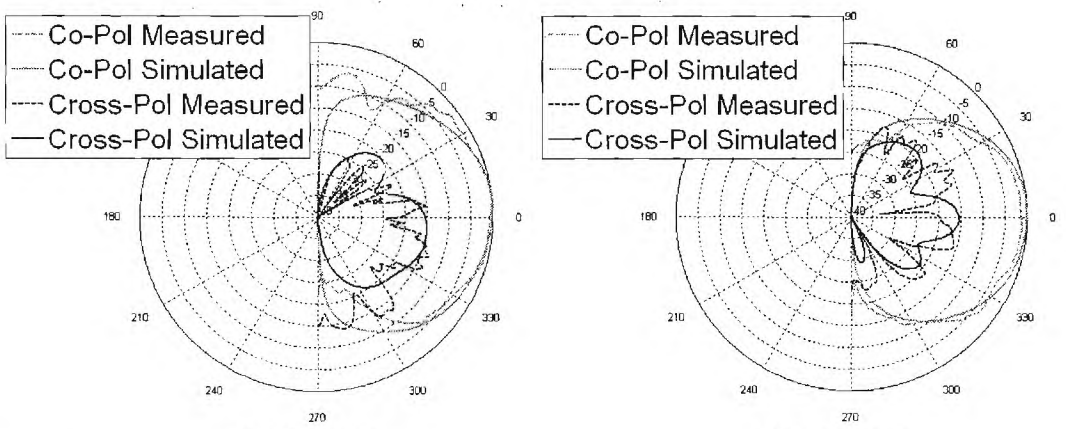

(a) E- Plane (b) H- Plane

Fig. 37 2-D radiation patterns of the 35 GHz array

Table 3 – Radiation Pattern Characteristics of the 14 GHz Array

Characteristic	Simulated	Measured
E-plane –3 dB Beamwidth	**65^0**	**67^0**
H-plane –3 dB Beamwidth	**58^0**	**58^0**
Max. Cross-pol. (E-plane)	**-31 dB**	**-25 dB**
Max. Cross-pol. (H-plane)	**-33 dB**	**-30 dB**

Table 4 – Radiation Pattern Characteristics of the 35 GHz Array

Characteristic	Simulated	Measured
E-plane –3 dB Beamwidth	**65^0**	**66^0**
H-plane –3 dB Beamwidth	**59^0**	**59^0**
Max. Cross-pol. (E-plane)	**-15 dB**	**-14 dB**
Max. Cross-pol. (H-plane)	**-16 dB**	**-15 dB**

The E-plane and H-plane beamwidths and the shapes of the co-polarized patterns are consistent for both the simulated and measured patterns of the arrays. The center-to-center distance can be increased to reduce the E-plane beamwidth to a value close to the H-plane beamwidth, but side-lobes will start to form as a result of this increase. The measured cross polarization levels also agree well with the predicted values for scan angles less than 70^0. The discrepancy at angles above 70^0 is due to the presence of the absorber as explained in the measurement section. To demonstrate the flexibility and mechanical stability of the multilayer LCP substrate, which is one of the key requirements for deployable antennas, antenna arrays were flexed several times and re-characterized. The return loss and radiation patterns were unchanged within the repeatability of the measurement equipment.

The measured results for the 2x1 antenna arrays were quite satisfactory. The cross-polarization level at 35 GHz was the only concern, although the measured results were still comparable to the simulated ones. Admittedly, the design arrangement chosen was relatively simple but it enabled us to demonstrate the applicability of LCP for the development of light-weight and conformal antenna arrays. Once these basic credentials were established, a more complicated architecture was developed to address the shortcomings of the current structure. Specifically, when it was tried to expand the 2x1 array to a 2x2 array that could form a basis for a more general planar array, the cross-coupling between the feed network and the patch elements within an array increased significantly and created disturbances in the radiation pattern. In addition, parasitic resonances were identified and it was quite impossible to minimize cross talk between the feed network of one array and the patch elements of the other array. Several design arrangements were tried but at least a couple of performance characteristics needed to be sacrificed to keep the simple microstrip-fed structure. In order to overcome these issues, a new layer was introduced incorporating just the feed networks for both the 14 and 35 GHz arrays. The development of this aperture-coupled array architecture will be described in the next section.

B.2 Aperture Coupled Patch Antenna Arrays

The developed microstrip fed patch antenna arrays, when expanded into a 2x2 array (the results are not shown here), had two primary shortcomings - Unwanted parasitic coupling between the feed network and the patch elements that led to radiation pattern distortion and the high cross-polarization level for the 35 GHz array. In order to overcome these problems, two improvements were introduced. First, a separate layer was introduced to place the feed networks beneath the ground plane thereby alleviating the parasitic radiation problem. Second, the substrate configuration was changed to place the 35 GHz antennas in the middle layer on a thinner substrate, while placing the 14 GHz

antennas on the top layer. The earlier configuration was chosen to minimize blockage effects on the 35 GHz antennas. However, the cross-polarization problem at 35 GHz is fundamentally dependent on the substrate thickness and improvement is quite difficult using other means, specifically for this dual polarization application. The blockage effects on the 35 GHz antennas, on the other hand, could be reduced by careful placement of antenna elements of both arrays.

B.2.1 Design

The top view (with all the layers interlaced) and the side view of the aperture coupled antenna array are shown in figure 38. The metal, used in simulation and fabrication, for the ground plane and the antenna elements is copper (Cu) and had a thickness of 18 μm. The total substrate thickness for this configuration is 18 mils. The radiating elements for both arrays are placed on one side of the ground plane, while the feed network for both arrays is placed on the other side. The ground plane itself contains slots through which energy is electromagnetically coupled from the feed network to the patches. The 35 GHz patches are placed on a 5-mil thick LCP substrate, while the 14 GHz patches are placed on a 14-mil thick LCP substrate. The feed network for both patches is placed on a 4-mil thick LCP substrate on the other side. These substrate choices are a result of extensive analysis of their influence on antenna performance and were chosen to provide similar radiation patterns for both arrays while keeping a compact profile.

As shown in the figure, a combination of series and parallel feed was employed to form the 2x2 array. Each 2x2 array consists of two linear 2x1 arrays and the linear 2x1 arrays are formed by combining two basic elements, which we will define as 'End element' and 'Any element'. The development of the 2x2 array from these basic elements is explained in figure 39.

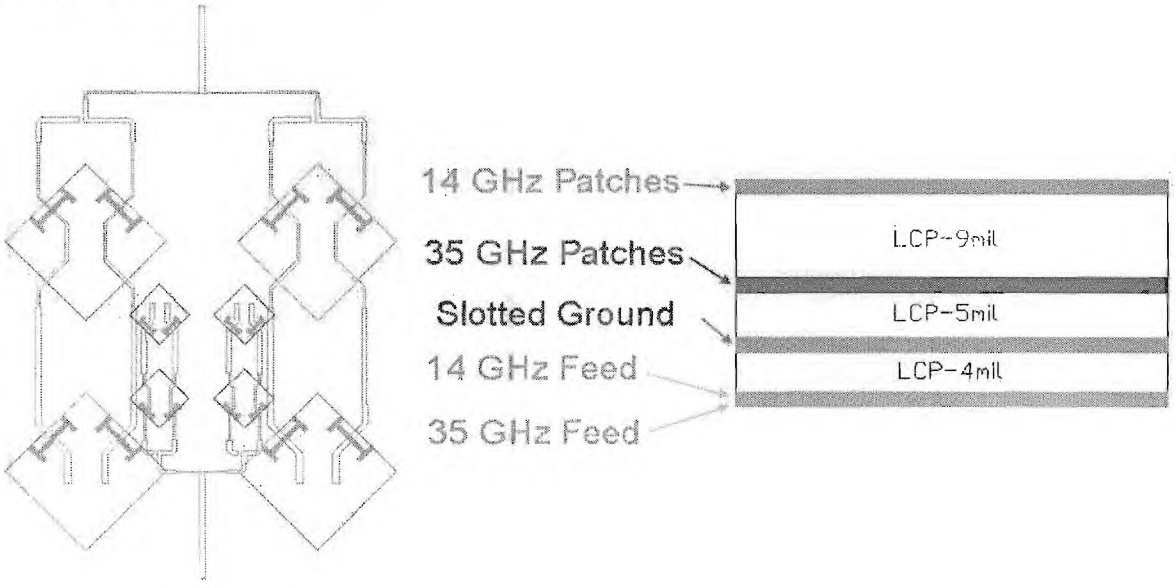

Fig. 38 Aperture Coupled Antenna Array, [L] Top View, [R] Side View

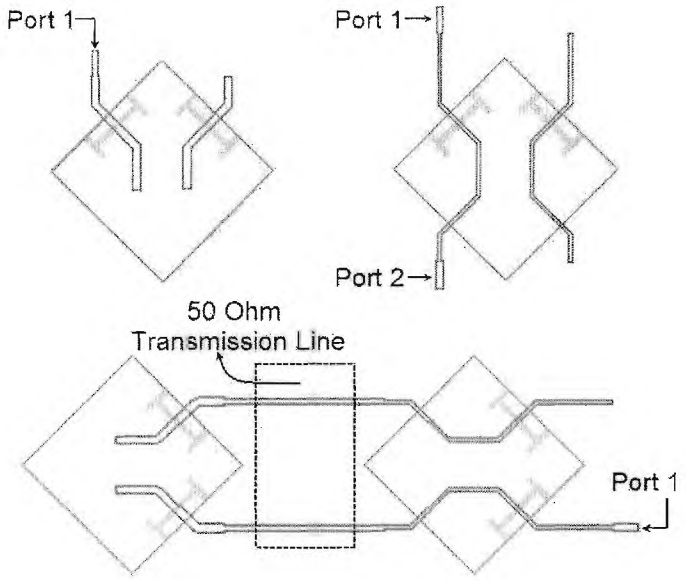

Fig. 39 Development of the Aperture Coupled Array. Top Left: 1-port 'End Element'. Top Right: 2-port 'Any Element'. Bottom: Linear Array with one 'End Element' and one 'Any Element'. Several such linear arrays can be combined using a corporate feed to form a planar array [Refer Fig. 1]. The parallel feed line without ports in each case is for exciting the orthogonal polarization making this a dual-polarization system.

The 'End element' as the name suggests is the last element in the linear array (from the feed direction). It is a 1-port device with its patch and feed dimensions optimized to resonate at the desired frequency. The simulated return loss characteristics of the 'End element' resonating at 14 GHz is shown in figure 40. The 'Any element' is a 2-port device designed to provide a matched load at the resonant frequency at port 1 when port 2 is terminated with a matched load. The simulated S-parameter characteristics of the 'Any element' for the 14 GHz array is shown in figure 41. The linear array is, then, formed by connecting port 1 of the 'End element' to port 2 of the 'Any element'. Since, the 'End element' is designed to resonate at the desired frequency, it presents a matched load at port 2 of the 'Any element' at the resonant frequency, which in turn makes the linear array resonate at the desired frequency. It can be noticed in figure 4 that the insertion loss is close to -3 dB at the resonant frequency. The feed network and the slots for the 'Any element' are optimized in this case to provide equal amplitude split between antenna elements in a 2x1 linear array. A 50 Ω constant impedance transmission line is connected between the elements to maintain an appropriate distance between them in an array configuration. Since both the elements are matched to 50 Ω, the length of the transmission line can be used to control important radiation characteristics such as directivity, beamwidth, and broadside angle of the array. The 2x2 array is formed by combining two linear arrays using a corporate feed network. It is also possible to realize a general Nx1 linear array by adding (N-1) 'Any elements' to an 'End element' and subsequently an NXN planar array.

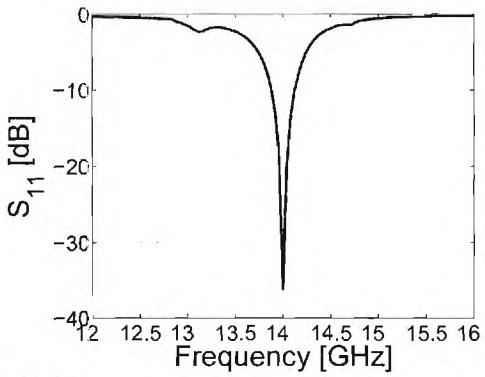

Fig. 40 Return Loss – End Element

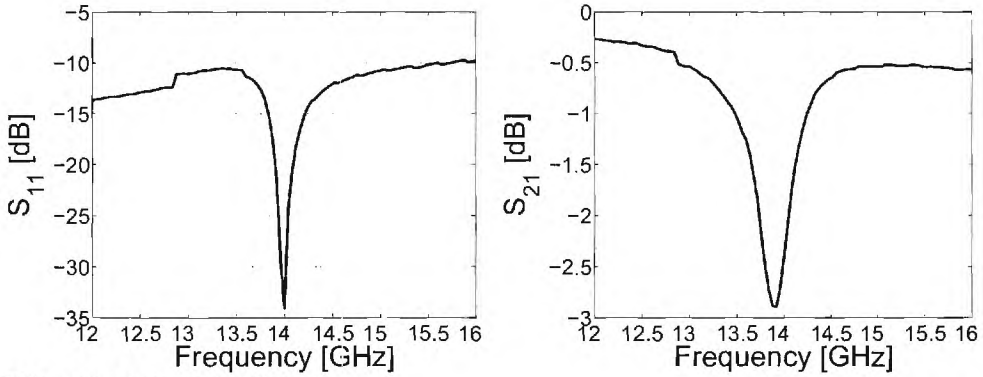

Fig. 41 S-parameters – Any Element

B.2.2 Fabrication and Measurement

The fabrication and measurement procedure is similar to the one explained in section B.1.2 and B.1.3. Figure 42(a) shows the individual patterned layers of the aperture coupled array before bonding and figure 42(b) shows the array after bonding.

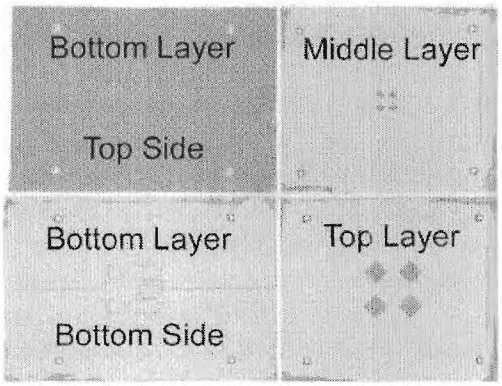

(a) Individual Layers – Before Bonding

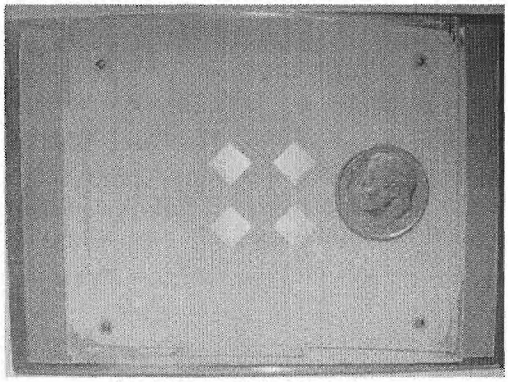

(b) Arrays – After Bonding

Fig. 42 Photo of the fabricated aperture coupled arrays

B.2.3 Results

The simulated and measured return loss results of the 14 GHz array is shown in figure 43. An excellent agreement has been achieved. The impedance characteristics are summarized in table 5. Figure 44 shows the return loss results for the 35 GHz array and table 6 summarizes the impedance characteristics. Although the measured return loss results agree very well with those of the simulations for the 14 GHz array, discrepancies can observed for the 35 GHz array. Specifically, there is a shift in the resonant frequency that could have arisen from fabrication tolerances. The margin for error is very little at mm-wave frequencies (such as 35 GHz) and especially for this multilayer design where precise alignment of the feed network, electromagnetic slots and the radiating patches is crucial.

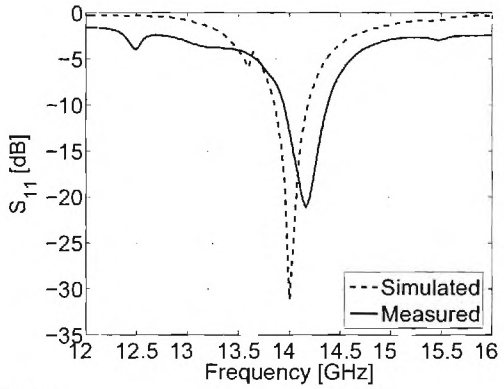

Fig. 43 Return Loss – 14 GHz Array

Table 5 – Impedance Characteristics of the 14 GHz Array

Attribute	Simulated	Measured
Resonant Frequency	**14 GHz**	**14.16 GHz**
Return Loss	**-31 dB**	**-21 dB**
Bandwidth	**280 MHz**	**320 MHz**
% Bandwidth	**2%**	**2.28%**

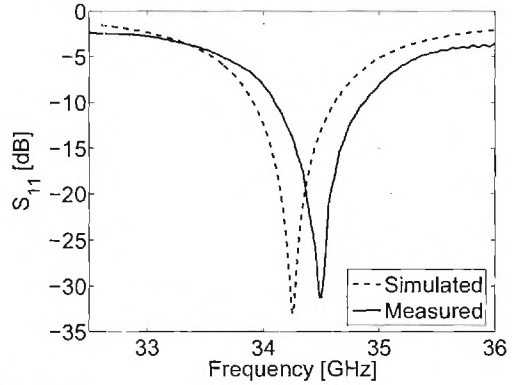

Fig. 44 Return Loss – 35 GHz Array

Table 6 – Impedance Characteristics of the 35 GHz Array

Attribute	Simulated	Measured
Resonant Frequency	**34.25 GHz**	**34.5 GHz**
Return Loss	**-33 dB**	**-32 dB**
Bandwidth	**710 MHz**	**720 MHz**
% Bandwidth	**2%**	**2%**

The 2-D radiation pattern results for the 14 GHz are shown in figures 45(a) and 45(b). The radiation characteristics of the 14 GHz array are summarized in table 7. The 2-D radiation pattern results for the 35 GHz are shown in figures 46(a) and 46(b). The radiation characteristics of the 35 GHz array are summarized in table 8. Again, the simulation and measured results agree very well.

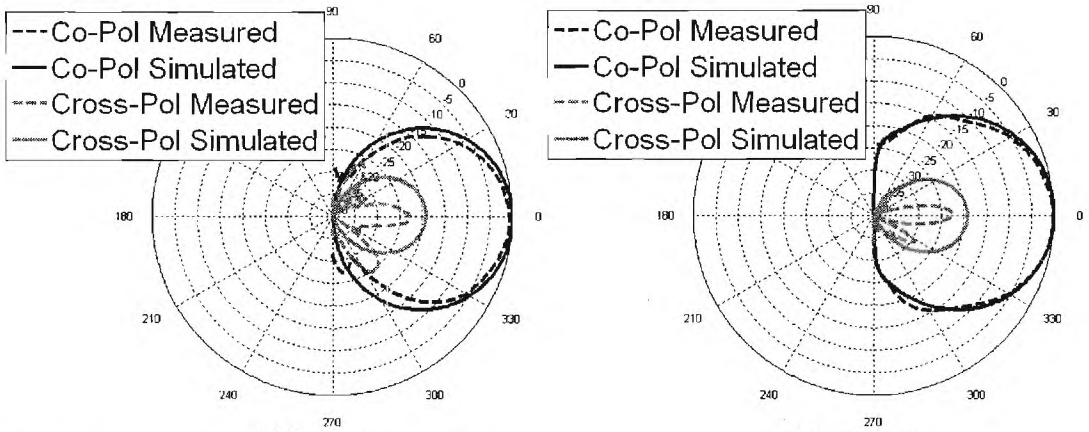

(a) E- Plane (a) H- Plane

Fig. 45 2-D radiation patterns of the 14 GHz array

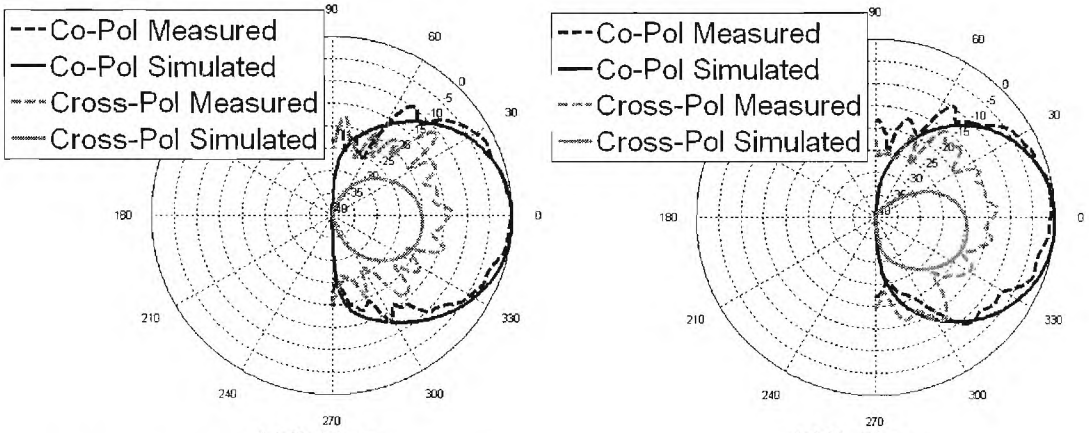

(a) E- Plane (a) H- Plane

Fig. 46 2-D radiation patterns of the 35 GHz array

Table 7 – Radiation Pattern Characteristics of the 14 GHz Array

Characteristic	Simulated	Measured
E-plane –3 dB Beamwidth	**49^0**	**48^0**
H-plane –3 dB Beamwidth	**46^0**	**45^0**
Max. Cross-pol. (E-plane)	**-19 dB**	**-21 dB**
Max. Cross-pol. (H-plane)	**-19 dB**	**-21 dB**

Table 8 – Radiation Pattern Characteristics of the 35 GHz Array

Characteristic	Simulated	Measured
E-plane –3 dB Beamwidth	**51^0**	**49^0**
H-plane –3 dB Beamwidth	**52^0**	**55^0**
Max. Cross-pol. (E-plane)	**-18 dB**	**-14 dB**
Max. Cross-pol. (H-plane)	**-18 dB**	**-14 dB**

The E-plane and H-plane beamwidths and the shapes of the co-polarized patterns are consistent for both the simulated and measured patterns of the arrays.

B2.4 Efficiency Calculations

Apart from the return loss and the radiation pattern measurements, efficiency measurements were also carried out. The efficiency of the 2X2 14 GHz aperture coupled array was measured using the Wheeler Cap method with cap dimensions of 10.8 mm x 34 mm x 65 mm. The efficiency is calculated based on input resistance measurements. The input resistance is measured with and without the cap so that radiation resistance and loss resistance can be separated. This method is simple but is known to work well for patch antennas. The measured efficiency of the entire setup that includes the array, the feed network and the connector was 58.6%. In order to determine the efficiency of the antenna array only, it is necessary to de-embed the mismatch loss, the loss of the feed lines and the connector. The return loss plot of the array shows that the mismatch loss is negligible. In figure 40(a) it can be seen that the input feed line has been extended to facilitate scattering parameter and radiation pattern measurements. The losses of the extended feed line and the corporate feed network are determined by simple simulations using ADS-momentum. The typical connector loss at 14 GHz is 0.15 dB. After de-embedding these losses, the efficiency of the antenna array is found to be 76.4%. Table 9 shows a summary of the measured efficiency, specific losses and the de-embedded efficiency.

Table 9 – Efficiency of the 14 GHz array

Attribute	***Efficiency/ Loss***
Measured Efficiency	58.6%
Mismatch Loss (dB)	**0.00 (100%)**
Connector Loss (dB)	**0.15 (96.6%)**
Feedline Loss (dB)	**1.00 (79.5%)**
Total Loss (dB)	**1.15 (76.7%)**
De-embedded Efficiency	76.4%

The results shown here demonstrate the applicability of LCP for the development of low cost, lightweight, and conformal antennas for communication and remote sensing systems operating up to mm-wave frequency ranges. All the results shown are for one polarization, but they are the same for the other orthogonal polarization also because of

the symmetric arrangement of radiating elements and the feed network. Thus the designs can function as a dual frequency and dual polarization antenna array system. The results shown thus far are for arrays implemented as "hard-wired" designs. To realize a polarization reconfigurable system (i.e. to switch between polarizations in real-time), switches need to be integrated with the current arrays. To achieve this, the feed networks for the arrays were modified to include bias stubs for the switches.

B.3 Antenna Arrays with MEMS switches for polarization reconfigurability

Figure 47 shows the top view of the designed arrays for integration with MEMS switches. The location and the orientation of the bias stubs are slightly modified for the 35 GHz case since the available space is limited. This configuration also minimizes the interaction between various stubs and the feed network. The total length of each radial stub is adjusted to produce an open at the operating frequency. The transformers and the combiners of the corporate feed network were optimized to minimize the effects of the bias stubs on the resonant frequency of the arrays.

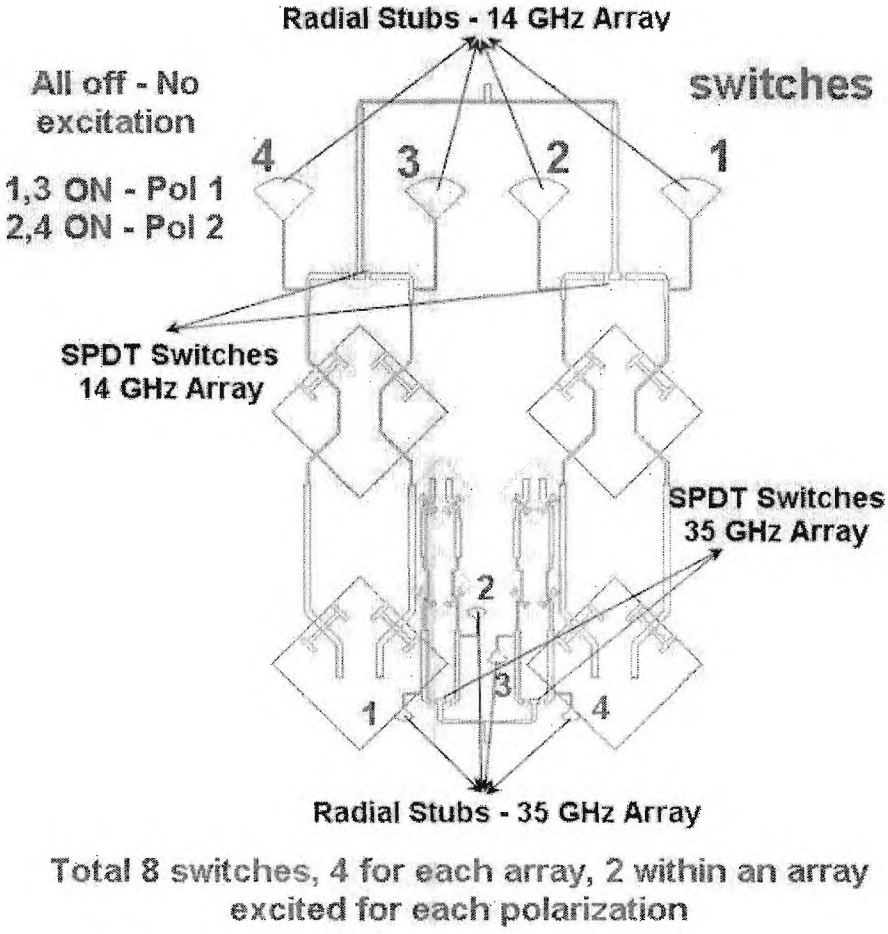

Fig. 47 Top View of the aperture coupled arrays with biasing stubs for MEMS integration

The measured return loss results for different switch configurations are shown in figures 48 and 49.

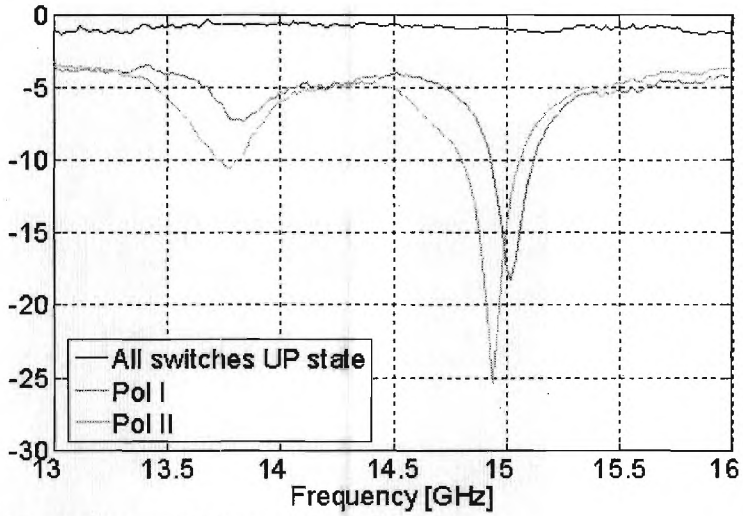

Fig. 48 Measured Return Loss – 14 GHz Array with MEMS

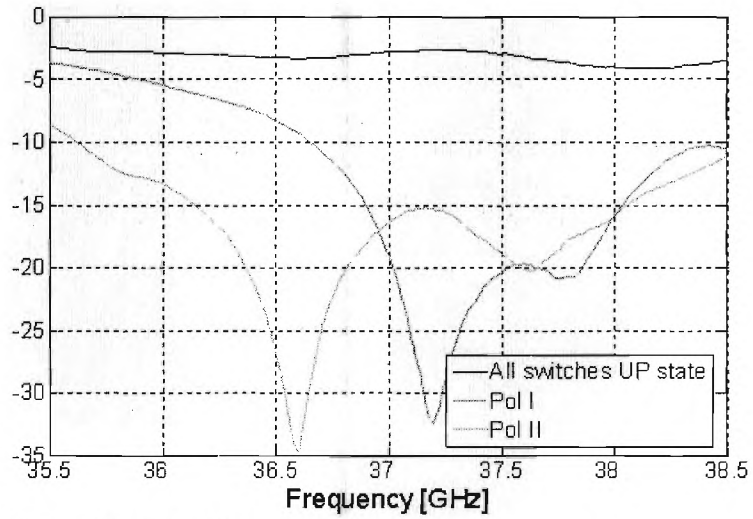

Fig. 49 Measured Return Loss – 35 GHz Array with MEMS

A considerable shift in the operating frequency can be noted in each case. We believe that the shift is due to dispersion of dielectric constant of the substrate. This assessment is based on our study on the sensitivity of the resonant frequency of this type of antennas to the dielectric constant (section A 3.3). LCP available from Rogers Corporation and used for fabrication of these MEMS arrays belonged to a new batch and could have had a lower dielectric constant compared to the older batches, whose characterization formed the basis for designing these arrays. Another reason for the resonance shift could be the capacitive MEMS switches whose effect has not been simulated.

Figure 50 shows the setup used for measuring the return loss of the arrays with MEMS. CPW-μstrip transition was used and a TRL calibration setup was utilized to de-embed the effects of the transition. Figure 51 shows a close-up view of the fabricated MEMS switches.

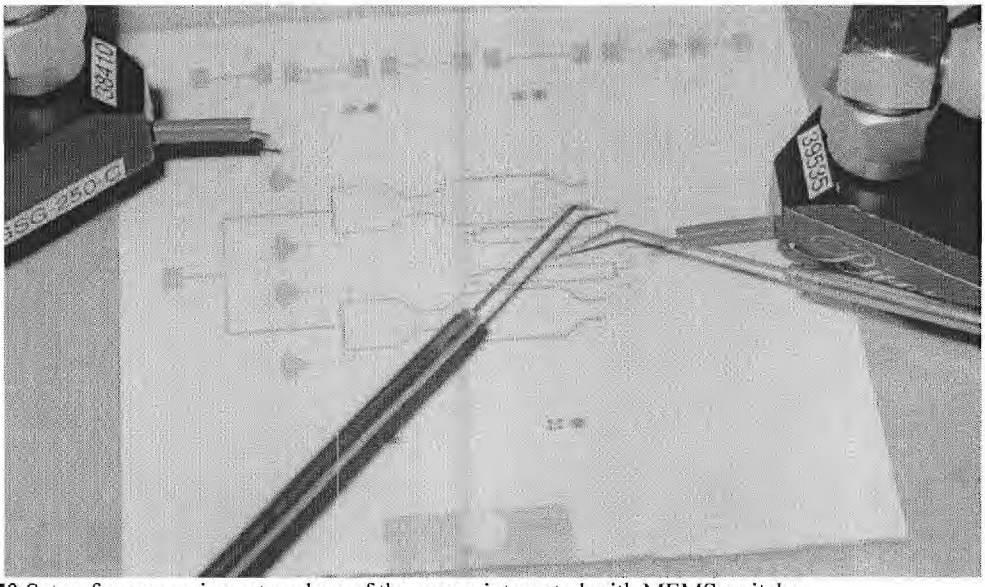

Fig. 50 Setup for measuring return loss of the arrays integrated with MEMS switches

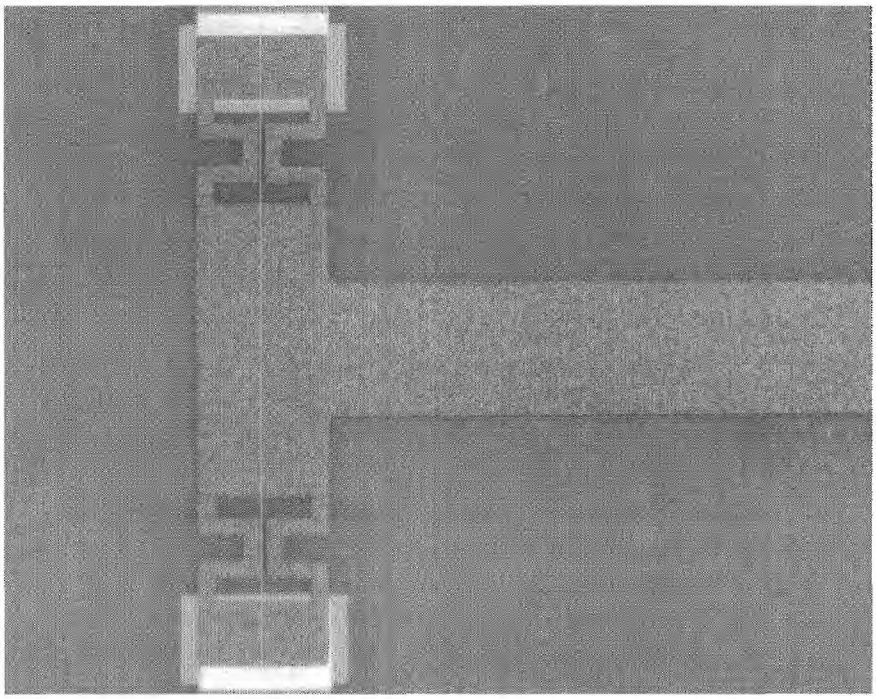

Fig. 51 Close up view of the fabricated switches

The MEMS integrated array was characterized on a modified, microwave antenna probe station that allowed the antenna to radiate downward while the microstrip line was excited on the upper side of the substrate by a microwave probe. The antenna under test (AUT) was characterized as the receive antenna and a Ka-Band horn antenna was used as the transmit antenna. The separation between the two antennas was 27.3 cm. The antennas were first characterized as received before bias and after biasing switches 1 and 3. The results are plotted in figure 52.

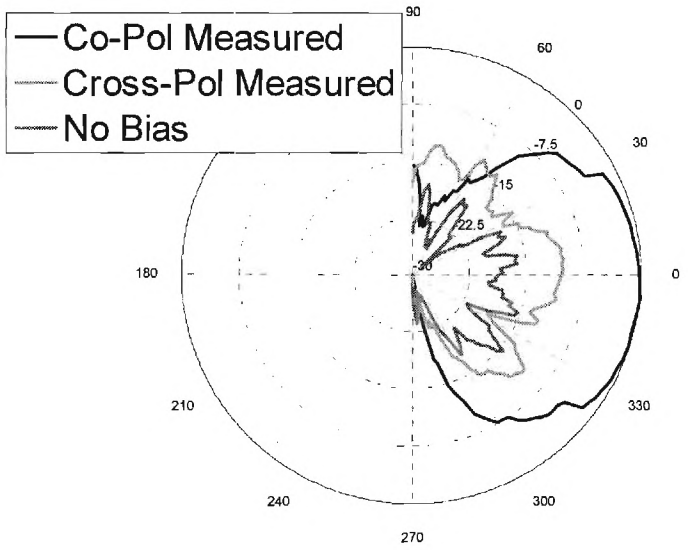

Fig. 52 Measured radiation pattern of the MEMS integrated 35 GHz array

The maximum cross polarization value measured is -10 dB. One of the reasons for a lower cross polarization value for the MEMS integrated arrays as compared to the hard wired arrays could be the isolation provided by the MEMS switches. This is clear from the radiation plot, where the maximum radiated power when the switches are unbiased stood at only 15 dB down from the co-polarization maximum.

C. RF MEMS Switches and Phase Shifters

C.1 Packaged RF MEMS Switch

Capacitive RF MEMS switches in both shunt and series configurations were developed on LCP substrate during this project. An additional layer of LCP with micromachined "enclosure cavities" was also used for packaging the switches. The general concept and results for this section of research is presented graphically in Figures 52-56. As it is shown, the capacitive MEMS switches have very low loss (<0.4 dB up to 35 GHz) and the LCP package adds no additional loss to the switch. The maximum isolation of the packaged switch is around 50 dB at 26 GHz.

Fabricating on a flexible, organic substrate is not as straight-forward as using a smooth, flat substrate like silicon. Being a flexible material, it is prone to curling. This effect becomes more pronounced throughout processing due to the fluctuation of temperature from the various baking, deposition, and etching steps. Since optical lithography with a 3-5 micron resolution can not be performed on a curled substrate, it is necessary to mount the sample to a flat, cleanroom grade material before processing. Temporary mounting can be done using a spin-on or roll-on adhesive. Permanent mounting can be done using a thermal bonding technique. Alternatively, if a mask aligner with a vacuum chuck is available, then no mounting is necessary.

Since the substrate is also an organic polymer, surface roughness is an issue. The surface roughness of bare LCP is usually on the order of 2-5 microns. Given that the switch membrane is generally suspended 2-3 microns above the substrate, the surface roughness can be large enough to prevent the switch from deflecting. To solve this problem, each sample is mechanically polished using a commercially available alumina slurry. It takes less than an hour to polish a four inch circular sample. After polishing, the sample will have a surface roughness between 10-50 nm, which is smooth enough for MEMS switch operation.

After polishing and mounting to a flat material, the following procedure was used in fabricating the MEMS switches. First, a 300A titanium- 2500A gold layer was electron beam evaporated, patterned, and etched using chemical etchants. This is to provide the transmission line metal. Second, a 2000A silicon nitride layer was deposited using low-temperature Plasma Enhanced Chemical Vapor Deposition (PECVD). Third, the silicon nitride was patterned and etched using a Reactive Ion Etch (RIE) process everywhere except for the MEMS switch contact areas. Fourth, a 2-3 micron thick photoresist layer was patterned to provide a sacrificial layer for the membrane. Fifth, gold was evaporated, patterned, electroplated to a thickness of 2 microns, and etched to create the membrane. Sixth, the sacrificial layer was dissolved using photoresist stripper leaving the membrane suspended above the signal lines. Finally, the switches were dried using carbon dioxide at the supercritical point to prevent membrane collapse due to water surface tension.

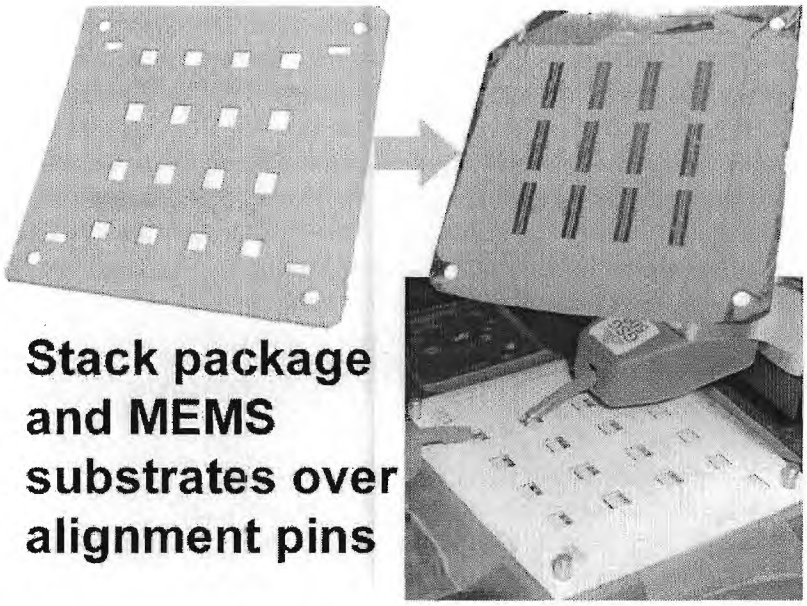

Fig. 53 Top left: LCP superstrate packaging layer with holes for alignment and probe feed-throughs. The packaged cavities between each set of probing holes are visible due to LCP becoming partially transparent at a 2 mil thickness. **Top right:** CB-FGC transmission lines with air-bridge RF MEMS switches in the center of the transmission lines. **Bottom right:** Both layers stacked on alignment fixture and probed through the feedthrough windows.

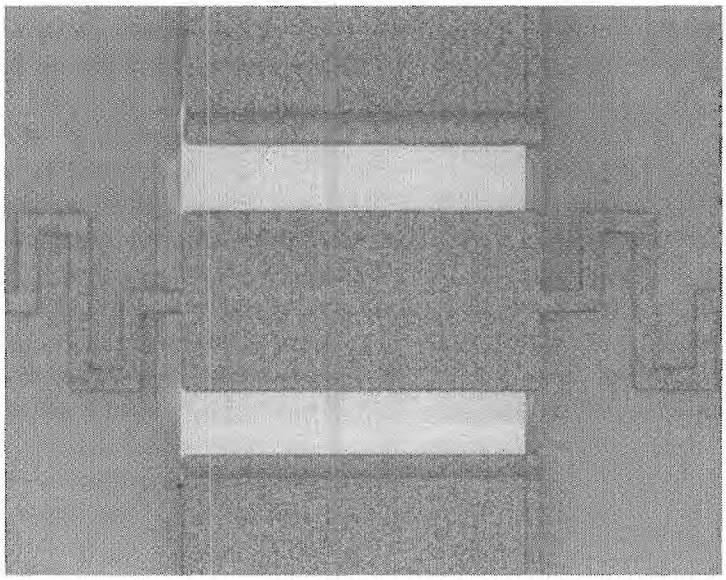

Fig. 54 Fabricated RF MEMS switch on LCP substrate.

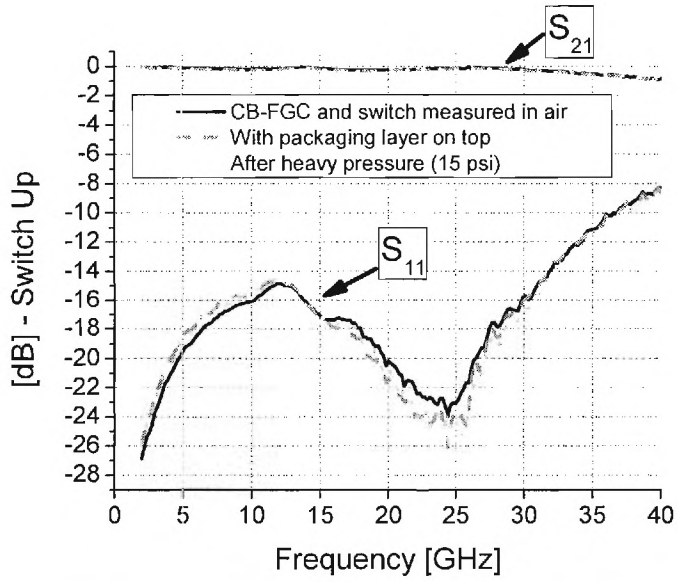

Fig. 55 Comparison of S-parameter measurements of an air-bridge type CB-FGC MEMS switch in the "UP" state. Case 1: The switch is measured in open air. Case 2: The packaging layer is brought down and taped into hard contact and measured. Case 3: A top metal press plate and a fifteen pound weight are put on top of the packaging layer (15psi) to simulate bonding pressure. The weight and the press plate are then removed and the switch is re-measured.

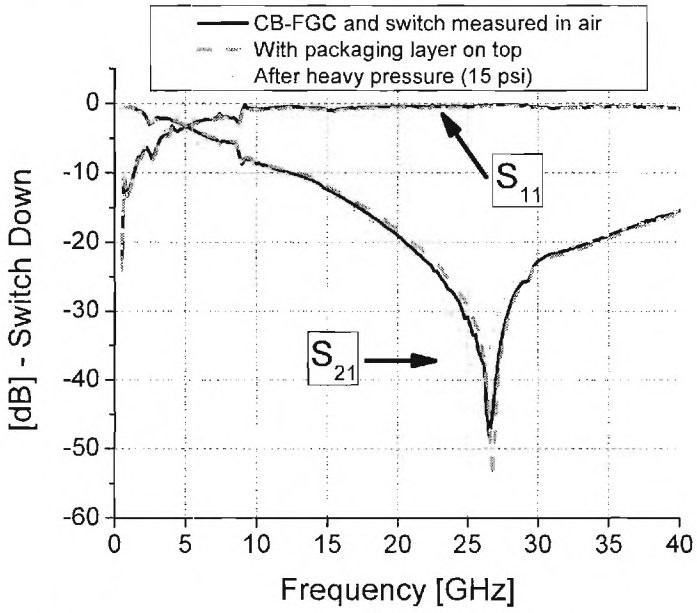

Fig. 56 Comparison of S-parameter measurements of an air-bridge type CB-FGC MEMS switch in the "DOWN" state. The three measurement cases shown are the same as those explained in the caption for Fig. 54.

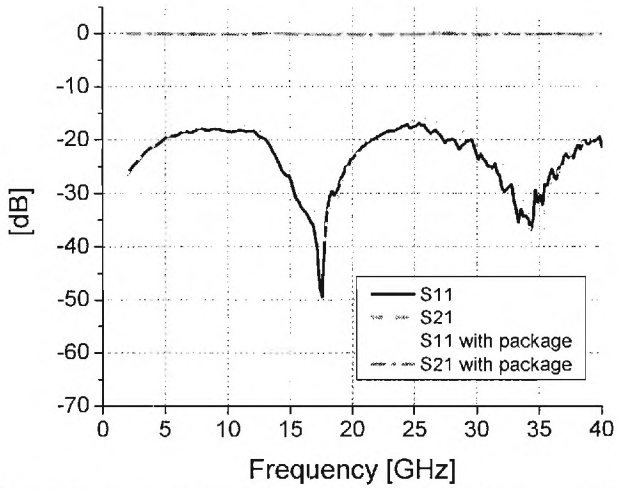

Fig. 57 Comparison of S-parameter measurements of the MEMS switch transmission line after the switch was physically removed. The cases with the package and without the package layer are nearly the same.

C.2 4-Bit MEMS Phase Shifters

For the first time a four-bit MEMS phase shifter was realized on an organic, flexible, low permittivity material. A microstrip switched-line phase shifter was optimized at 14 GHz for small size and excellent performance. The improved geometry of the reduced size phase shifter is 2.8 times smaller than a traditional switched-line phase shifter and is much less lossy. For the four-bit phase shifter, the worst case return loss is greater than 19.7 dB and the average insertion loss is less than 0.96 dB (0.24 dB/bit or 280°/dB) at 14 GHz. The average phase error at 14 GHz is only 3.96°.

General Phase Shifter Design

The LCP material used has a thickness of 100 μm, a permittivity (ε_r) of 3.1, and a tan δ of 0.004. The phase shifter offers phase shifts between 0° and 337.5° in 22.5° increments (16 cases). Traditional microstrip theory was used to design the phase shifter. A layout of the final four-bit phase shifter is shown in the figure below.

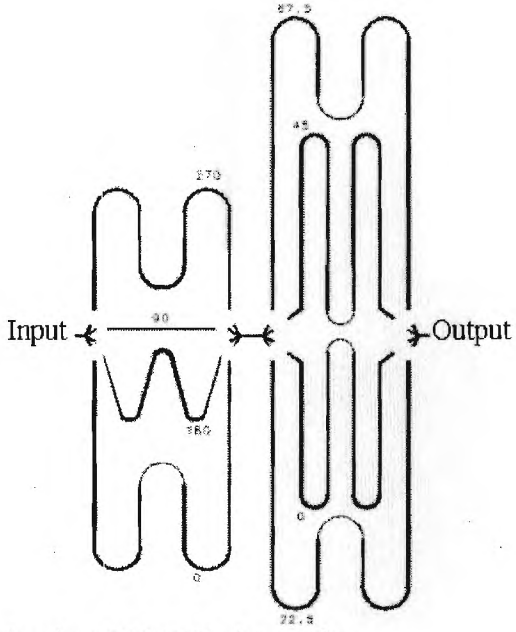

Fig. 58 Top view of 4-bit series-shunt RF MEMS phase shifter

In order to apply the necessary bias voltage to actuate the MEMS switches, bias pads were designed and placed on each of the signal paths (not shown in the figure above). When a DC voltage is applied to the bias pad, electrostatic force pulls the switches (which are DC grounded) towards the signal line. A layer of silicon nitride deposited over the signal line prevents switch metal to signal line metal contact. Therefore, no DC current can flow but the capacitance between the switch and the signal line is large enough for RF energy to pass through.

Reduced-size Methodology

Switched-line phase shifters are widely used because they are straight-forward to design, fabricate, and integrate with other microwave devices. Unfortunately, the overall size of the switched-line geometry is comparable to the wavelength for each bit. Since multibit phase shifters are usually desired, this can result in a phase shifter that is much larger than the other microwave components in an RF system. For this reason, a number of changes were made to the traditional layout to decrease the size. These design changes are detailed below. By incorporating these layout changes, the overall area was reduced by a factor of 2.8. The length was reduced by a factor of four. In addition to the size reduction, the signal line length and number of MEMS switches traversed compared to a traditional implementation were each reduced by a factor of two. This results in half the line loss and half the switch loss by using this implementation. A size comparison of the modified layout compared to a traditional layout is shown below.

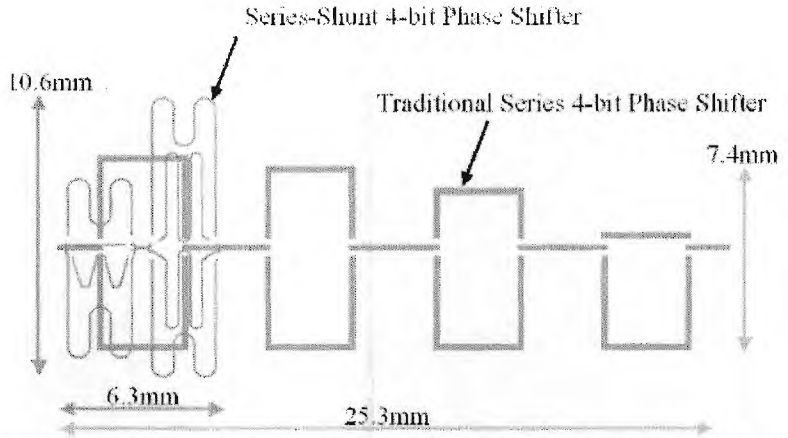

Fig. 59 Size comparison of 4-bit series-shunt design with traditional series switched-line phase shifter on LCP at 14 GHz

Series-Shunt Modification

Instead of cascading four one-bit phase shifters in series (as demonstrated in the figure above), four shunt phased paths were cascaded with another four shunt phased paths (hence the series-shunt distinction). In order to generate all sixteen possible cases, a 0° reference path must occur in every series portion of the phase shifter. In addition, the 0°, 90°, 180°, and 270° phased paths must be in one section and the 0°, 22.5°, 45°, and 67.5° phased paths must be in another section to create all 16 cases. In order to make this feasible for really short phased paths (like the 22.5° case) and really long phased paths (like the 270° case), the shortest phased paths were elongated by a wavelength. This is why the smallest phase shifts have longer line lengths than the largest phase shifts.

High Impedance Modification

Instead of using the standard 50Ω input impedance, 100Ω was used. By making this change, the signal line width decreased from 240 μm to 65 μm. This allowed for more signal lines to be placed in less area. In practice, high impedance patch antenna arrays that would utilize this type of phase shifter are common. However, a 50Ω to 100Ω transition could be added for integration with other standard microwave components.

Curled Signal Line Modification

Instead of using the traditional rectangular phased paths, the lines were curled inward to minimize the overall area. Careful attention was given to minimize coupling between the signal lines. A full wave HP-ADS Momentum (method of moments) simulation was performed to determine the amount of coupling between line segments. It was determined that as long as the lines were more than 300 μm apart, the amount of coupling would be sufficiently small to prevent crosstalk.

Impedance Matching

Since curved microstrip lines are being used to reduce the size, impedance matching must be done to compensate for the additional parasitic impedance. Instead of using additional matching devices, such as stubs, all impedance matching was handled through the signal lines themselves. Lines that require a higher impedance match were made

thinner and lines that require a lower impedance match were made wider. All impedance matching was performed using a full-wave simulator. Since the arcs are the shortest part of the signal line, they were used to do the impedance matching. The impedance was varied until the lowest insertion loss was achieved. The overall size of the circuit does not change by using this method of impedance matching. The optimized impedance values for a section of the phase shifter are shown in the figure below.

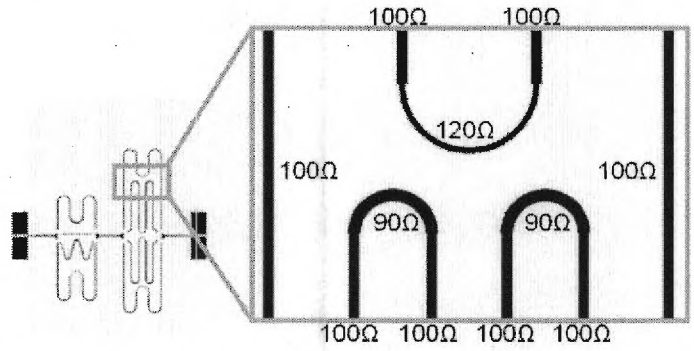

Fig. 60 Optimal impedance values for a section of the phase Shifter

Tree-Junction Design

To simplify the design and fabrication process, all of the MEMS switches are single-pole four-throw (SP4T). Since one signal must be split among four different phased paths, a four-way Y-junction (or tree-junction) was designed. The geometry of the tree-junction used is shown in the figure below.

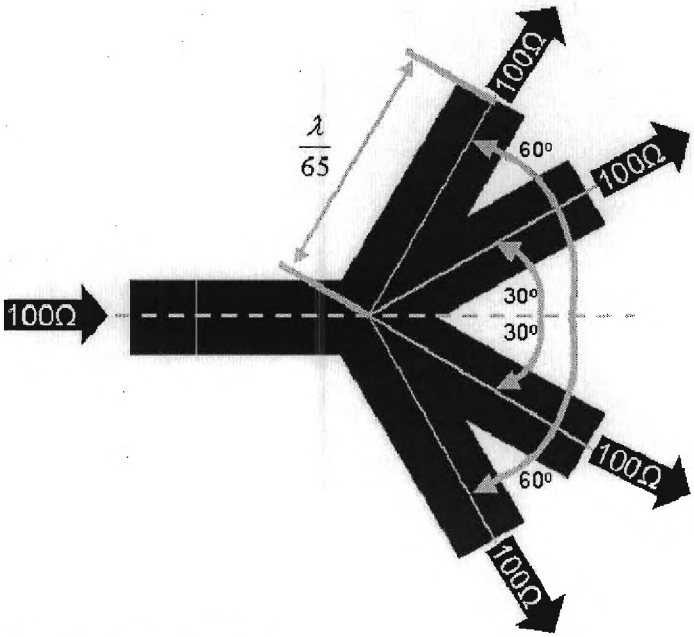

Fig. 61 Design geometry for the tree-junction

Each of the four output stubs are the same width as those of the other signal lines and are λ/65 long at the design frequency (or 220 μm). This is sufficiently small to prevent RF energy from entering the stubs that are associated with non-activated MEMS switches (that is, in the up state). Using longer lines increases the amount of leakage power into these stubs. Using shorter stubs forces the layout to be too dense. The λ/65 length is optimal for this particular layout. However, a good rule of thumb is to use line lengths less than λ/25 to avoid excessive leakage power. Fine-tuning can be done using a full-wave simulator.

Each stub is placed at 30° or 60° off the main axis. These values can vary, but symmetry across the main axis is necessary for symmetric distribution of power. Very wide angles can be used with very short stubs to prevent layout crowding (as in this case). Alternatively, very narrow angles can be used with long stubs to keep the layout small. To demonstrate that the angle can vary without greatly effecting the performance, a full wave simulation was run with one stub that varies the bend angle from 0° to 90°. The results are shown in the figure below.

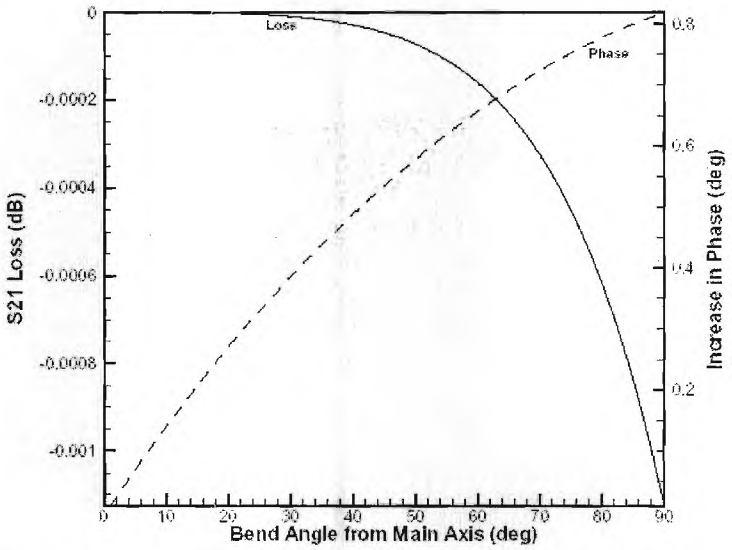

Fig. 62 S21 loss and phase data for one stub of the tree-junction versus the bend angle

For all angles between 0° to 90°, the effect of the bend is negligible. The additional phase increase from the bend discontinuity is 0.39° and 0.66° for the 30° and 60° bends, respectively. The additional insertion loss is too small to measure.

Simulation Results

A full-wave simulation was performed using HP-ADS Momentum for the 4-bit phase shifter. The design was optimized for low-loss and a phase error less than three degrees. S11 and S21 simulation results for four of the sixteen possible phase shifts are shown in the figure below.

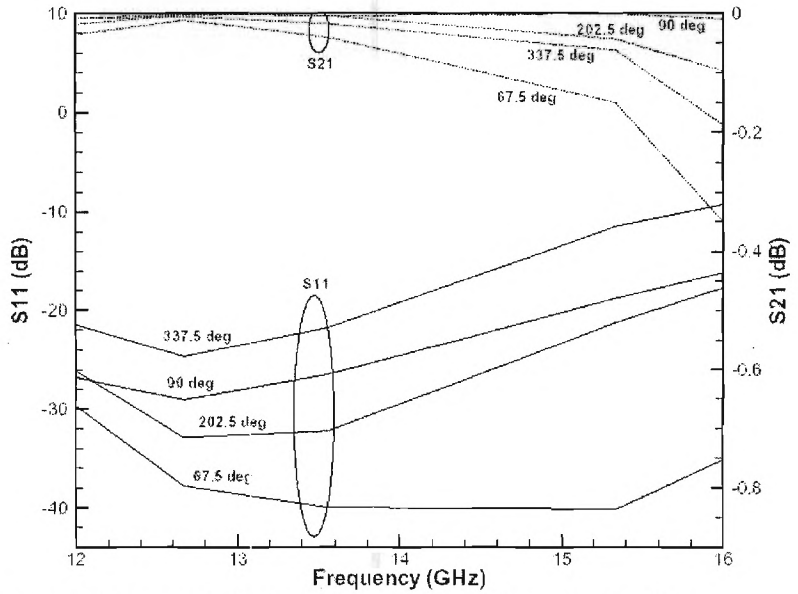

Fig. 63 Full-wave simulation results for four of the sixteen possible phased paths

As expected, the phased paths with the longest lengths have more insertion loss than the shorter phased paths. The 67.5° configuration has the longest signal line length and the 90° configuration has the shortest signal line length in the system. The MEMS switch and metal losses were not modeled in these simulations. Therefore, it is expected that the insertion losses shown will be much less than the measured results.

Measurement Results

Measurement results were taken using high impedance DC probes to apply the switch bias voltage. Thru-Reflect-Line (TRL) calibration was performed on wafer to remove the connector and cable losses. The loss measurement results for the four-bit MEMS phase shifter are shown in the figure below. The worst case S11 is -20.8 dB and the average S21 is -0.95 dB at 14 GHz. This is a per-bit insertion loss of only 0.238 dB.

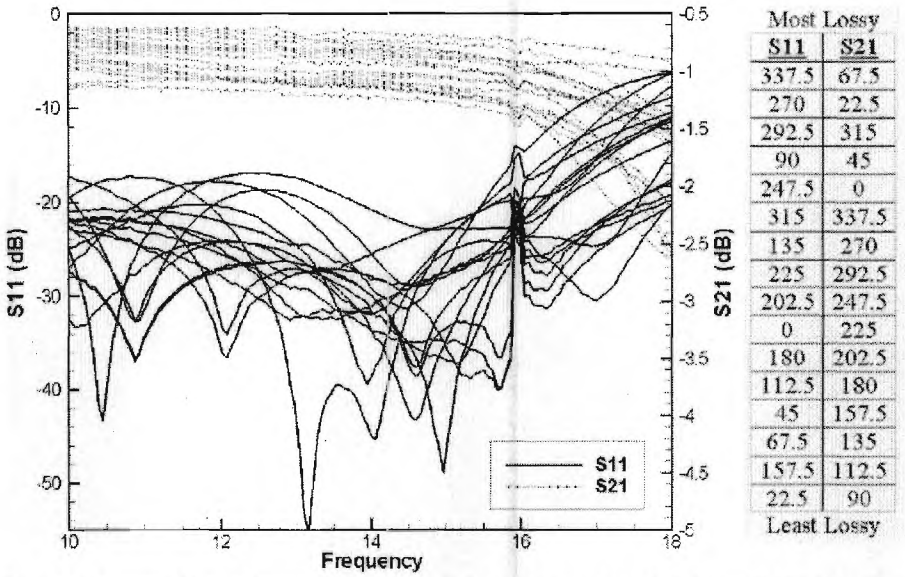

Fig. 64 Measured loss of unpackaged phase shifter. The order of the lines is listed from most lossy to least lossy at 14 GHz

The phase error measurement results are shown in the figure below. The average phase error at 14 GHz is 3.96 degrees.

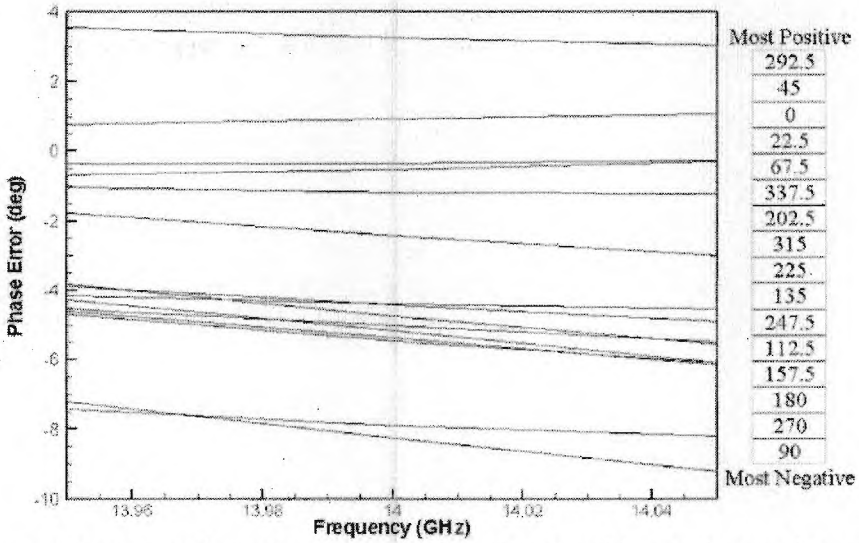

Fig. 65 Measured phase error of unpackaged phase shifter. The order of the lines is listed from most positive to most negative at 14 GHz

Phase Shifter Packaging

The ideal method of packaging the MEMS phase shifter is to use thermocompression bonding. This involves melting a layer of low-melt LCP between two layers of high-melt LCP at 300°C. Unfortunately, MEMS switches experience plastic deformation above 200°C and they are unusable after being exposed to temperatures over 230°C. Instead, the

three layers of LCP were bonded together using an epoxy. This method proved to be fast, simple, and low-loss.

The spray adhesive used for epoxy bonding is Super 77 by 3M. The thickness of the epoxy is approximately 100μm, which is about the same thickness as the substrate layer. The permittivity of the material is unknown but it must be similar to that of LCP since its presence has little effect on the performance. The additional insertion loss from the epoxy is 0.087 dB at 14 GHz.

The phase shifter signal lines and MEMS switches are fabricated on the LCP substrate. A piece of 25μm thick LCP bond ply layer is placed on top of the fabricated substrate. This layer is electrically the same as the thicker 100μm material. To prevent the MEMS switches from being damaged by the superstrate LCP layer, cavities were laser-micromachined to expose each of the MEMS devices using a CO_2 laser. These cavities align with the switches on the substrate layer to create an opening large enough and deep enough to prevent contact between the switches and the cavity walls. On top of these two layers of LCP, a third (superstrate) layer of 100μm thick LCP is stacked to complete the package. A side view of the laser drilled cavities and packaged MEMS switches is shown below.

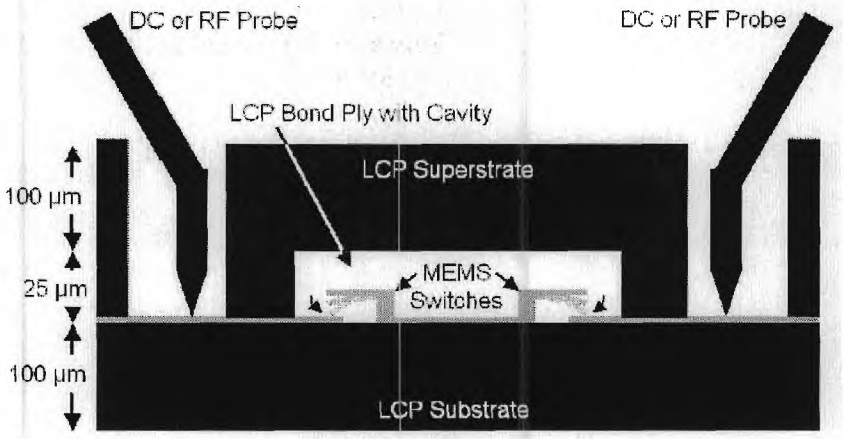

Fig. 66 Side view of packaged MEMS switches at tree-junction

In order to access the metal signal lines from outside the package with DC or RF probes, windows over the bias pads were laser etched in the middle and top layers to allow direct contact. The DC bias pads were connected to a voltage source through a high impedance DC probe. Since the DC probe is of much higher impedance than the signal lines, very little RF power is leaked into the DC probe. The placement of the windows and cavities is demonstrated below.

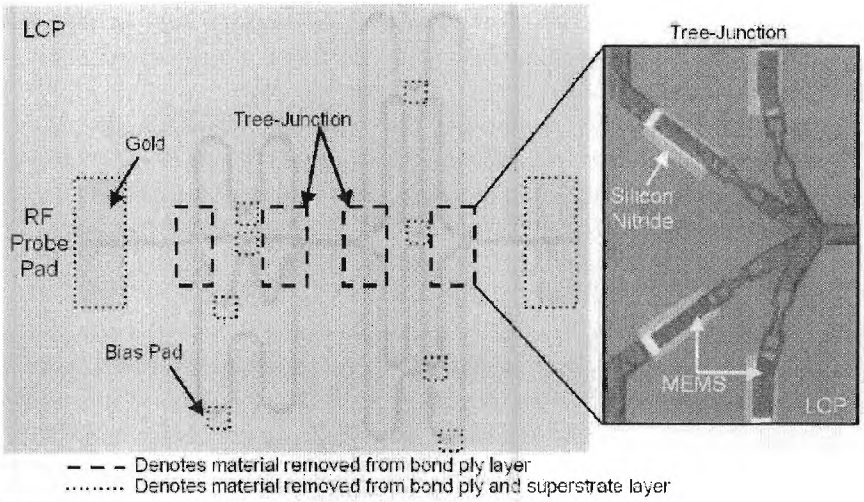

Fig. 67 Picture of fabricated MEMS phase shifter

After bonding with the packaging layers, the final device is achieved. An image of a completed phase shifter package is shown below.

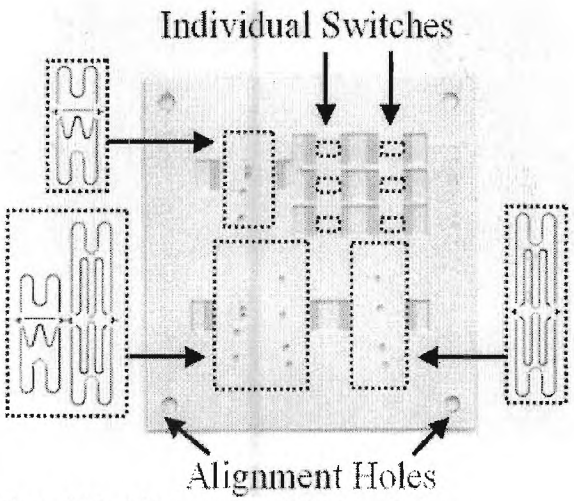

Fig. 68 Packaged 2-bit shifters, 4-bit shifter, and size MEMS switches

The measured loss for the packaged phase shifter is shown below.

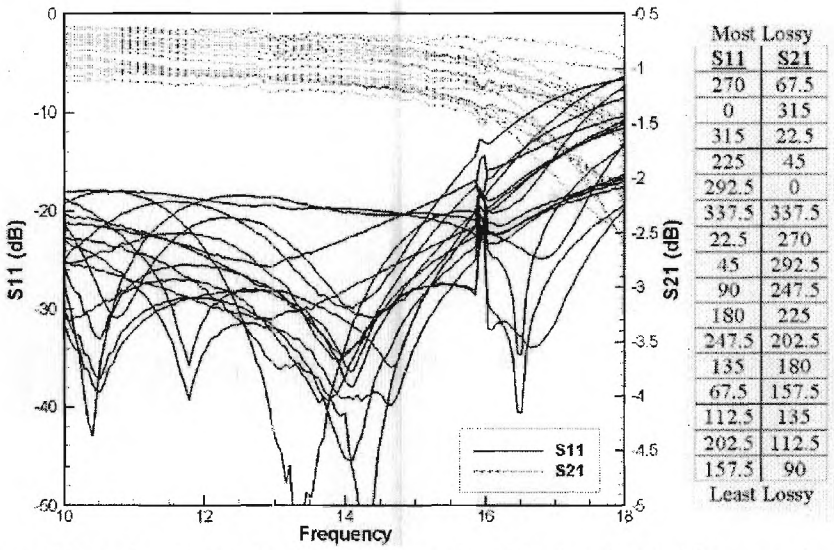

Fig. 69 Measured loss of packaged phase shifter. The order of the lines is listed from most lossy to least lossy at 14 GHz

The measured phase error is shown in the figure below.

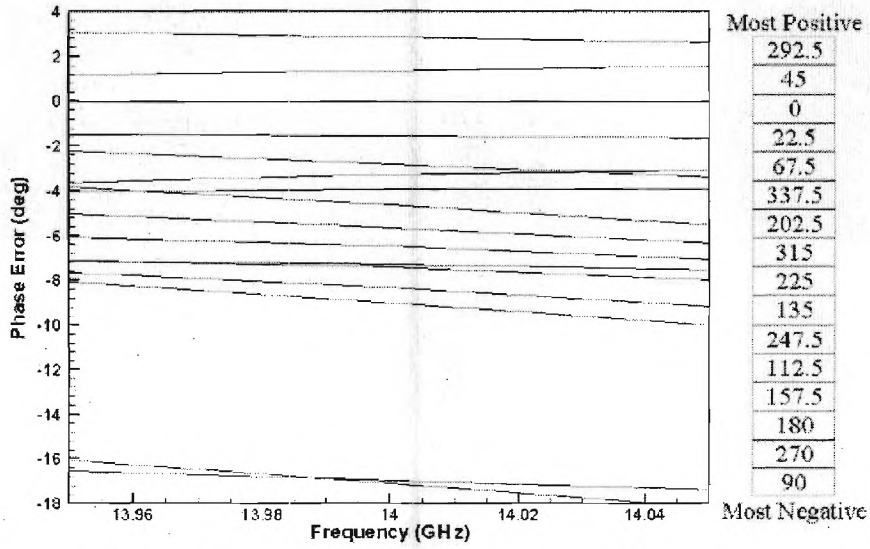

Fig. 70 Measured phase error of packaged phase shifter. The order of the lines is listed from most positive to most negative at 14 GHz

A comparison of the packaged and unpackaged measurement results are shown in the table below.

Table 10 - Measurements results for unpackaged and packaged configurations

	Worst Case	Average	Best Case
Unpackaged S11	-20.8 dB	-30.9 dB	-45.0 dB
Unpackaged S21	-1.22 dB	-0.95 dB	-0.66 dB
Packaged S11	-19.7 dB	-32.5 dB	-45.3 dB
Packaged S21	-1.21 dB	-0.96 dB	-0.69 dB
Unpackaged Phase Error	8.25°	3.96°	0.34°
Packaged Phase Error	17.07°	6.57°	1.38°
S21 Loss Variation	0.045 dB	0.013 dB	0.0022 dB
S21 Phase Variation	9.77°	3.16°	0.27°

D. Compact Soft/ Hard Surface (SHS) Structure

D.1 A Single Patch Surrounded by SHS

D.1.1 Configuration

In this section, we report on integrated Soft-Hard-Surface (SHS) structures that were investigated in this project to enhance the performance of planar antennas. SHS structures were selected instead of Electromagnetic Band Gap (EBG) structures due to their increased compactness. Figure 71 shows a patch antenna surrounded by a square SHS structure which consists of a metal-strip ring short-circuited to the ground plane by a metal wall along the outer edge of the ring. By adjusting the width of the metal strip (W_s) and the inner length of the SHS ring (L_s), the radiation pattern of the patch antenna can significantly improved. Fig. 72 compares the 3D radiation-patterns between the patch antennas with and without the SHS. It is seen that without the SHS the direction for the maximum radiation is no longer in the z-direction due to the contribution from the surface-wave diffraction. By introducing the SHS structure, the radiation pattern is significantly improved, including the enhanced radiation field in the z-direction, narrower beamwidth in the x-z plane, and reduced backside radiation. The 2D radiation patterns in two principal planes (E-plane and H-plane) are compared in Fig. 73. We can see that the directivity at broadside is increased by 4 dB while the backside radiation level gets reduced by about 8 dB.

An experimental verification was carried out by making use of the LTCC technology. Fig. 74 shows the layout and prototype of a patch antenna surrounded by the SHS. The simulated and measured results for the return loss are shown in Fig. 75 and good agreement is observed. The radiation patterns measured in the E- and H-planes are compared with simulated results in Fig. 76. We can see good agreement for the co-polarized components. It is confirmed that the radiation at broadside is enhanced and the backside level is reduced. Also the beamwidth in the E-plane is significantly reduced by the SHS. The simulated and measured gains at broadside (i.e. the z-direction) are shown in Fig. 77. We can see that the simulated broadside gain around the design frequency of the patch antenna with the SHS is more than 9.0 dBi, about 6.5 dB improvement as compared to the patch without the SHS. The maximum gain measured for the patch with the SHS is observed around 17 GHz and its value is near 9 dBi, almost 7 dB higher than the gain at broadside for the patch antenna without the SHS.

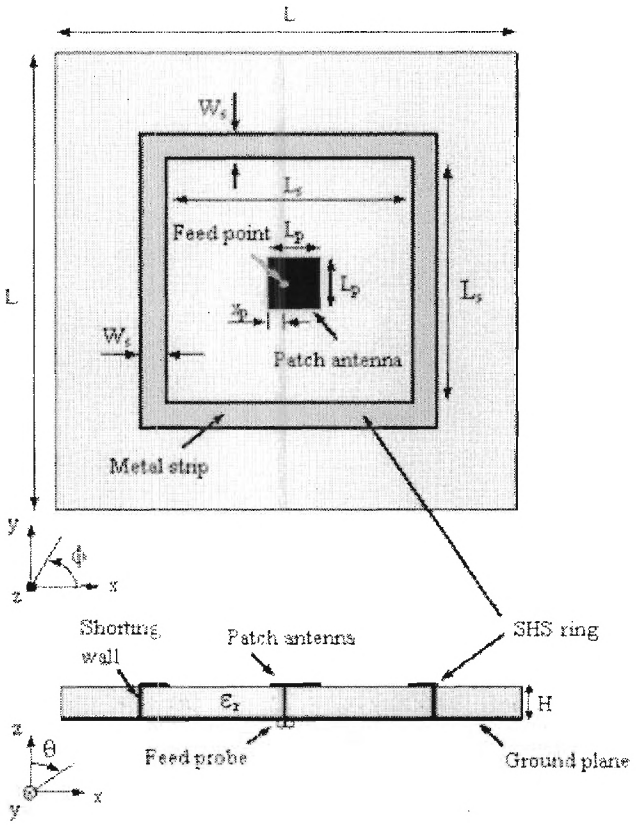

Fig. 71 Schematic Showing SHS configuration for a single patch antenna

D.1.2 Simulation Results

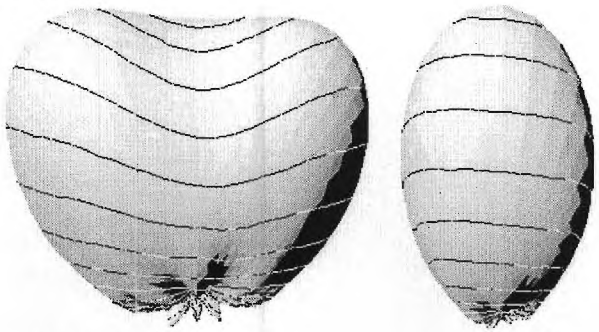

(a) Without SHS **(b) With SHS**

Fig. 72 3-D Radiation Pattern

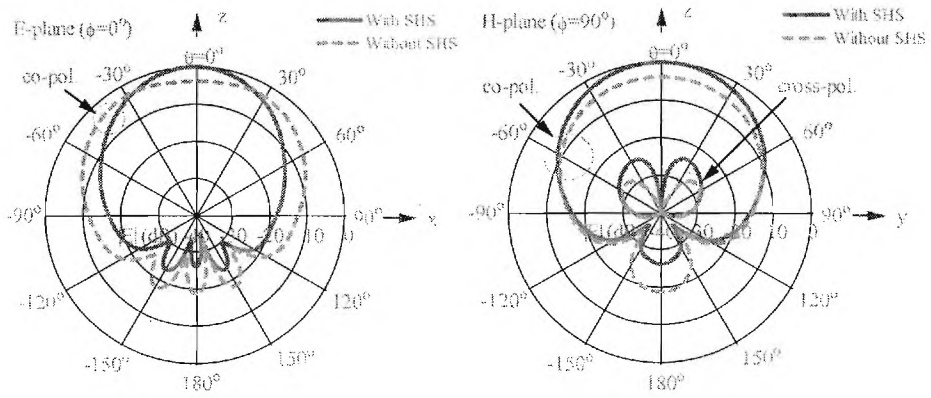

(a) Without SHS **(b) With SHS**

Fig. 73 2-D Radiation Pattern

D.1.2 Experimental Results

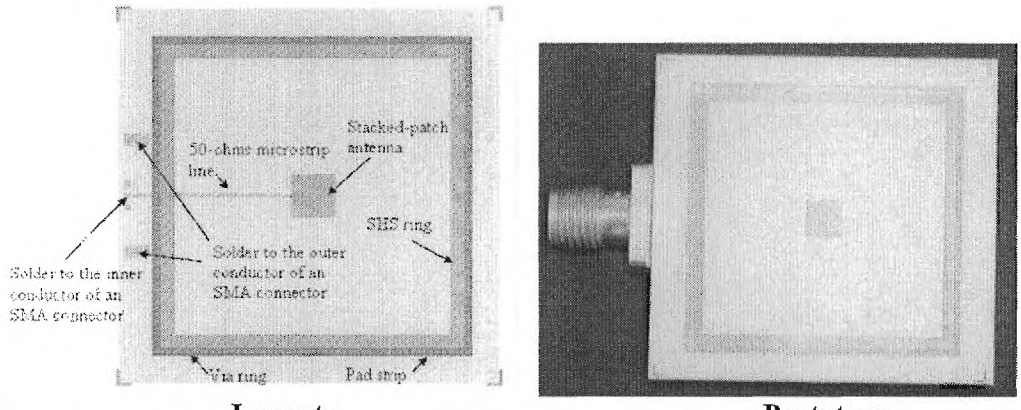

Layout **Prototype**

Fig. 74 Layout and fabricated photo of the patch antenna with SHS ring

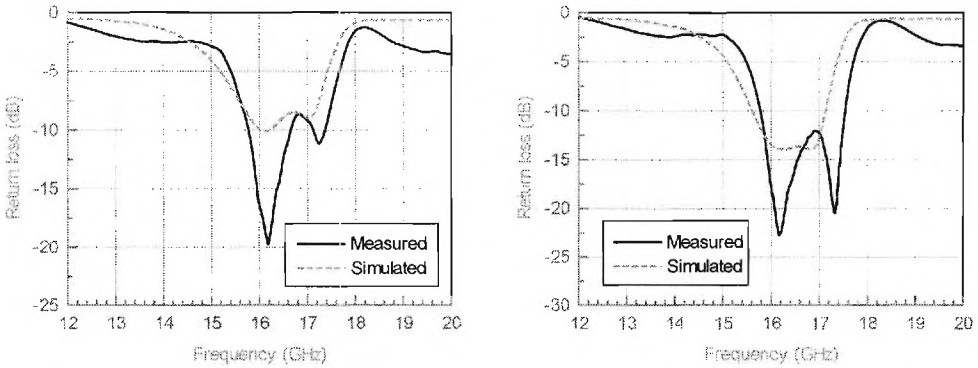

(a) Without SHS **(b) With SHS**

Fig. 75 Return Loss

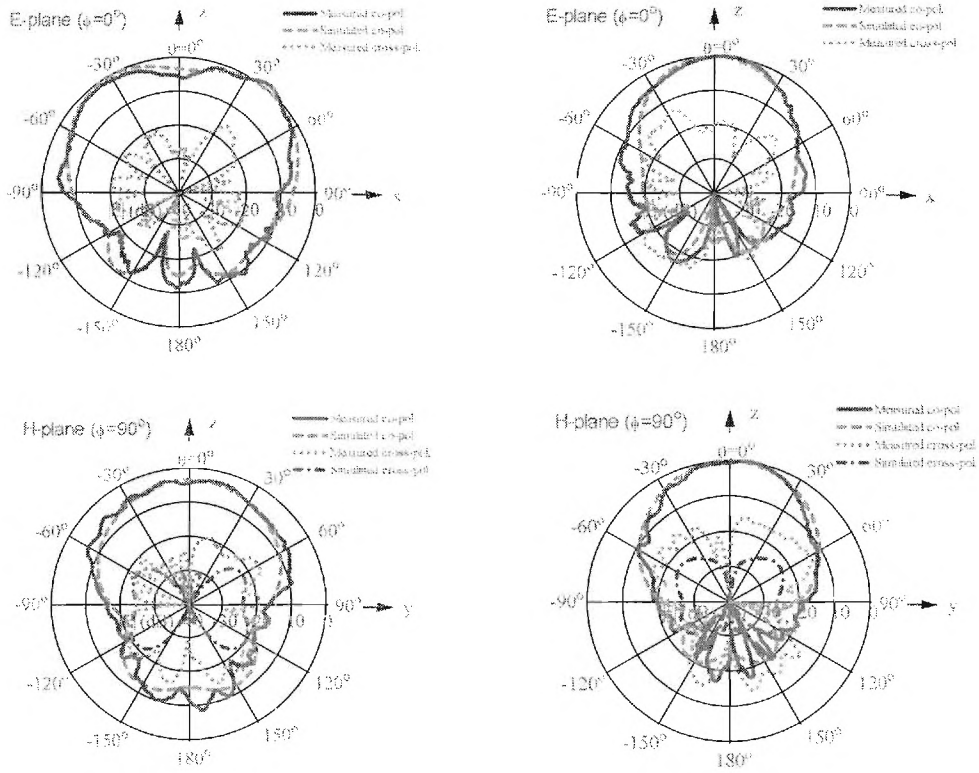

(a) Without SHS **(b) With SHS**

Fig. 76 Radiation Pattern

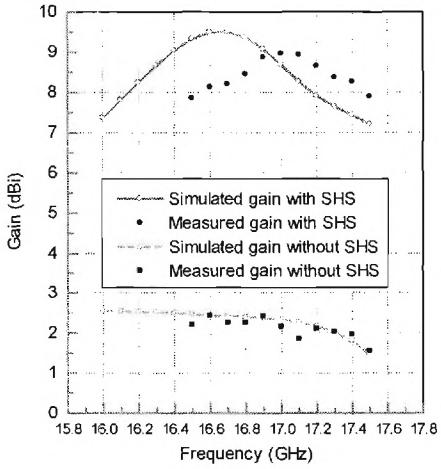

Fig. 77 Plot demonstrating gain enhancement with SHS

D.2 2X2 35 GHz Patch Array Surrounded by SHS

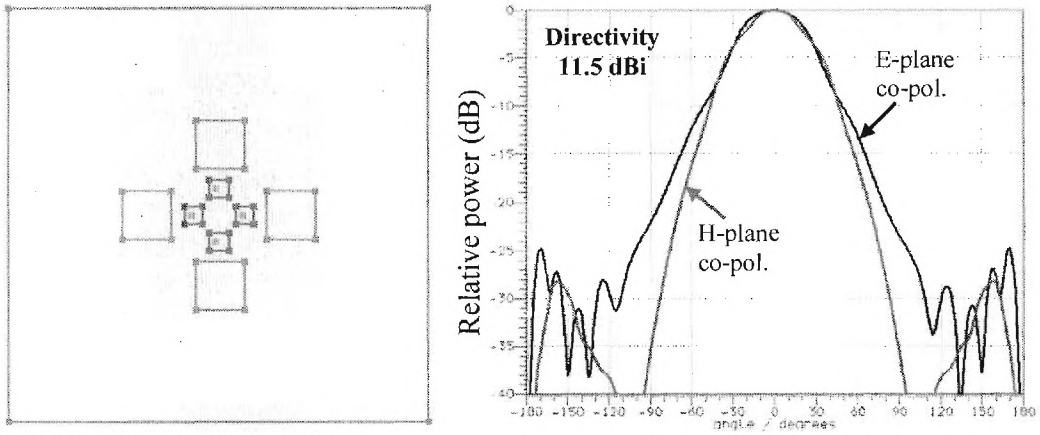

Fig. 78 2x2 35 GHz array without SHS

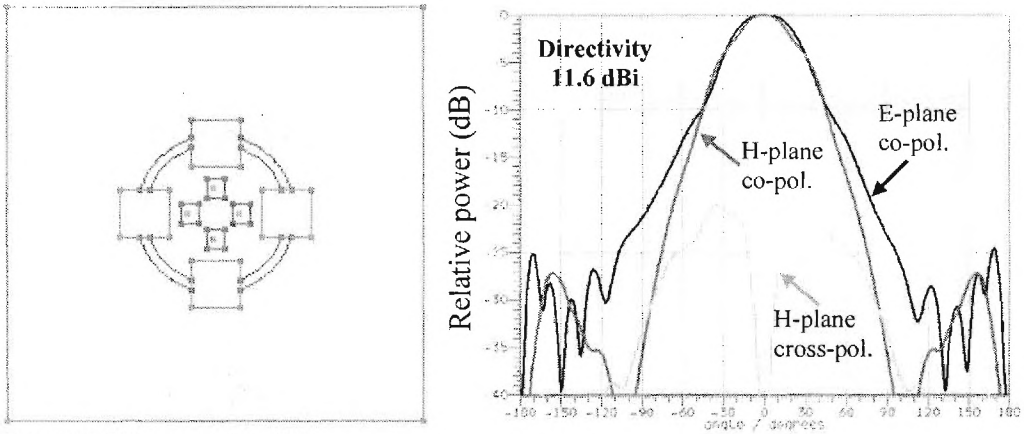

Fig. 79 2x2 35 GHz array with SHS

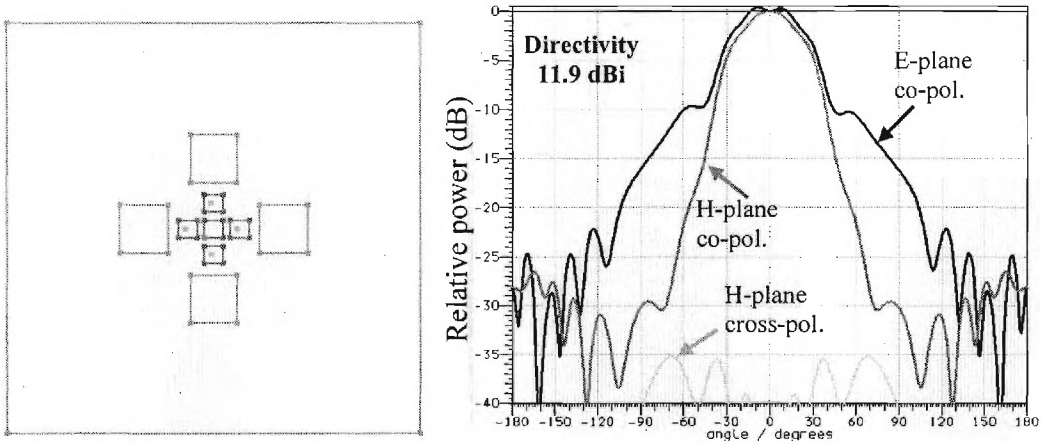

Fig. 80 2x2 35 GHz array with parasitic element

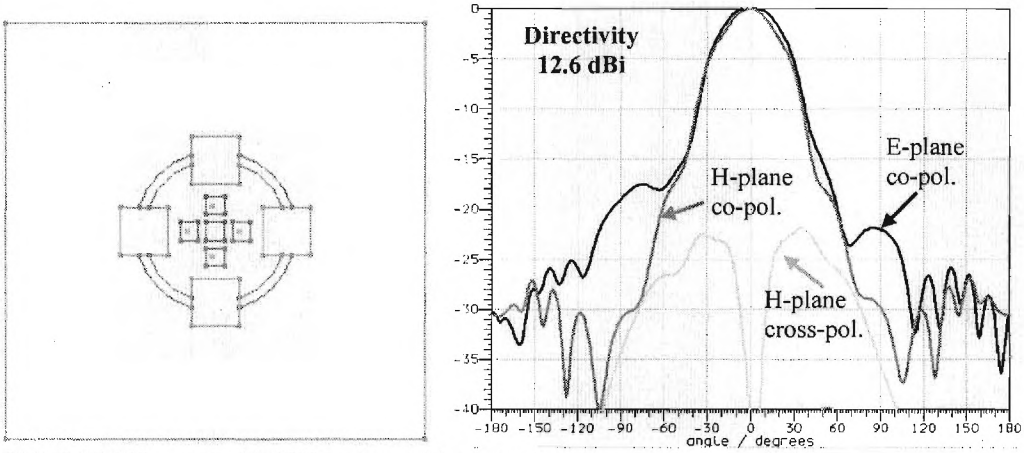

Fig. 81 2x2 35 GHz array with SHS and parasitic element

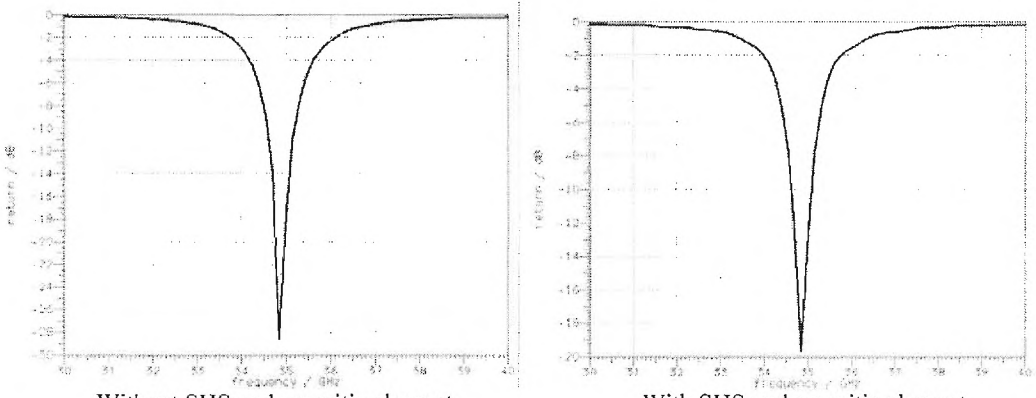

Without SHS and parasitic element | With SHS and parasitic element

Fig. 82 Effect of the SHS ring and the parasitic element on impedance matching

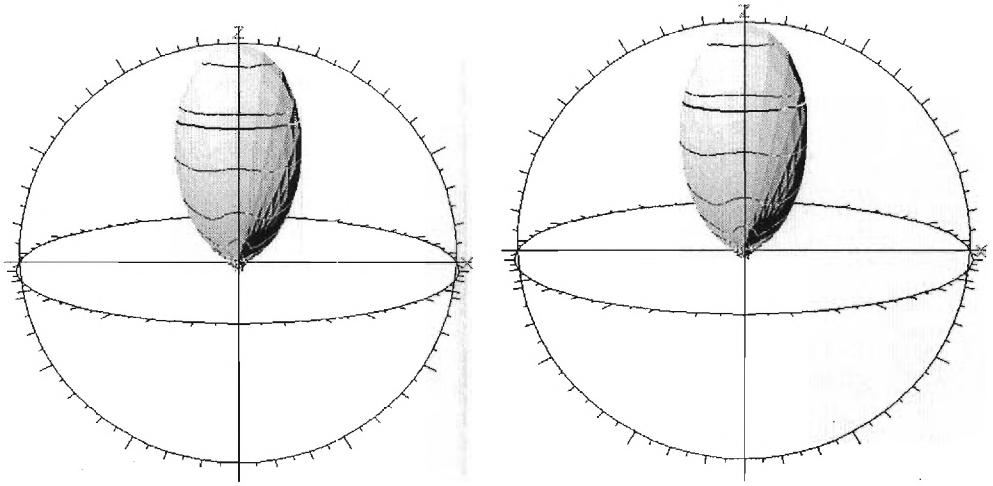

Without SHS and parasitic element (Directivity=12.6 dBi)

With SHS and parasitic element (Directivity=12.6 dBi)

Fig. 83 Effect of the SHS ring and the parasitic element on the radiation pattern of the 14 GHz array

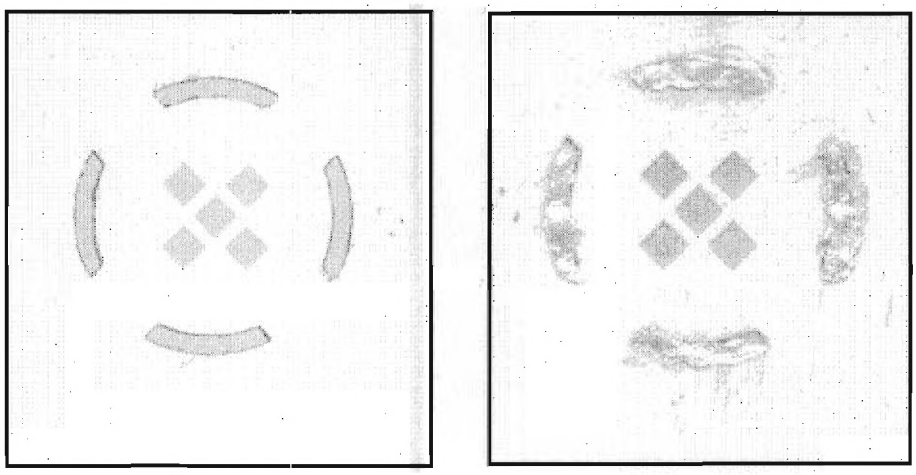

(a) Trench Unfilled

(b) Trench Filled

Fig. 84 Photo of the 35 GHz array with SHS ring

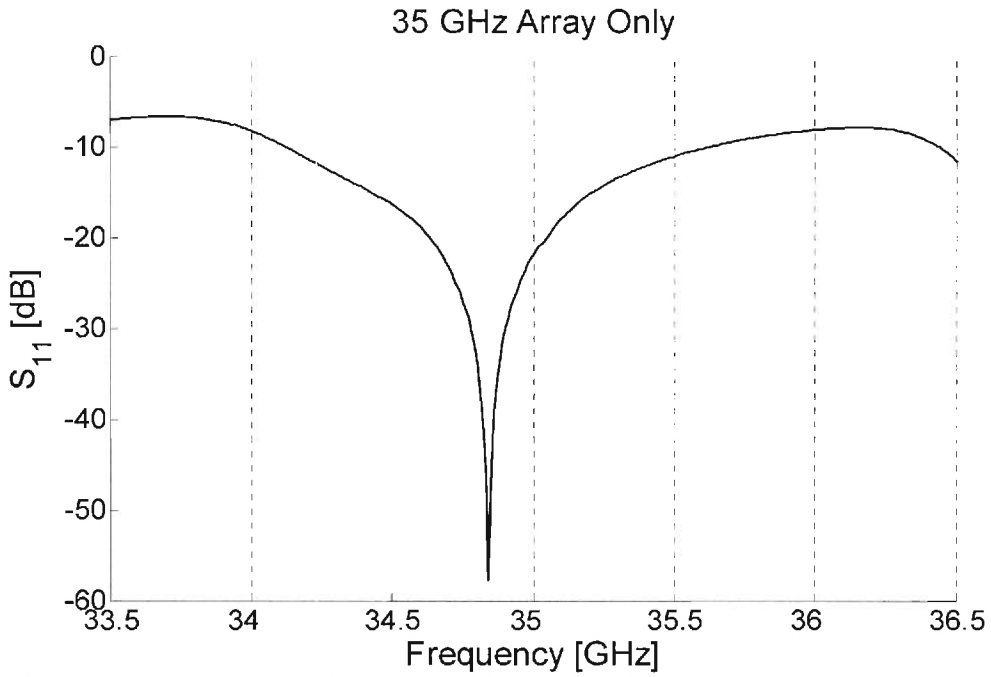

Fig. 85 Measured Return Loss (only 35 GHz Array)

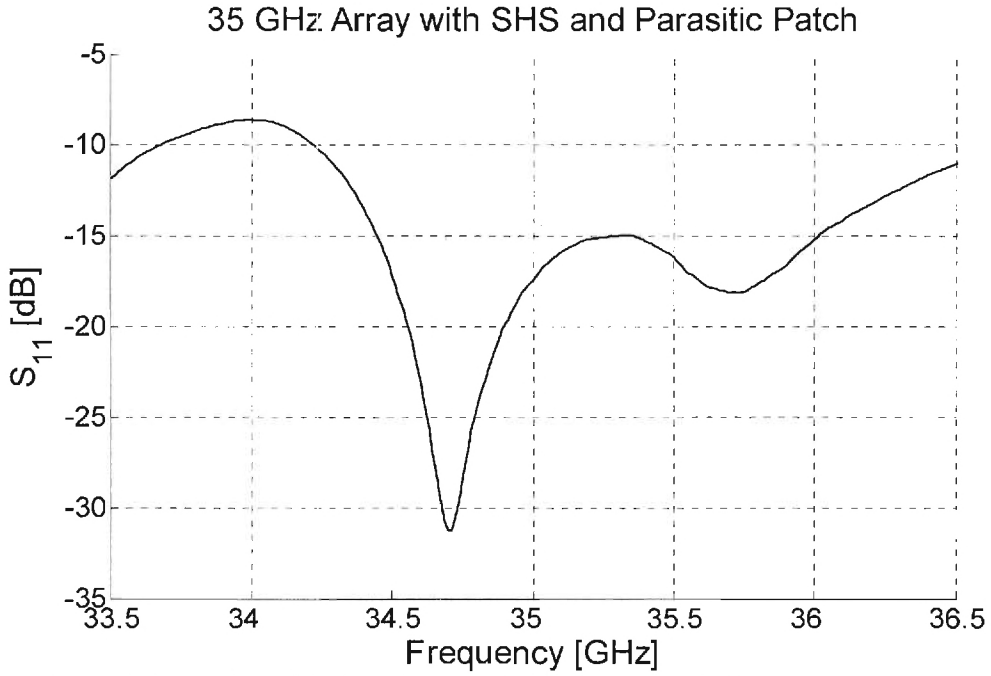

Fig. 86 Measured Return Loss (35 GHz Array with SHS and parasitic patch)

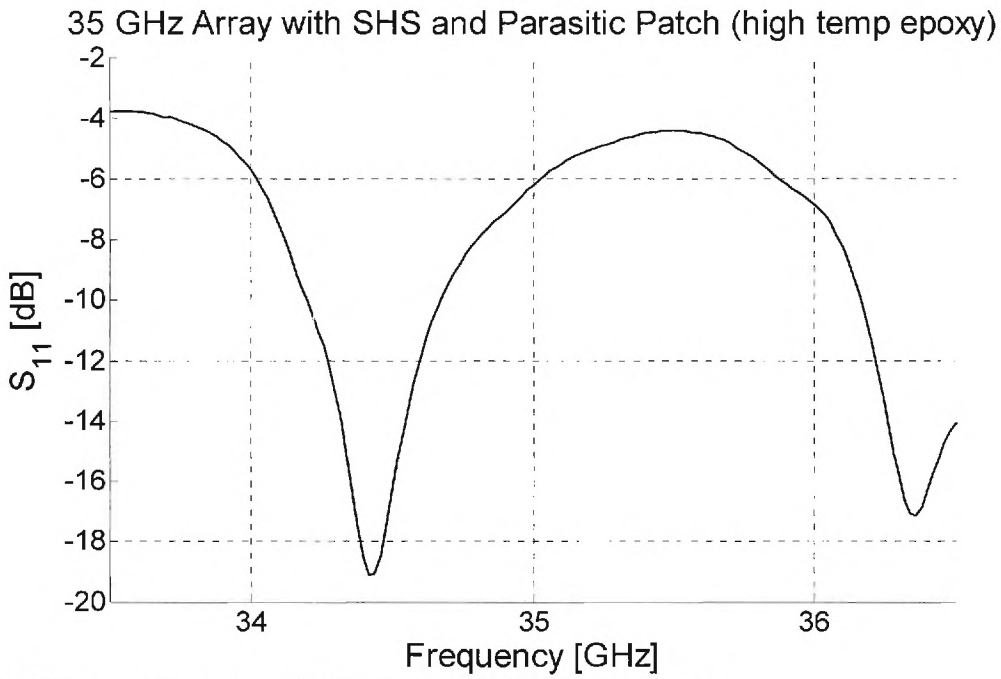

Fig. 87 Measured Return Loss (35 GHz Array with SHS and parasitic patch)

For each measurement, the LCP substrate with the antennas is mounted onto a plexiglass test fixture that is machined with a cutout, rectangular region both above and below the feed structure and antennas. In this way, the antenna is mounted on a pedestal in the antenna test chamber, but the pedestal does not interfere with the feed lines and the antennas are radiating into free space. However, the existence of the rectangular ring around the substrate does cause interference with the radiated signal, and this is evidenced by the small ripple on the radiation patterns. To excite the antenna arrays, a 2.4 mm coaxial to microstrip launcher is used.

It is found that the placement of the launcher affects the magnitude of the reflection coefficient, and therefore, it affects the magnitude of the measured radiated power. Therefore, multiple measurements were taken of each pattern, and the average value of the peak radiated power was determined. It is seen in the figures below that the average radiated power is approximately 5 dB high with the SHS structures.

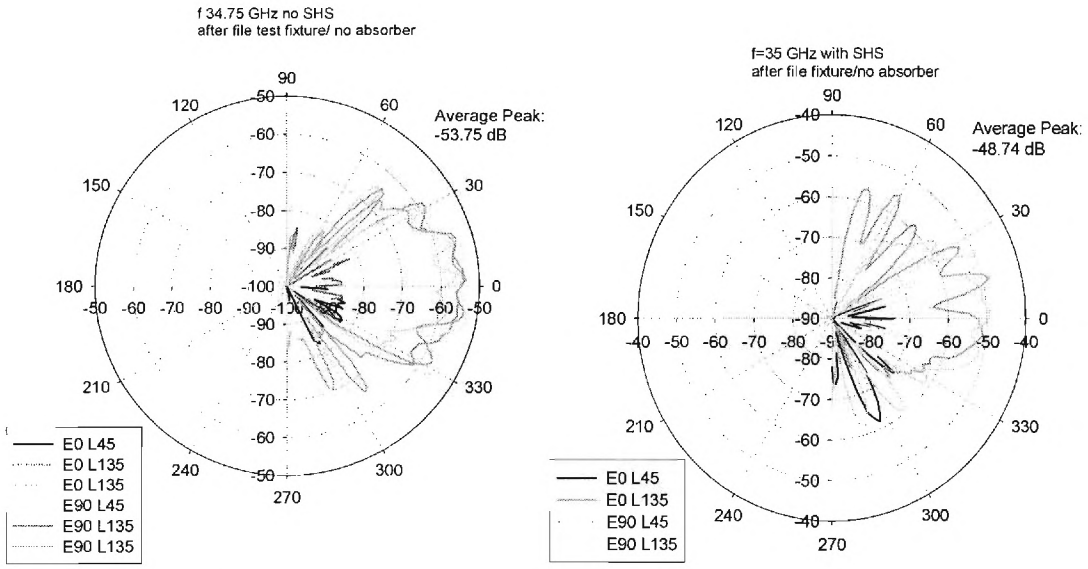

(a) Without SHS (b) With SHS

Fig. 88 Measured Radiation Patterns

The effectiveness of a modern SHS concept on the radiation-pattern improvement of a patch antenna on a large-size substrate has been investigated. The SHS ring can improve the gain of a 2×2 element array by about 1.1 dB via incorporating a parasitic element in the center of the array. The SHS ring and the parasitic element have no effect on the impedance matching and on the radiation pattern of the 14 GHz array. Therefore there is no need to revise the design for the feeding network. It is found that both the 14 GHz array and the 35 GHz array (when SHS is incorporated) have the same directivity (12.6 dBi)

E. Analysis of Phased Array

The purpose of this section is to examine the effects of beam steering when the antennas in the arrays are out of phase with one another. This is a critical step in the stage of developing the final 2x2 antenna arrays with RF MEMS switches and phase shifters. The 14 GHz and 35 GHz array configuration is shown in Fig. 89 without feedlines to simplify the study. A virtual coaxial probe was used to feed the antennas. The phase angles of interest for this analysis are 0°, 45°, 90°, 93°, 135°, and 180°.

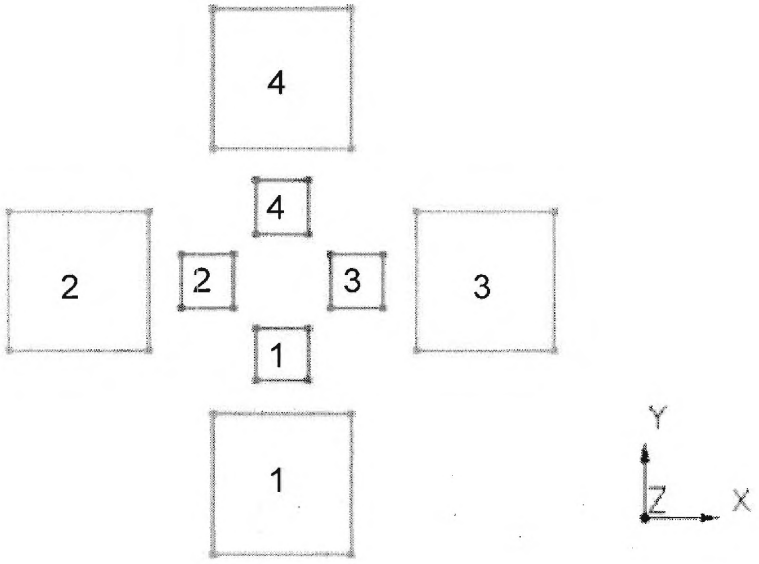

Fig. 89 Antenna structure (14 GHz in pink, 35 GHz in blue).

E.1 Results

Table 11 summarizes the results from the 14 GHz phase change simulations when the 35 GHz antennas act as parasitic elements. Furthermore, Table 12 gives the results from the 35 GHz phase change simulations when the 14 GHz antennas act as parasitic elements. The combination 1-2-3-4 describes the phase of the antenna that is being referenced. The E-plane and H-plane column headers give the angle of the tilted main beam. Directivity is given in dBi's. The results are given for six frequencies: Table 11 – 13.8, 14.0, 14.2 GHz, Table 12 – 34.8, 35.0, 35.2 GHz. All of the antennas simulated in this study are polarized in the x-direction.

Table 11

ant 1-2-3-4	θ main beam (deg)								
Phase Pattern	13.8 GHz			14.0 GHz			14.2 GHz		
	angle of tilt (θ)			angle of tilt (θ)			angle of tilt (θ)		
	E-plane	H-plane	Directivity	E-plane	H-plane	Directivity	E-plane	H-plane	Directivity
0-0-0-0	0.2	-0.4	12.241	0.1	-0.2	12.344	0	-0.2	12.444
45-0-0-0	0	-5.4	12.105	0	-5.3	12.241	0	-5.4	12.338
0-45-0-0	-8.6	-0.3	12.034	-8.7	-0.3	12.104	-8.7	-0.2	12.172
0-0-45-0	9.2	-0.6	12.007	8.9	-0.3	12.084	8.7	-0.2	12.156
0-0-0-45	0.4	4.9	12.108	0.2	4.9	12.252	0.1	5.2	12.356
90-0-0-0	-0.1	-9.6	11.508	0	-9.6	11.723	0	-9.9	11.819
0-90-0-0	-18.4	-0.3	11.619	-18.1	-0.4	11.602	-18.2	-0.3	11.594
0-0-90-0	18.8	-0.8	11.597	18.3	-0.4	11.583	18.2	-0.2	11.577
0-0-0-90	0.5	9.2	11.519	0.2	9.4	11.749	0.1	9.8	11.861
135-0-0-0	-0.1	-12.1	10.384	0	-12.6	10.691	0	-13.2	10.758
0-135-0-0	-27.2	-0.4	10.868	-27	-0.5	10.721	-27.1	-0.3	10.646
0-0-135-0	27.6	-0.8	10.854	27.1	-0.3	10.706	27.1	-0.2	10.631
0-0-0-135	0.4	12	10.395	0.2	12.6	10.723	0.1	13.2	10.814
180-0-0-0	0.1	21.6	9.506	0.1	20.7	9.365	0.1	21.5	9.316
0-180-0-0	-34.5	-0.8	9.692	-34.2	-0.6	9.395	-34.3	-0.3	9.377
0-0-180-0	34.7	-0.1	9.669	34.3	0	9.379	34.3	0	9.41
0-0-0-180	0.2	-22.9	9.437	0.1	-22	9.326	0	-22.5	9.293
90-90-0-0	-15.7	-12.2	11.905	-15.7	-12.1	11.992	-15.8	-12.3	12.037
0-0-90-90	16.3	11.4	11.913	16.1	11.5	11.986	16	11.8	12.02
0-90-90-0	0.1	-0.8	9.972	-0.1	-0.7	10.011	-0.1	-0.5	9.96
90-0-0-90	0.2	0	10.275	0.1	0	10.546	0.1	0	10.552
90-90-0-90	-15.2	0.1	11.547	-15.4	4.3	11.709	-15.6	0	11.752
90-90-90-0	-0.1	-12.7	11.685	-0.2	-12.2	11.735	-0.1	-12.3	11.777
93-0-0-0	0	-9.8	11.459	0	-9.9	11.68	0	-10.2	11.775
0-93-0-0	-19	-0.2	11.58	-18.8	-0.3	11.558	-18.8	-0.3	11.544
0-0-93-0	19.5	-0.8	11.556	18.9	-0.4	11.538	18.8	-0.2	11.527
0-0-0-93	0.5	9.4	11.469	0.2	9.6	11.708	0.1	10.1	11.82

Table 12

ant 1-2-3-4	θ main beam (deg)								
Phase Pattern	34.8 GHz			35.0 GHz			35.2 GHz		
	angle of tilt (θ)			angle of tilt (θ)			angle of tilt (θ)		
	E-plane	H-plane	Directivity	E-plane	H-plane	Directivity	E-plane	H-plane	Directivity
0-0-0-0	0	0	11.547	0	0	11.81	0	0	11.863
45-0-0-0	0.1	-9	12.017	0.1	-9.6	12.056	0.1	-9.9	12.112
0-45-0-0	-3	0	11.025	-2.9	0	11.101	-2.9	0	11.176
0-0-45-0	3	0	11.054	2.9	0	11.126	2.9	0	11.196
0-0-0-45	0.1	9.2	12.017	0.1	9.6	12.056	0.1	9.9	12.112
90-0-0-0	0.1	-14.1	12.126	0.1	-14.4	12.17	0.1	-14.7	12.212
0-90-0-0	-27.1	0	10.806	-27.1	0	10.85	-27.1	0	10.901
0-0-90-0	27.5	0	10.778	27.5	0	10.812	27.5	0	10.85
0-0-0-90	0.1	14.1	12.126	0.1	14.4	12.17	0.1	14.7	12.212
135-0-0-0	0.1	-17	11.521	0.1	-17.3	11.586	0.2	-17.6	11.636
0-135-0-0	-30.4	0	10.446	-30.1	0	10.516	-29.8	0	10.594
0-0-135-0	30.9	0	10.385	30.6	0	10.435	30.4	0	10.493
0-0-0-135	0.1	17	11.521	0.1	17.3	11.586	0.2	17.6	11.636
180-0-0-0	9.1	-19.1	9.759	9.4	-19.4	9.8	9.7	-19.7	9.809
0-180-0-0	-32.1	0	9.78	-31.6	0	9.784	-31.1	0	9.772
0-0-180-0	32.7	0	9.708	32.3	0	9.705	31.9	0	9.692
0-0-0-180	-9.1	19.1	9.759	-9.4	19.4	9.8	-9.7	19.7	9.809
90-90-0-0	-26	-13.9	11.686	-26.1	-14.1	11.724	-26.2	-14.3	11.755
0-0-90-90	26.4	14	11.594	26.6	14.3	11.621	26.7	14.6	11.642
0-90-90-0	-14	0	8.91	-13.9	0	8.801	-13.9	0	8.672
	14			14			14		
90-0-0-90	0.1	0.5	11.485	0.1	-1.4	11.423	0.2	-1.8	11.339
90-90-0-90	-26.7	0	11.197	-26.8	0	11.168	-26.8	0	11.127
90-90-90-0	-3	-14.1	10.667	-1.5	-14.4	10.673	-1.1	-14.6	10.725
93-0-0-0	0.1	-14.4	12.105	0.1	-14.7	12.147	0.1	-14.9	12.186
0-93-0-0	-27.4	0	10.815	-27.4	0	10.861	-27.4	0	10.914
0-0-93-0	27.8	0	10.786	27.8	0	10.821	27.8	0	10.861
0-0-0-93	0.1	14.4	12.105	0.1	14.7	12.147	0.1	14.9	12.186

E.2 Individual elements out of phase

In the first series of simulations, one of the elements is placed out of phase for each of the four antennas at each frequency. The phase angles that were studied are 45°, 90°, 135°, and 180°. Tables 11 and 12 show that the main beam experiences a tilt in the direction of the antenna that is out of phase. As the phase is increased, the tilt angle increases. For the 14 GHz antennas, the tilt angle increase follows a linear relationship. For the E-plane of antennas 2 and 3, the tilt starts at about 9° for a 45° phase difference and rises to about 18.5° for a 90° phase difference, 27.5 for a 135° phase difference, and finally 34.5° for a 180° phase difference. For the 35 GHz antennas, the E-plane tilt angle experiences a small increase (3°) from 0° to 45° phase angle change, but rises quickly to around 27° when the phase angle is increased to 90°. This is a large jump that is not seen in the 14 GHz excitations. The H-plane experiences results that are not as linear as those of the E-plane. At a phase angle of 45°, the H-plane main beam tilt jumps from 0° to around 9°. As the phase angle rises from 45° to 90°, the H-plane beam has a smaller tilt of approximately 14°. That is a 5° change from 45° to 90° in comparison to the 9° change from 0° to 45°. As the phase angles increases from 90° to 135° and from 135° to 180°, the changes in the angle of beam tilt decreases by smaller increments (3° and 2°, respectively). From there, the tilt angle saturates to a steady value around a 180° phase difference. It is also interesting to note that antennas 2 and 3 have tilt angles that are as much as twice the value of antennas 1 and 4. The linearly-polarized excitations contribute to this difference. The directivity increases as the phase difference increases. When all antennas are in phase, a directivity greater than 12 dBi can be achieved. Fig. 87 shows the 3D radiation pattern at 14 GHz for the excitation of antenna 2 at four different phase angles. As the phase is increased, the directivity drops to under 10dBi where the main beam is split into two beams of similar directivity. The 180° phase difference radiation patterns show severe pattern degradation for the 35 GHz antennas but the comparison to Fig. 90 is similar.

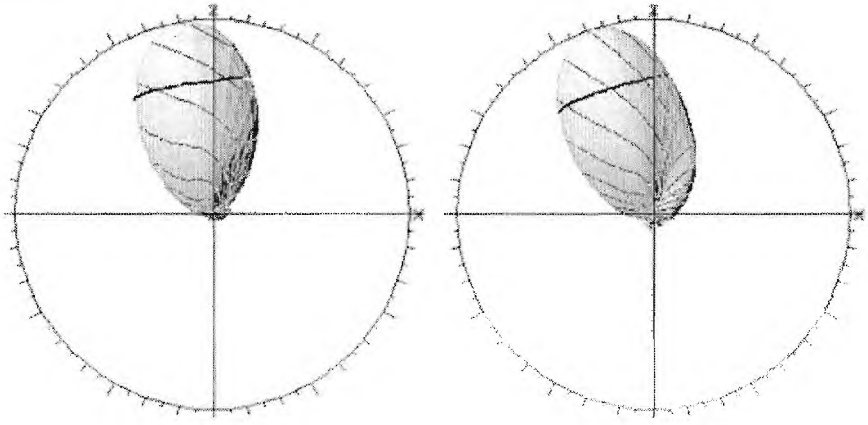

a. b.

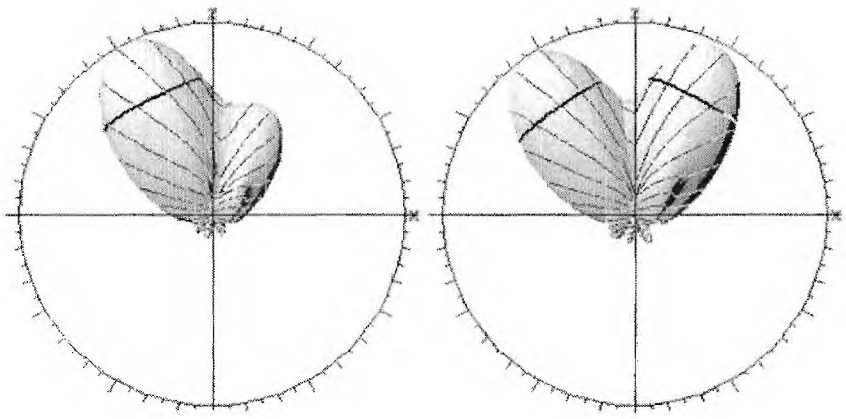

c. d.

Fig. 90 3D radiation pattern patterns at 14 GHz for phase combinations, a.) 0-45-0-0, b.) 0-90-0-0, c.) 0-135-0-0, and d.) 0-180-0-0

E.3 Two elements out of phase

The next series of simulations focused on the effects of the radiation pattern as two antennas were placed out of phase. For this study, there are 4 combinations that were placed out of phase (90° phase difference). An interesting result occurs from these simulations. When antennas 1 and 2 (90-90-0-0) and antennas 3 and 4 (0-0-90-90) are set at 90° phase difference, the E-plane and H-plane experiences a beam tilt. In the 14 GHz excitations, the angles of the main beam tilts are close in value (separated by less than 5°). When the 35 GHz antennas are excited, the beam tilt difference between the E-plane and the H-plane is around 13°. This is shown in Fig. 91. It is understandable that the higher frequency designs will have greater effects in the beam tilt. This could be attributed to multiple effects of the phase difference between elements and the possible edge diffraction effects that occurs on finite substrate with the size is electrically large. Conversely, when antennas 2 and 3 and antennas 1 and 4 are set at 90° phase difference, the main beam experiences no tilt at all. This can be explained by the concept of arrays and array factors. Antennas 1 and 4 form an array in the y-direction, while antennas 2 and 3 form an array in the x-direction. Therefore, antennas 1 and 4 have no affect on the beam steering characteristics of antennas 2 and 3. So when antennas 1 and 2 are set at a 90° phase difference, there are two linear arrays (1-4 and 2-3) that are out of phase; hence, beam tilts occur in both planes. (Same applies for antennas 3 and 4 set at 90° phase difference.) Moreover, when antennas 1 and 4 are set at a 90° phase difference (90-0-0-90), the antennas in both linear arrays are in phase and no beam tilt is seen. This is also observed in the excitation of antennas 2 and 3 with a 90 phase angle. Keep in mind that the polarization direction has no effect on this concept (it doesn't matter if the antennas are polarized in the x- or y- direction). This observation is clearly seen when the 14 GHz antennas are excited. When antennas 2 and 3 are excited at 35 GHz, the main beam is split into two beams that tilt by 14° in opposite directions. This split is shown in the E-plane radiation patterns of Fig. 92. The reason for this split is being investigated. The existence of grating are present as well in Fig. 92. The grating lobes have a larger

amplitude at the higher frequency (35 GHz). The directivities of the 14 GHz excitations are slightly less than 12 dBi for the 1-2 and 3-4 excitation combinations. For the 1-4 and 2-3 combinations at 14 GHz, the directivities are around 10 dBi; at 35 GHz, the 2-3 combination has a lower directivity due to the beam split. The 1-4 combination has a directivity of 12 dBi due to the element distance of the patches in phase.

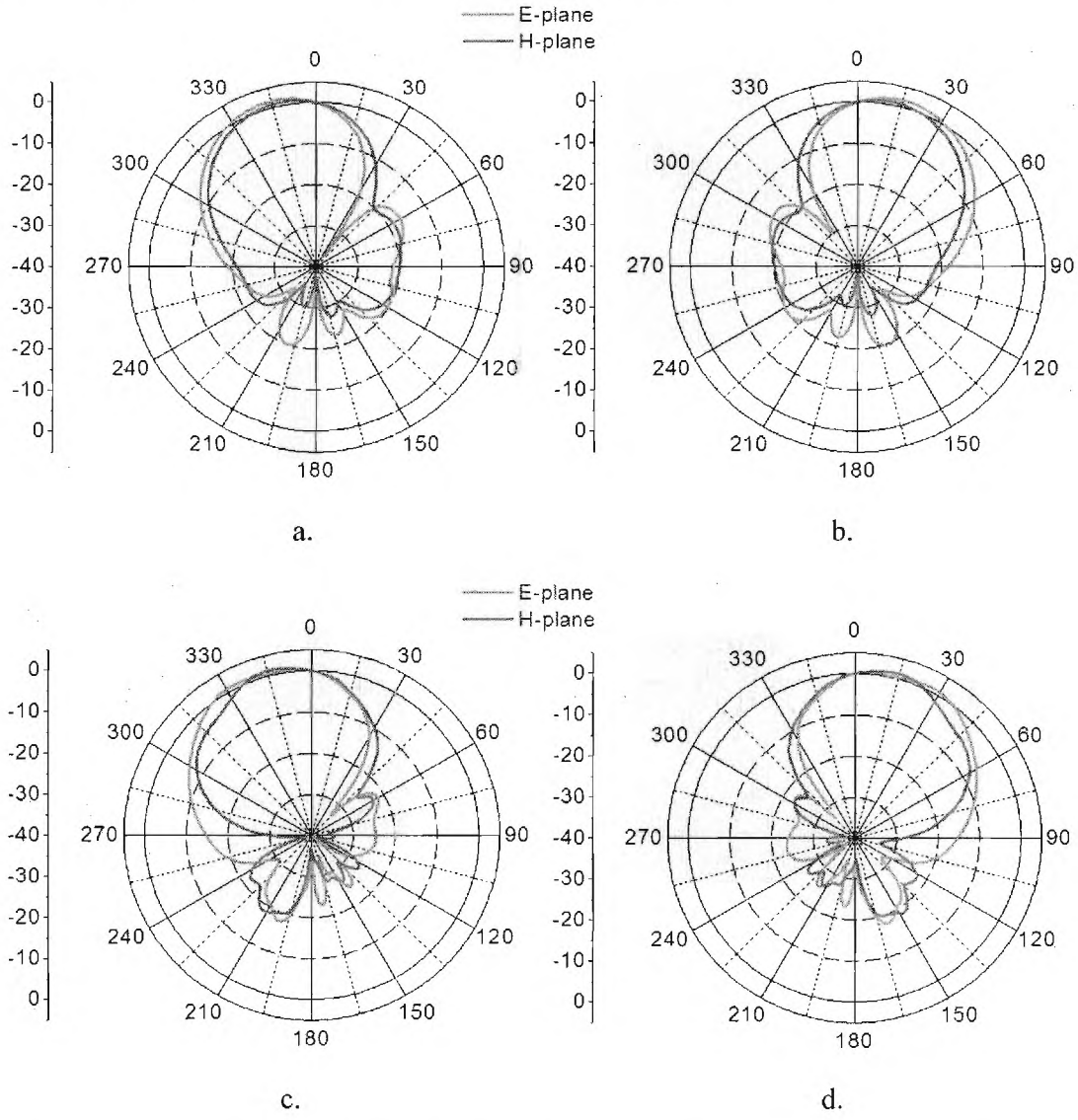

Fig. 91 2D radiation patterns of phase combinations a.) 90-90-0-0 and b.) 0-0-90-90 at 14 GHz and c.) 90-90-0-0 and d.) 0-0-90-90 at 35 GHz.

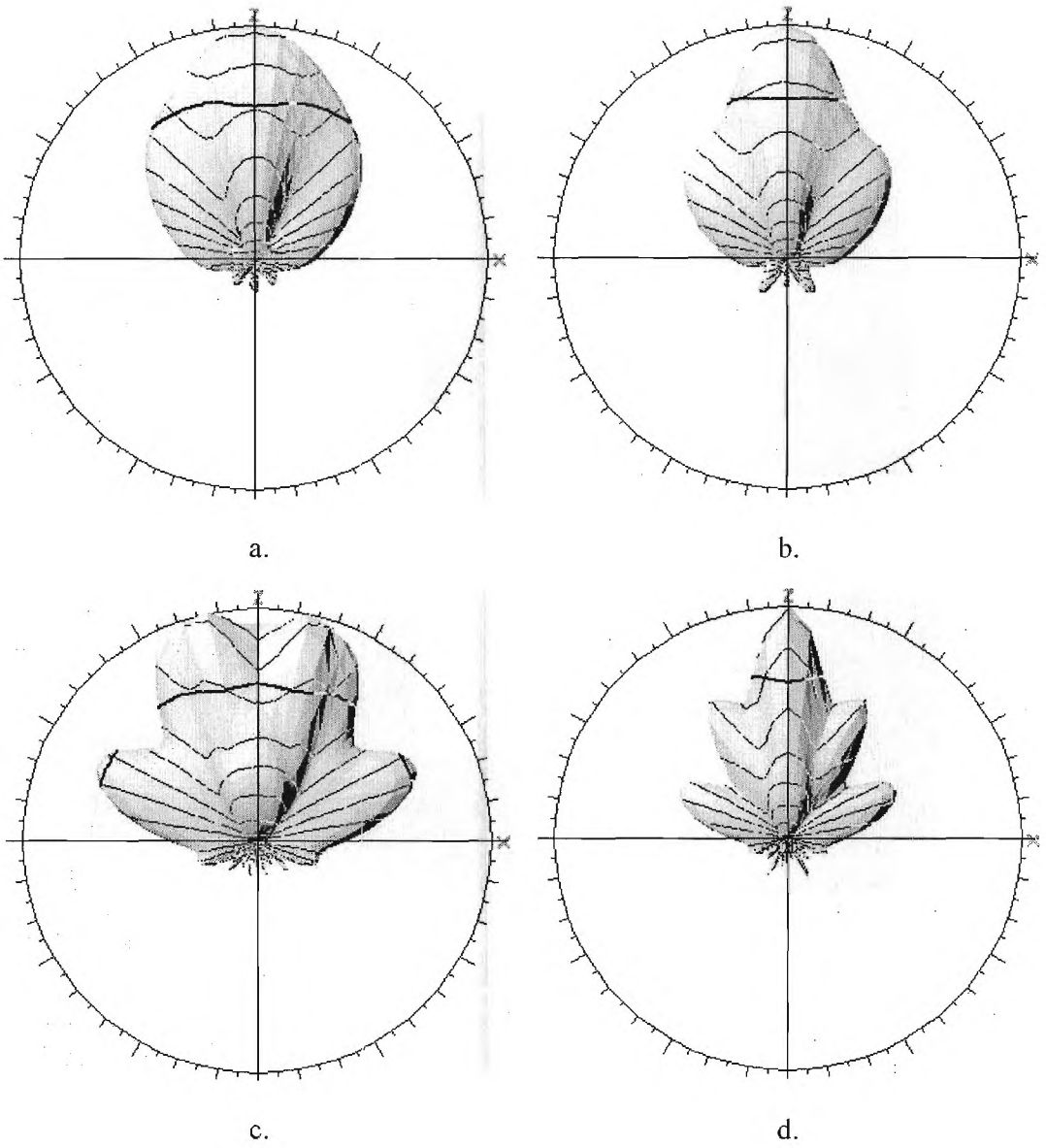

Fig.92 3D radiation patterns of phase combinations a.) 0-90-90-0 and b.) 90-0-0-90 at 14 GHz and c.) 0-90-90-0 and d.) 90-0-0-90 at 35 GHz.

E.4 Three elements out of phase

In the next series of simulations, three elements are placed out of phase. Only two combinations were done for this test: antennas 1, 2, and 3 (90-90-90-0) and antennas 1, 2, and 4 (90-90-0-90). For the first test (90-90-90-0), a 15° beam tilt is seen in the E-plane, while for the second test (90-90-0-90), a 12° beam tilt can be observed in the H-plane radiation pattern at 14 GHz. This is a difference of only 3°. Following the same array concept discussed in the last section, the beam tilts can be attributed to the smaller linear array being out of phase. In the first test, antennas 1 and 4 are out of phase so a

beam tilt occurs in the H-plane (y-direction). Similarly, antennas 2 and 3 are out of phase in the second test, and therefore, a beam tilt occurs in the E-plane (x-direction). At 35 GHz, the beam tilt in the E-plane is around 27° for the 1-2-4 combination of 90° phase angles. In the H-plane, the beam tilt is about 14° for the 1-2-3 combination of 90° phase angles. The large disparity in the beam tilt angles of the E-plane patterns at 14 and 35 GHz is displayed in Fig. 93. It may be difficult to see that the main has split into two beams, but the split is quite small. The H-plane patterns show little change in the beam tilt angles at the two frequencies (14 and 35 GHz). Without this split, the E-plane radiation patterns would experience a similar characteristic to the H-plane radiation patterns. The directivities at 35 GHz for the two combinations are smaller (between 10.6-11.1 dBi) than those at 14 GHz for the two combinations (11.5-11.7 dBi).

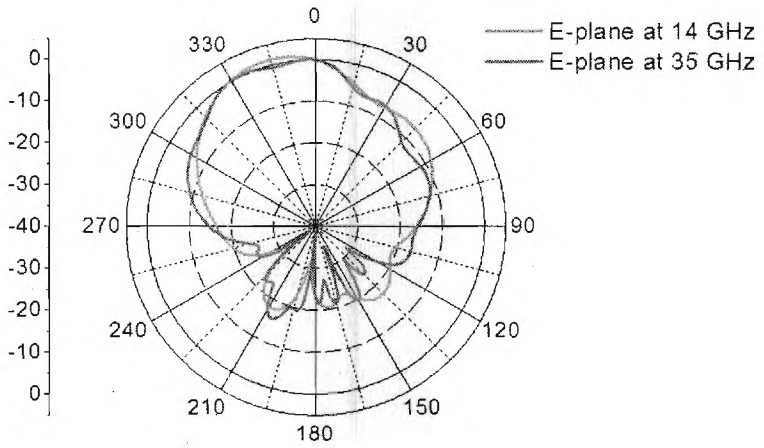

(a)

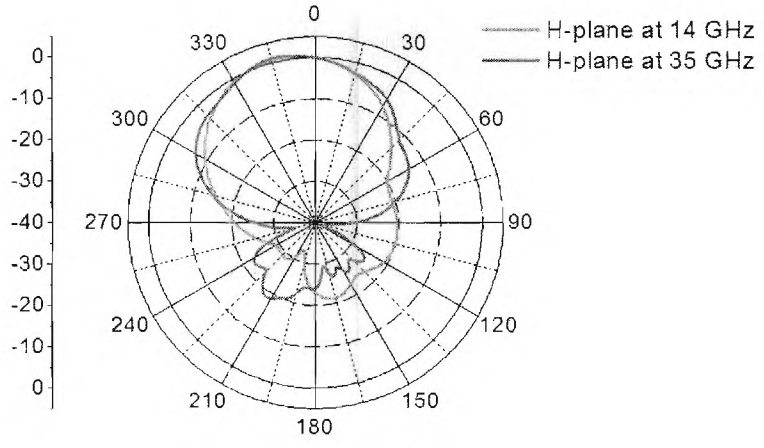

(b)

Fig. 93. 2D radiation patterns of a.) E-plane comparison at 14 and 35 GHz and b.) H-plane comparison at 14 and 35 GHz.

E.5 Comparison between individual elements that have 90° and 93° phase differences

In this last test, four simulations at 14 GHz and 35 GHz were performed to test the effects of having a slight phase difference in the excitations. From the tables shown in this report, the values of the directivity and the beam tilt angle are similar for both phase difference angles. The discrepancies in the beam tilt angles are less than 1°, and the 93° phase difference angles exhibit directivities than are 0.5 dBi less than the 90° phase difference angles.

F. TRL Assessment

During the duration of this project we have developed a 2x2 dual frequency/polarization sub-array operating at 14/35 GHz utilizing RF MEMS switches on a multilayer LCP substrate and have demonstrated its validity in a laboratory environment. We have also developed a packaged 4-bit RF MEMS phase shifter on a multilayer LCP substrate and have also demonstrated its validity in a laboratory environment. **As a result, we have reached a TRL of 4 for these components**. The entry point for this project was a TRL of 2.

In order to achieve a TRL of 6 for a lightweight, multilayer RF MEMS based 2x2 sub-array integrated with a 4-bit phase shifter, the PI estimates the duration of the follow-on activities to 3-4 years with a rough cost of $1.2M-$1.4M.

Georgia Institute of Technology

Lightweight, Deployable, Dual-Frequency/Polarization Microstrip Antenna Array for Remote Sensing of Precipitation

ESTO
Earth Science Technology Office

PI: Prof. John Papapolymerou/Georgia Tech

Objectives

- Contribute to the development and demonstration of concepts and techniques that enable lightweight, deployable and low cost antenna arrays for remote sensing:
  - Develop and demonstrate a 2x2 dual frequency/polarization microstrip array system on-a-package (SOP) in a 3D configuration
  - Develop and demonstrate RF MEMS switches and 4-bit phase shifters for SOPs
  - Develop and demonstrate 3D integrated modules in flexible laminated materials.

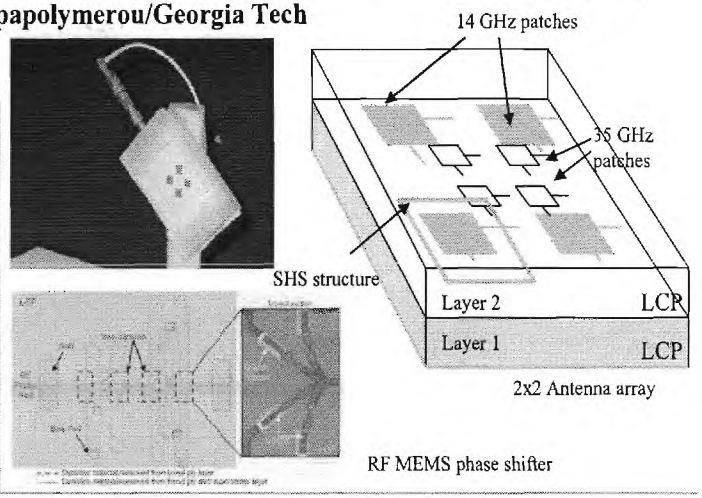

Accomplishments

- Demonstrated the excellent electrical and packaging performance of LCP organic materials up to 110 GHz
- Developed 2x2 dual frequency/polarization array (14/35 GHz) on lightweight, flexible, multilayer LCP substrates with RF MEMS switches
- Developed a packaged 4-bit low loss RF MEMS phase shifter on LCP organic substrate
- Developed integrated SHS antenna structures for increased efficiency
- Some "so whats":
  - Proved feasibility of making flexible, lightweight arrays on organic substrates up to mm-wave range
  - LCP offers excellent antenna performance (75-80% efficiency) & packaging characteristics up to mm-wave range
  - First organic RF MEMS phase shifter with 0.25 dB/bit loss at 14 GHz

CoIs: Prof. Manos M. Tentzeris (Georgia Tech), Dr. George Ponchak (NASA Glenn)

TRL_{in}=2; TRL_{out}=4

March 2006

Appendix

Publications

Journal publications

[1] R.L. Li, G. DeJean, E.M. Tentzeris, J. Papapolymerou and J. Laskar, "FDTD Analysis of Patch Antennas on High Dielectric-Constant Substrates Surrounded by a Soft-and-Hard Surface," *IEEE Transactions on Magnetics,* Vol. 40, No. 2, pp. 1444-1447, March 2004.

[2] D. Thompson, O. Tantot, H. Jallageas, G. Ponchak, M. Tentzeris and J. Papapolymerou, "Characterization of Liquid Crystal Polymer (LCP) Material and Transmission Lines on LCP Substrates From 30-110 GHz," *IEEE Transactions on Microwave Theory and Techniques,* Vol. 52, No. 4, pp. 1343-1352, April 2004

[3] M. Tentzeris, J. Laskar, J. Papapolymerou, S. Pinel, V. Palazzari, R. Li, G. DeJean, N. Papageorgiou, D. Thompson, R. Bairavasubramanian, S. Sarkar and J.H. Lee, "3D Integrated RF and Millimeter-Wave Functions and Module System-On-Package Technology," *IEEE Transactions on Advanced Packaging,* Vol. 27, No. 2, pp. 332-340, May 2004

[4] R.L. Li, G. DeJean, M. Tentzeris, J. Papapolymerou and J. Laskar, "Radiation Pattern Improvement of Patch Antennas on a Large-Size Substrate Using a Compact Soft/Hard Surface (SHS) Structure and its Realization on LTCC Multilayer Technology," *IEEE Transactions on Antennas and Propagation,* Vol. 53, No. 1, pp. 200-208, January 2005

[5] R.L. Li, D. Thompson, M. Tentzeris, J. Laskar and J. Papapolymerou, "Development of a Wideband Short Backfire Antenna Excited by an Unbalance-Fed H-Shaped Slot," *IEEE Transactions on Antennas and Propagation*, Vol. 53, No.2, pp. 662-671, February 2005

[6] G. DeJean, R. Bairavasubramanian, D. Thompson, G.E. Ponchak, M. Tentzeris and J. Papapolymerou, "Liquid Crystal Polymer (LCP): A New Organic Material for the Development of Multilayer Dual Frequency/Dual Polarization Flexible Antenna Arrays," *IEEE Antennas and Wireless Propagation Letters,* Vol. 4, pp. 22-26, March 2005.

[7] S. Pinel, R. Bairavasubramanian, J. Laskar and J. Papapolymerou, "Compact Planar and Via-Less Composite Low-Pass Filter Using Folded Stepped Impedance Resonator on Liquid Crystal Polymer Substrate," *IEEE Transactions on Microwave Theory and Techniques*, Vol. 53, No. 5, pp. 1707-1712, May 2005

[8] J.H. Lee, G.R. DeJean, S. Sarkar, S. Pinel, K. Lim, J. Papapolymerou, J. Laskar and M. Tentzeris, "Highly Integrated Millimeter-Wave Architectures Using 3-D LTCC System-on-Package (SOP) Technology," *IEEE Transactions on Microwave Theory and Techniques,* Vol. 53, No. 6, pp. 2220-2229, June 2005.

[9] R. Li, D. Thompson, J. Papapolymerou, J. Laskar and M. Tentzeris, "A New Excitation Technique For Wide-Band Short Backfire Antennas," *IEEE Transactions on Antennas and Propagation*, Vol. 33, No. 7, pp. 2313-2320, July 2005.

[10] I.K. Kim, N. Kingsley, M. Morton, R. Bairavasubramanian, J. Papapolymerou, M. Tentzeris and J.G. Yook, "Fractal Shaped Microstrip Coupled Line Bandpass Filters For Suppression of 2nd Harmonic," *IEEE Transactions on Microwave Theory and Techniques,* Vol. 53, No. 9, pp. 2943-2948, September 2005.

[11] D. Thompson, J. Papapolymerou and M. Tentzeris, "High Temperature Dielectric Stability of Liquid Crystal Polymer at mm-Wave Frequencies," *IEEE Microwave and Wireless Components Letters,* Vol. 15, No. 9, pp. 561-563, September 2005.

[12] J.H. Lee, L. Marcaccioli, G. Dejean, C. Lugo, S. Pinel, J. Papapolymerou, J. Laskar, R. Sorrentino and M. Tentzeris, "Advanced System-on-Package (SOP) Front-End Passive Solutions For RF and Millimeter-Wave Wireless Systems," *Proceedings of the European Microwave Association,* Vol. 1, No. 2, pp. 130-139, June 2005.

[13] N. Kingsley, G. Wang and J. Papapolymerou, "Comparative Study of Analytical and Simulated Doubly-Supported RF MEMS Switches for Mechanical and Electrical Performance," *Applied Computational Electromagnetics Society Journal,* Vol. 21, No. 1, pp. 9-15, March 2006.

[14] N. Kingsley, and J. Papapolymerou, "Organic Wafer Scale Packaged Miniature Four-Bit RF MEMS Phase Shifter," *IEEE Transactions on Microwave Theory and Techniques,* Vol. 54, No. 3, pp. 1229-1236, March 2006.

[15] R. Bairavasubramanian, S. Pinel, J. Laskar and J. Papapolymerou, "Compact 60 GHz Bandpass Filters and Duplexers on Liquid Crystal Polymer Technology," *to be published in IEEE Microwave and Wireless Components Letters*, (acceptance letter received December 2005).

Conference publications

[1] D. Thompson, J. Papapolymerou and E. Tentzeris, "W-Band Characterization of Finite Ground Coplanar Transmission Lines on Liquid Crystal Polymer (LCP) Substrates," *2003 ECTC Conference,* pp. 1652-1655, New Orleans, LA, May 2003

[2] R. L. Li, G. DeJean, M. M. Tentzeris, J. Laskar and J. Papapolymerou, "LTCC Multilayer Based CP Patch Antenna Surrounded by a Soft-and-Hard Surface for GPS Applications," *2003 IEEE International Symposium on Antennas and Propagation Digest*, pp. 651-654, Columbus, OH, June 2003.

[3] R. Li, E. Tentzeris, J. Laskar and J. Papapolymerou, "FDTD Analysis of Microstrip Patch Antennas and Arrays on High-Dielectric Constant Substrate Surrounded by a Soft and Hard Surface," *14th Conference on the Computation of Electromagnetic Fields (Compumag 2003), Proceedings*, Vol. I, pp. 150-151, July 2003

[4] V. Palazzari, D. Thompson, N. Papageorgiou, S. Pinel, J. H. Lee, S. Sarkar, R. Pratap, G. DeJean, R. Bairavasubramanian, R.L. Li, M. Tentzeris, J. Laskar, J. Papapolymerou and L. Roselli, "Multi-band RF and mm-Wave Design Solutions for Integrated RF Functions in Liquid Crystal Polymer System-On-Package Technology," *2004 IEEE Electronic Components and Technology Conference (ECTC) Conference*, pp. 1658-1663, Las Vegas, NV, May 2004.

[5] S. Sarkar, V. Palazzari, G. Wang, N. Papageorgiou, D. Thompson, J. H. Lee, S. Pinel, M. Tentzeris, J. Papapolymerou and J. Laskar, "RF and MM-Wave SOP Module Platform Using LCP and RF MEMS Technology," *2004 IEEE International Microwave Symposium Digest* pp. 567-570, Fort Worth, TX, June 2004.

[6] G. DeJean, R.L. Li, M. Tentzeris, J. Papapolymerou and J. Laskar, "Radiation Pattern Improvement of Patch Antennas Using a Compact Soft/Hard Surface (SHS) Structure on LTCC Multilayer Technology," *2004 IEEE International Antennas and Propagation Symposium Digest*, Vol. 1, pp. 317-320, Monterey, CA, June 2004.

[7] G. Wang, D. Thompson, E.M. Tentzeris and J. Papapolymerou, "Low Cost RF MEMS Switches Using LCP Substrate," *2004 IEEE European Microwave Conference*, pp. 1441-1444, Amsterdam, The Netherlands, October 2004.

[8] S. Pinel, S. Sarkar, R. Bairavasubramanian, J.H. Lee, M. Tentzeris, J. Papapolymerou and J. Laskar, "Highly Integrated LTCC and LCP Millimeter Wave Functions for 3D-SOP High Data Rate Wireless Systems," *presented at the 2004 IEEE Asia-Pacific Microwave Conference*, New Delhi, India, December 2004.

[9] J.H. Lee, S. Sarkar, S. Pinel, J. Papapolymerou, J. Laskar and M. Tentzeris, "3D-SOP Millimeter Wave Functions for High Data Rate Wireless Systems using LTCC and LCP Technologies," *2005 IEEE Electronic Components Technology Conference*, pp. 764-768, Orlando, FL, May 2005.

[10] D. Thompson, N. Kingsley, G. Wang, M. M. Tentzeris and J. Papapolymerou, "RF Characteristics of System-Level Thin Film LCP Packages for Chip, MEMS, and MMIC Integration," *2005 IEEE International Microwave Symposium Digest*, pp. 857-860 Long Beach, CA, June 2005.

[11] R. Bairavasubramanian, S. Pinel, J.Papapolymerou, J. Laskar, C. Quendo, E. Rius, A. Manchec and C. Person, "Dual-Band Filters for WLAN Applications on Liquid Crystal Polymer Technology," *2005 IEEE International Microwave Symposium Digest*, pp. 533-536, Long Beach, CA, June 2005.

[12] C. Quendo, E. Rius, C. Person, J. Favennec, Y. Clavet, A. Manchec, R. Bairavasubramanian, S. Pinel, J. Papapolymerou and J. Laskar, "Wide Band, High Rejection and Miniaturized Fifth Order Bandpass Filter on LCP Low Cost Organic Substrate," *2005 IEEE International Microwave Symposium Digest*, pp. 2203-2205, Long Beach, CA, June 2005.

[13] D. Thompson, R.L. Li, J. Papapolymerou, J. Laskar and M. Tentzeris, "New Short Backfire Antennas for Wireless Applications," *2005 IEEE Antennas and Propagation International Symposium,* pp. 371-374, Vol. 2A, Washington, D.C., July 2005.

[14] R. Bairavasubramanian, D. Thompson, D. DeJean, G.E. Ponchak, M. Tentzeris and J. Papapolymerou, "Development of mm-wave Dual-Frequency Multilayer Antenna Arrays on Liquid Crystal Polymer (LCP) Substrate," *2005 IEEE Antennas and Propagation International Symposium*, pp. 393-396, Vol. 1B, Washington D.C., July 2005.

[15] N. Kingsley, G. Wang and J. Papapolymerou, "14 GHz Microstrip MEMS Phase Shifters on Flexible, Organic Substrate," *2005 IEEE European Microwave Conference*, pp. 625-628, Paris, France, October 2005.

[16] A. Manchec, R. Bairavasubramanian, C. Quendo, S. Pinel, E. Rius, C. Person, J.F. Favennec, J. Papapolymerou and J. Laskar, "High Rejection Planar Diplexer on Liquid Crystal Polymer Substrates Using Oversizing Techniques," *2005 IEEE European Microwave Conference*, pp. 101-104, Paris, France, October 2005.

Patents

[1] D. Thompson, N. Kingsley, G. Wang, E. Tentzeris and J. Papapolymerou, "RF MEMS Switches on Liquid Crystal Polymer (LCP) Packaged with a Thin-Film Laser Micromachined LCP superstrate," submission of the invention for patent protection to U.S. Patent and Trademark Office on 1/18/2005 (provisional patent application). A utility application (patent) has also been filed (September 2005).

[2] R. Bairavasubramanian, D. Thompson, N. Kingsley, G. Wang, G. DeJean, R.L. Li, E. Tentzeris and J. Papapolymerou, "Scannable Antenna Arrays with Microwave Components and Electronic/Electromechanical Switching Elements on Single/Multilayer Liquid Crystal Polymer Substrates," submission of the invention for patent protection to U.S. Patent and Trademark Office on 6/29/2005 (provisional patent application). A utility application (patent) has also been filed (September 2005).

Student Participation

Ph.D. Students Supported

1. Gerald DeJean
2. Ramanan Bairavasubramanian
3. Dane Thompson
4. Nickolas Kingsley